Detection of Quantum States of Light

Abstract

This thesis deals with the detection of quantum states of light. Thereby, the focus was on two main experiments.

In the first experiment, the quantum nature of light was demonstrated measuring non-classical photon statistics. For the first time this was done with a very fundamental experimental setup consisting of a quantum light source and only a single detector. Usually, for this kind of measurements a Hanbury-Brown-Twiss setup is employed which consists of a beam splitter with two detectors placed in its outputs. As a non-classical light source a nitrogen-vacancy centre in a nano-diamond was used. The simplification of the experimental setup was possible, because the measurements were done with a detector with a dead time much shorter than the source's intensity auto-correlation time. For detection, a super-conducting single-photon detector with an active area of $10\,\mu\mathrm{m}\times10\,\mu\mathrm{m}$ formed by a meandering nanowire was utilised. In this thesis, a procedure was developed to couple these structures effectively to a single-mode optical fibre.

The other main experiment dealt with the implementation of different strategies for optimal discrimination of quantum states. In quantum mechanics, e.g. two non-orthogonal states cannot be discriminated without errors by one projective measurement. However, under certain conditions there are ways to discriminate such states unambiguously at the expense of allowing for inconclusive results. In this work experimental unambiguous discrimination of two mixed single-photon states was carried out for the first time. Furthermore, in a different scenario, where unambiguous discrimination is not possible, optimum maximum-confidence discrimination of two single-photon states could be implemented. The states to be discriminated were prepared with single-photons from an electrically pumped quantum-dot source.

The experimental results obtained in this work affirm fundamental properties of quantum mechanics, and they can be used to improve the experimental setups for detecting light states in various cases.

Zusammenfassung

Die vorliegende Arbeit widmet sich der Untersuchung verschiedener Aspekte der Detektion von Quantenzuständen des Lichts. Zwei Experimente standen dabei im Vordergrund.

Im ersten Experiment wurde die Quantennatur des Lichts erstmalig mit einem sehr fundamentalen experimentellen Aufbau, bestehend nur aus einer nichtklassischen Lichtquelle und einem Detektor, nachgewiesen. Dies geschah über eine Messung der Photonenstatistik der Quelle. Normalerweise wird dafür ein Hanbury-Brown-Twiss-Aufbau verwendet, welcher aus einem Strahlteiler und zwei in dessen Ausgängen platzierten Detektoren besteht. Die Messung mit nur einem Detektor war hier möglich, weil Detektoren verwendet wurden, deren Totzeit viel kürzer ist als die Intensitätsautokorrelationszeit der verwendeten Einzelphotonenquelle, hier ein Stickstoff-Fehlstellen-Defekt in einem Nanodiamanten. Für die Detektion wurden supraleitende Einzelphotonendetektoren benutzt, deren $10\,\mu\text{m} \times 10\,\mu\text{m}$ große aktive Fläche aus einem mäanderförmig angeordneten Nanodraht besteht. Im Rahmen dieser Arbeit wurde eine Methode entwickelt, eine optische Faser effektiv an diese Mäanderstrukturen anzukoppeln.

Im zweiten Hauptexperiment wurden verschiedene Strategien zur optimalen Unterscheidung von Quantenzuständen implementiert. Aufgrund grundlegender quantenmechanischer Gesetze können z.B. zwei nicht-senkrechte Zustände durch eine projektive Messung nicht fehlerfrei unterschieden werden. Allerdings kann man dies in manchen Fällen erreichen, wenn man außerdem Messergebnisse zulässt, die keine Aussage über den Anfangszustand machen. Eine solche Art der Zustandsunterscheidung wurde hier erstmals experimentell mit gemischten Einzelphotonenzuständen implementiert. Außerdem wurden in einem ählichen Experiment, wo eindeutige, d.h. fehlerfreie Zustandsunterscheidung nicht möglich war, zwei gemischte Einzelphotonenzustände optimal mit minimalem Fehler unterschieden. Als Einzelphotonenquelle diente in beiden Fällen ein elektrisch gepumpter Quantenpunkt.

Die experimentellen Ergebnisse bestätigen zum einen fundamentale quantenmechanische Zusammenhänge, zum anderen können sie dazu dienen, die Messaufbauten für verschiedene (quanten-)optische Experimente effektiver zu machen.

Contents

Contents

1 Introduction

In order to study fundamental quantum mechanical properties experimentally, experiments performed on isolated quantum objects (figure 1.1) have turned out to be very useful. However, it is not trivial to achieve complete control of such a system, as e.g. single atoms or molecules are difficult to isolate due to their strong interaction with the environment. For light this interaction is much weaker, which means that in experiments with isolated single photons uncontrolled environmental disturbances can be avoided more easily. On the other hand, there are a lot of feasible tools for controlled manipulation. Therefore, in many cases the quanta of light are a good system to study fundamental quantum effects.

Though most of the activities in the field of quantum optics are still basic research, some prove-of-principle experiments have already been followed by first applications. One prominent example for that is quantum cryptography [1] (figure 1.2a). Here, the basic properties of quantum mechanics are exploited to guarantee the security of a secret key distributed between two parties. Based on ideas by S. Wiesner, Bennett and Brassard published a proposal for a first quantum key distribution (QKD) protocol in 1984 [2]. Since then a rapid development took place, and nowadays quantum cryptography systems have become commercially available. Today, another commercial quantum-optical product, even though not as sophisticated as the QKD systems, are quantum random number generators, which exploit the probabilistic nature of quantum mechanical measurements to obtain random numbers from an intrinsically random process (figure 1.2b).

One imaginable future application of contemporary quantum optical research is quantum information processing (figure 1.2c). In a classical computer, information is coded in bits having a value of 0 or 1. To execute calculations, operations on the bits have to be performed using a certain set of gates. Instead of classical bits, so-called quantum bits or *qubits* can be used which are quantum mechanical superpositions of the states $|0\rangle$ and $|1\rangle$. Utilising qubits and an appropriate set of quantum gates to perform the necessary operations on the qubits, a quantum computer is able to execute certain task more efficient than a classical one. In particular, there are three important classes of problems, where quantum computers are known to provide more efficient algorithms than classical ones. A quantum computer was firstly proposed by R. P. Feynman in 1982, who suggested to execute quantum simulations on a quantum system [3]. In 1994 an efficient way for prime factorisation on a quantum computer was found by P. W. Shor [4], and three years later L. K. Grover proposed a quantum algorithm for the search of elements in an unsorted set [5]. A scheme for implementing a quantum computer using photonic qubits and linear optics was developed in 2001 by
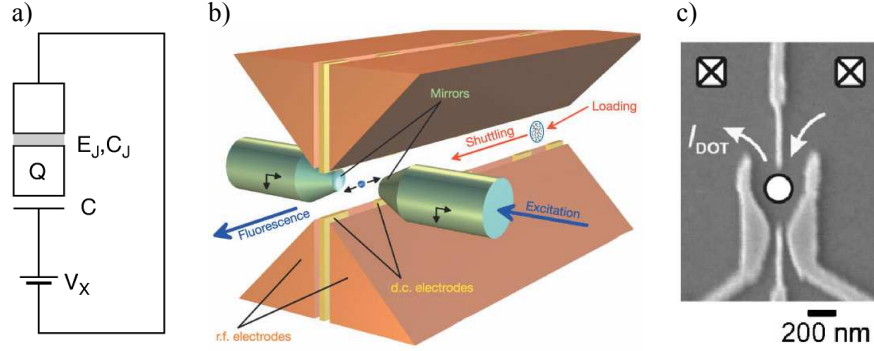
Figure 1.1: Examples of isolated quantum systems. (a) A single quantum objects provided by a superconducting electron box with Cooper-pair charge $Q = 2ne$. The superconducting island is coupled by a Josephson tunnel barrier (grey area) to a lead (from [7]). (b) A single ion isolated in an ion trap (from [8]). (c) Scanning electron microscope picture of a quantum-dot device defined by metal surface electrodes (from [9]).

Knill et al. [6].

No matter what kind of experiment one wishes to implement with light quanta, there is always the need to produce and detect single photons. Both of these steps are challenging tasks. The production of single photons is different from attenuating a bright classical source, since due to the processes involved in its preparation, the latter would always deliver a light state that shows classical behaviour. Systems able to emit quantum states of light are often isolated single systems possessing a discrete energy level structure.

In this thesis, research is reported concerning the detection of single photons. One necessary condition for that is to have detectors sensitive for very small light intensities, since the energies single photons posses are on the order of 1 eV. There are many types of such detectors, the ones mostly used nowadays are based on semiconducting or superconducting materials. One very recent type of superconducting detectors is investigated in detail in this work.

The quantisation of light can be demonstrated by looking for correlations in the photon stream from non-classical emitters. Light emitted by such sources shows other intensity auto-correlations than e.g. a laser light source: in a light stream of single photons emitted "one by one" there won't be two photons impinging on a detector at the same time, whereas in a laser beam, where photons are emitted independently of each other, this happens with a certain probability. Thus, the ability to determine photon statistics is essential to prove non-classical behaviour. In this thesis an experiment is discussed where this was done in a very fundamental way.

A click in the single-photon detector indicates that there was a photon at a certain position $\vec{r}$ and time t. Quantum mechanically, an object, as e.g. the photon before the measurement, is completely described by its wave function $\psi(\vec{r}, t)$ [10]. According
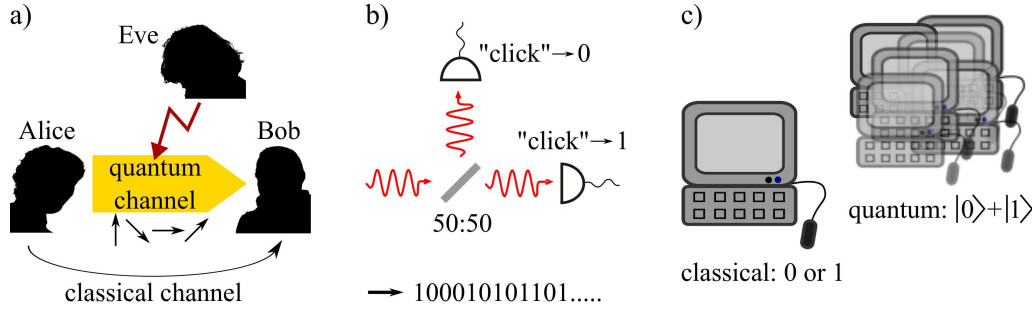
Figure 1.2: Possible applications of single photons. (a) Quantum cryptography. (b) Quantum random-number generation. (c) Quantum information processing.

to the *Copenhagen interpretation* of quantum mechanics [11], ψ is usually interpreted as a probability amplitude. That means, $|\psi|^2$ gives the probability to find the photon at position $\vec{r}$ and time t. Thus, a click in the detector gives only limited information about the photon before detection. Generally, the state (the wave function) of any quantum object is altered by measurements [12], which means that usually only one measurement can be performed on the unaltered input state. This leads to some fundamental difficulties for a complete analysis of an unknown initial state. Depending on the prior knowledge about possible states, there are different strategies how to obtain a maximum of information about the initial state performing one measurement. This kind of problems are addressed in the last part of this work where corresponding experiments are shown.

The thesis is organised as follows:

- In Chapter 2 the photons are formally introduced and some fundamental consequences of the non-classical description of light are discussed.

- In Chapter 3 single-photon sources are discussed, in particular those employed in the experiments that were carried out here, namely semiconductor quantum dots and the nitrogen-vacancy defect centre in diamond.

- In Chapter 4 an overview of single-photon detectors is given and a special type, the nanowire superconducting single-photon detectors (NSSPDs) are introduced and characterised.

- In Chapter 5 an experiment is presented that proves the quantum nature of light in a very fundamental way utilising a NSSPD.

- In Chapter 6 the experimental implementation of strategies for discriminating non-orthogonal quantum states is shown.

- Chapter 7 contains a summary and an outlook addressing possible future developments.

2 Quantum States of Light

Although light is a part of everybody's every-day experience, it is not trivial to find a model (i.e. a mathematical expression) to describe all aspects of this phenomenon. Around the year 1900 evidence was found that the description of light as an electromagnetic wave, which was employed at that time and is still a very powerful tool for describing many of its aspects, fails in explaining some experimental results. A solution for understanding these results was developed as quantum mechanics evolved, and consists in the description of light as a quantum object as well.

In the first part of this chapter, the quantum of light, the photon, is introduced and some special quantum states of light are defined. In the second section, statistical properties of light states are discussed. The chapter closes with some remarks concerning the measurement process in terms of quantum mechanics.

2.1 The Photon

A quantum theory of light implies that there are light quanta as impartible entities. This quantum is called *photon* in analogy to electrons as impartible entities of the electric current.

However, there are many properties of light that can be well explained without assuming the existence of photons. Interference and diffraction effects can be understood employing the model of light as an electromagnetic wave, based on Maxwell's equations and the Huygens principle. At the beginning of the 20th century this wave model gave a satisfactory description of almost all known phenomena, but it failed to explain an experimental result obtained some years before. However, this effect could very well be modelled assuming an energy quantisation for light.

2.1.1 The Photoelectric Effect

In 1887, H. Hertz discovered that when a metal surface is irradiated with UV light, electrons are emitted (see figure 2.1). This phenomenon is called photoelectric effect. The experimental results are the following:

1. There is a threshold frequency ν_0 for the photoelectric effect. For frequencies $\nu < \nu_0$ no electrons are emitted from the surface.

2. For frequencies above ν_0, the amount of electrons emitted is proportional to the light intensity.
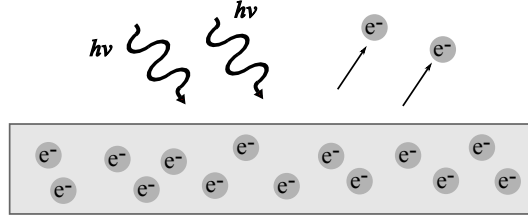
Figure 2.1: Photoelectric effect.

3. The kinetic energy of the electrons depends linearly on the light frequency.

4. No temporal delay is measured between switching on the light and emission of electrons.

An interpretation applying a wave theory of light faces some difficulties. Classically, for the kinetic energy of the electrons one would expect a dependence of the light intensity. The electron would be expected to be emitted as soon it has absorbed enough energy from the light field. This would in some cases also mean that a substantial temporal delay between the begin of absorption of light and the emission of electrons could be measured.

A coherent interpretation of the photoelectric effect was given by A. Einstein in 1905 [13]. He assumed that the energy of the light field is not distributed continuously but as a sum of impartible energy quanta. For light of frequency ν they have the energy

$$E = h\nu \tag{2.1}$$

where h is the constant M. Planck introduced in 1900 as an auxiliary quantity to derive a law for the spectral energy density of a black body [14]. For every electron emitted from the metal a photon has been absorbed. Hence, the electron's energy is increased by

$$\frac{1}{2}m_e v^2 = h\nu - W \tag{2.2}$$

with v being the velocity of the emitted electron and W the work required to overcome its binding energy. Thus the photon's kinetic energy is linearly dependent on the frequency and there is a threshold frequency $\nu_0 = W/h$. The number of electrons emitted depends on the intensity of the light (the amount of incident photons) and the emission of an electron takes place immediately upon photon absorption.

This interpretation of the photoelectric effect was the birth of a quantum theory of light and was awarded the Nobel Prize in 1921. In the next section a formal introduction of the quantisation of the electromagnetic field is sketched.

2.1.2 Quantisation of the Electromagnetic Field

The classical electromagnetic field in free space is described by the Maxwell's equations

$$\nabla \cdot \vec{E} = 0 \tag{2.3}$$

$$\nabla \cdot \vec{H} = 0 \tag{2.4}$$

$$\nabla \times \vec{E} = -\mu_0 \frac{\partial \vec{H}}{\partial t} \tag{2.5}$$

$$\nabla \times \vec{H} = \varepsilon_0 \frac{\partial \vec{E}}{\partial t} \tag{2.6}$$

where $\vec{E}$, $\vec{H}$ are the electric and magnetic field and ε_0, μ_0 the free space permittivity and permeability, respectively. Taking the curl of equation 2.5 and substituting the vacuum speed of light $c = 1/\sqrt{\varepsilon_0 \mu_0}$, the wave equation for the electric field follows

$$\nabla^2 \vec{E} - \frac{1}{c^2} \frac{\partial^2 \vec{E}}{\partial t^2} = 0. \tag{2.7}$$

Assuming periodic boundary conditions, i.e. a box of length L and volume V, and an electric field linearly polarised in x-direction (see figure 2.2) the electric field can be expanded in the eigenmodes of the box

$$E_x(z,t) = \sum_{j=1}^{\infty} A_j q_j(t) \sin(k_j z) \tag{2.8}$$

with $k_j = j\pi/L$, q_j being the amplitude of the mode (with dimension of a length), and

$$A_j = \left(\frac{2\omega_j^2 m_j}{\varepsilon_0 V} \right)^{\frac{1}{2}} \tag{2.9}$$
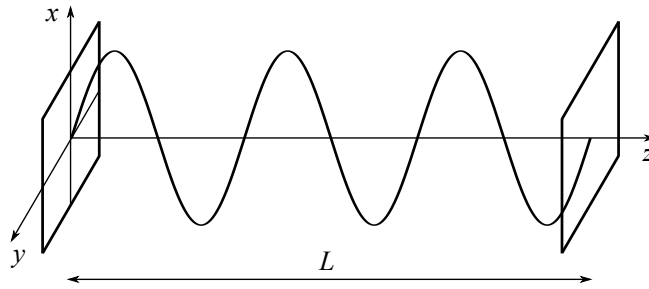
Figure 2.2: Electric field of an eigenmode of a box of length L. The field is assumed to be linearly polarised in x-direction.

where $\omega_j = c \cdot k_j$ and m_j is a constant with dimension of a mass. Here q_j and m_j have been introduced to establish the analogy to a mechanical oscillator with mass m_j and Cartesian coordinate q_j. For the magnetic field follows

$$H_y(z,t) = \sum_{j=1}^{\infty} A_j \frac{\dot{q}_j \varepsilon_0}{k_j} \cos{(k_j z)}. \tag{2.10}$$

The classical Hamiltonian for the field is given by

$$\mathcal{H} = \frac{1}{2} \int_V \left(\varepsilon_0 E_x^2 + \mu_0 H_y^2 \right) \mathrm{d}V \tag{2.11}$$

Substitution of E_x and H_y results in

$$\mathcal{H} = \frac{1}{2} \sum_j \left(m_j \omega_j^2 q_j^2 + m_j \dot{q}_j^2 \right) = \frac{1}{2} \sum_j \left(m_j \omega_j^2 q_j^2 + \frac{p_j^2}{m_j} \right) \tag{2.12}$$

where $p_j = m_j \dot{q}_j$ is the canonical momentum of the jth mode. This equation is equivalent to the Hamiltonian of a sum of harmonic oscillators, one for each mode. The light field can thus be quantised as the mechanical harmonic oscillator by associating q_j, p_j with operators obeying the commutation relation

$$[q_j, p_{j'}]_- = \mathrm{i}\hbar \delta_{jj'} \tag{2.13}$$

$$[q_j, q_{j'}]_- = [p_j, p_{j'}]_- = 0 \tag{2.14}$$

It is convenient to replace the q_j, p_j by new operators a_j, $a_j^\dagger$ via a canonical transformation

$$a_j \mathrm{e}^{-\mathrm{i}\omega_j t} = \frac{1}{\sqrt{2m_j \hbar \omega_j}} (m_j \omega_j q_j + \mathrm{i}p_j) \tag{2.15}$$

$$a_j^\dagger \mathrm{e}^{\mathrm{i}\omega_j t} = \frac{1}{\sqrt{2m_j \hbar \omega_j}} (m_j \omega_j q_j - \mathrm{i}p_j) \tag{2.16}$$

Then it follows for the commutation relations of the a_j, $a_j^\dagger$

$$\left[a_j, a_{j'}^\dagger \right]_- = \delta_{jj'} \tag{2.17}$$

$$[a_j, a_{j'}]_- = \left[a_j^\dagger, a_{j'}^\dagger \right]_- = 0 \tag{2.18}$$

and for the Hamiltonian of the quantised free electromagnetic field

$$\mathcal{H} = \frac{1}{2} \sum_j \left(m_j \omega_j^2 q_j^2 + \frac{p_j^2}{m_j} \right) = \sum_j \hbar \omega_j \left(a_j^\dagger a_j + \frac{1}{2} \right). \tag{2.19}$$

In terms of a_k and $a_k^\dagger$, electric and magnetic field take the form [15]

$$\vec{E}(\vec{r}, t) = \sum_{\vec{k}} \vec{e}_{\vec{k}} \mathcal{E}_{\vec{k}} a_{\vec{k}} \, \mathrm{e}^{-\mathrm{i}(\omega_k t - \vec{k} \cdot \vec{r})} + \mathrm{H.c.} \tag{2.20}$$

$$\vec{H}(\vec{r}, t) = \frac{1}{\mu_0} \sum_{\vec{k}} \frac{\vec{k} \times \vec{e}_{\vec{k}}}{\omega_k} \mathcal{E}_{\vec{k}} a_{\vec{k}} \, \mathrm{e}^{-\mathrm{i}(\omega_k t - \vec{k} \cdot \vec{r})} + \mathrm{H.c.} \tag{2.21}$$

where $\vec{e}_{\vec{k}}$ is the polarisation vector and $\mathcal{E}_{\vec{k}} = \sqrt{\hbar \omega_k / \varepsilon_0 V}$ the electric field per photon.

2.1.3 Number States and Coherent States

The quantised Hamiltonian possesses eigenstates exhibiting highly non-classical properties, which are introduced in this section. Another class of light states worth mentioning in particular, the so called coherent states, will be discussed afterwards.

Number States or Fock States

Number states or Fock states $|n\rangle$ are eigenstates of the Hamiltonian of the quantised free field (equation 2.19), or introducing the number operator $\hat{n} = a^\dagger a$, eigenstates of the number operator, i.e.

$$\hat{n}|n\rangle = n|n\rangle. \tag{2.22}$$

A number state $|n\rangle$ is a state with exactly n photons in the same mode. The energy of this state is then

$$\langle n|\mathcal{H}|n\rangle = \hbar \omega n + H_0. \tag{2.23}$$

Fock states are orthogonal, i.e. $\langle n|m\rangle = \delta_{nm}$, and complete, i.e. $\sum_{n=0}^{\infty} |n\rangle\langle n| = 1$ [16], which means that every state $|\psi\rangle$ can be expanded in the Fock basis as

$$|\psi\rangle = \sum_{n=0}^{\infty} |n\rangle\langle n|\psi\rangle. \tag{2.24}$$

Thus the photon number distribution $p_{|\psi\rangle}(n)$ of state $|\psi\rangle$, i.e. the probability to find n photons in the same mode is given by

$$p_{|\psi\rangle}(n) = |\langle n|\psi\rangle|^2. \tag{2.25}$$

For the operators a, $a^\dagger$ it can be shown that the following equations hold

$$a|n\rangle = \sqrt{n}|n-1\rangle \tag{2.26}$$
$$a^\dagger|n\rangle = \sqrt{n+1}|n+1\rangle. \tag{2.27}$$

Therefore a and $a^\dagger$ are usually called annihilation and creation operator.

Two special states of number states are the vacuum state $|0\rangle$ and the single-photon
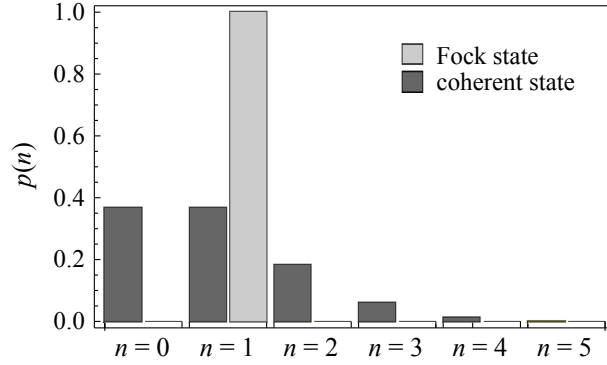
Figure 2.3: Photon number distribution $p(n)$ for a Fock state $|n = 1\rangle$ and a coherent state with mean photon number $\bar{n} = 1$.

state $|1\rangle$. Every number states $|n\rangle$ can be expressed applying the creation operator n times on the vacuum state

$$|n\rangle = \frac{(a^\dagger)^n}{\sqrt{n!}}|0\rangle. \tag{2.28}$$

Single-photon states $|1\rangle$ are interesting objects to study the quantum nature of light since experimentally they are relatively easy to prepare, at least compared to number states $|n\rangle$ with $n > 1$. A criterion to prove single-photon emission from a quantum light source experimentally will be given in section 2.2.2.

Coherent States

Formally, coherent states $|\alpha\rangle$ can be defined as eigenstates of the annihilation operator

$$a|\alpha\rangle = \alpha|\alpha\rangle. \tag{2.29}$$

The interesting feature of these states is that the mean values of observables such as Hamiltonian, electric field, polarisation field etc. are equal to the corresponding classical values [16]. Furthermore it can be shown that $|\alpha\rangle$ is a minimum uncertainty state, i.e. $\Delta p \cdot \Delta q = \hbar/2$ for coherent states [16].

Using equations 2.28 and 2.29, an expansion in the Fock basis yields

$$|\alpha\rangle = \sum_{n=0}^{\infty} |n\rangle\langle n|\alpha\rangle = e^{-|\alpha|^2/2} \sum_{n=0}^{\infty} \frac{\alpha^n}{\sqrt{n!}}|n\rangle. \tag{2.30}$$

Thus the photon number distribution $p(n)$ of a coherent state is

$$p(n) = \langle n|\alpha\rangle\langle \alpha|n\rangle = \frac{\bar{n}^n e^{-\bar{n}}}{n!} \tag{2.31}$$

which is a Poissonian distribution with $\bar{n} = \langle\alpha|a^\dagger a|\alpha\rangle = |\alpha|^2$ being the mean number of photons in the coherent state. Figure 2.3 depicts the photon number distribution of a coherent state with $\bar{n} = 1$ compared to a $|n = 1\rangle$ number state.

The term *coherent state* is motivated by the specific auto-correlation properties of these states. The corresponding correlation functions of the electric field will be discussed in the next section.

2.2 Photon Statistics

A characteristic feature of light sources are their statistical properties of photon emission. There are sources that emit photons uncorrelated, i.e. the probability of emission of one photon is not altered by emission of another one, and those which exhibit strong correlations in their emission properties.

As pointed out in the previous section, the photon number is an operator associated with the second order of the electric field, the intensity. That means an investigation of the photon statistics of a light source is an investigation of its intensity auto-correlations. Before discussing intensity auto-correlations in more detail, correlation functions of the electric field will be introduced in general in this section.

2.2.1 Correlation Functions of the Electric Field

Correlation functions of the electric field are very useful not only to characterise statistical properties of a light source, but also to describe interference phenomena and to define optical coherence.

A correlation function C of two variables v and w in two points $z_1 = (\vec{r}_1, t_1)$ and $z_2 = (\vec{r}_2, t_2)$ is given by

$$C_{vw}(z_1, z_2) = \langle v(z_1)w(z_2)\rangle. \tag{2.32}$$

If correlations of the same quantity ($v = w$) at two different points in space or time are considered, this is often referred to as auto-correlations. In optics the interesting quantity is usually the electric field, therefore in the following only auto-correlation functions of electric fields will be discussed. Following the approach by Glauber [17], we define the nth order (auto-)correlation function $G^{(n)}$ of an electric field $E(z)$, $z = (\vec{r}, t)$ in the state characterised by the density operator ρ by

$$G^{(n)}(z_1, \ldots, z_n, z_{n+1}, \ldots, z_{2n}) = \text{Tr}\left(\rho E^\dagger(z_1)\ldots E^\dagger(z_n)E(z_{n+1})\ldots E(z_{2n})\right). \tag{2.33}$$

Here, $\rho = \sum_j \eta_j|\psi_j\rangle\langle\psi_j|$ is the density operator characterising a statistical mixture of states $|\psi_j\rangle$ with respective probabilities η_j (cf. section 2.3.2).

The first-order correlation function $G^{(1)}$ displays field amplitude correlations. Therefore they are useful to describe interference phenomena. To define temporal and spatial coherence, the first-order auto-correlations at the same point at two different times, $E(x, t)$, $E(x, t + \tau)$, or at the same time at two different points, $E(x, t)$, $E(x + \xi, t)$,

respectively, are of interest. Normalised first-order correlation functions are given by

$$g^{(1)}(\tau) = \frac{\langle E^\dagger(t)E(t+\tau)\rangle_t}{\sqrt{\langle|E(t)|^2\rangle_t\langle|E(t+\tau)|^2\rangle_t}} \qquad (2.34)$$

$$g^{(1)}(\xi) = \frac{\langle E^\dagger(x)E(x+\xi)\rangle_x}{\sqrt{\langle|E(x)|^2\rangle_x\langle|E(x+\xi)|^2\rangle_x}} \qquad (2.35)$$

where $|E| = \sqrt{E^\dagger E}$. First-order coherence can then be defined as

$$|g^{(1)}| = \begin{cases} 1 & \text{coherent} \\ 0 & \text{incoherent} \\ 0 < \cdots < 1 & \text{partially coherent.} \end{cases} \qquad (2.36)$$

For all fields $g^{(1)}(0) = 1$. For very large time differences τ, $g^{(1)}(\tau)$ approaches zero. The time scale τ_c for this to happen is called coherence time. For fields with constant amplitude $g^{(1)}(\tau) = 1$ for all τ, that means the coherence time is infinitely long. A spatial coherence length can be defined analogously.

Temporal first-order correlation function $G^{(1)}(\tau) = \langle E^\dagger(t)E(t+\tau)\rangle_t$ and spectral density $S(\omega)$ of a light source are related by the Wiener-Khinchin theorem

$$S(\omega) = \int\limits_{-\infty}^{\infty} \mathrm{e}^{-\mathrm{i}\omega\tau}G^{(1)}(\tau)\mathrm{d}\tau. \qquad (2.37)$$

Experimentally, this means that coherence properties can be investigated measuring spectral properties and vice versa, e.g. small linewidths can be determined interferometricly.

2.2.2 Temporal Second-order Correlations

Similar to equation 2.34, the normalised temporal second-order correlation function is given by

$$g^{(2)}(\tau) = \frac{\langle E^\dagger(t)E^\dagger(t+\tau)E(t+\tau)E(t)\rangle_t}{\langle|E(t)|^2\rangle_t\langle|E(t+\tau)|^2\rangle_t}. \qquad (2.38)$$

Second-order correlation functions of the electric field describe intensity correlations. $g^{(2)}(\tau)$ gives the joint probability of detecting the arrival of a photon at time $t+\tau$ given the detection of another photon at time t.

$g^{(2)}$-**functions for Classical Fields**

The evaluation of the second-order correlation function for classical fields can be found in many textbooks, e.g. [16, 18]. Assuming a probability distribution $P(\varepsilon)$ for the

fluctuating classical field

$$E(\varepsilon, t) = -\left(\mathrm{i}\frac{\hbar\omega}{2\varepsilon_0 V}\right)^{1/2} \varepsilon \mathrm{e}^{-\mathrm{i}\omega t} \tag{2.39}$$

to have the amplitude ε, one can write for zero time delay

$$g^{(2)}(0) = 1 + \frac{\int P(\varepsilon)(|\varepsilon|^2 - \langle|\varepsilon|^2\rangle)^2 \mathrm{d}^2\varepsilon}{\langle|\varepsilon|^2\rangle^2}. \tag{2.40}$$

Since the probability distribution $P(\varepsilon)$ is positive, for classical fields follows

$$g^{(2)}(0) \geq 1. \tag{2.41}$$

Further evaluation for a field obeying Gaussian statistics with zero mean amplitude yields [16]

$$g^{(2)}(\tau) = 1 + |g^{(1)}(\tau)|^2. \tag{2.42}$$

Applying the Wiener-Khinchin theorem (equation 2.37), for a thermal field with spectral linewidth γ the normalized second-order correlation function is given by

$$g^{(2)}(\tau) = \begin{cases} 1 + \mathrm{e}^{-\gamma\tau} & \text{for a Lorentian spectrum and} \\ 1 + \mathrm{e}^{-\gamma^2\tau^2} & \text{for a Gaussian spectrum.} \end{cases} \tag{2.43}$$

The probability of detecting a second photon right after the detection of a first one is increased for fluctuating classical sources. The phenomenon is called *bunching*. For chaotic sources it can be understood since the $g^{(2)}$-function depends quadratically on the field intensity. For a fluctuating field, intensities above the mean account more for the intensity correlation function than the fluctuations below the mean.

Experimentally, it can be challenging to resolve the bunching peak of a classical light source because the spectral linewidth of the source needs to be narrow enough (cf. equation 2.37). For a linewidth of 100 MHz to 1 GHz, peak widths are on the order of some 100 ps and can thus be resolved [19]. Bunching peaks can not be resolved experimentally for spectrally much broader sources.

$g^{(2)}$-function for Coherent States

Since coherent states $|\alpha\rangle$ are eigenstates of the annihilation operator a, the $g^{(2)}$-function equals

$$g^{(2)}(\tau) = 1 \tag{2.44}$$

for all time differences τ. That means, that a coherent source is a light source with no intensity fluctuations. Photons are emitted independently of each other. This property is equivalent to the fact, that coherent states possess a Poissonian photon number distribution (cf. equation 2.31). Sometimes sources with $g^{(2)} > 1$ are therefore called *super-Poissonian* and sources with $g^{(2)} < 1$ *sub-Poissonian*.

$g^{(2)}$-function for Quantum Fields

Applying the quantisation of the field given in section 2.1.2, for a single-mode quantum field the normalized second-order correlation function can be written using creation and annihilation operators. For zero time difference this results in

$$g^{(2)}(0) = \frac{\langle a^\dagger a^\dagger a a \rangle}{\langle a^\dagger a \rangle^2}. \tag{2.45}$$

Using the number operator $\hat{n} = a^\dagger a$ with $\hat{n}|n\rangle = n|n\rangle$ and the commutator relation $[a, a^\dagger] = 1$, for a number state $|n\rangle$ $g^{(2)}(0)$ can be calculated as

$$g^{(2)}(0) = \frac{\langle n|a^\dagger(aa^\dagger - 1)a|n\rangle}{\langle n|\hat{n}|n\rangle^2} = \frac{n^2 - n}{n^2} = 1 - \frac{1}{n}. \tag{2.46}$$

Thus Fock states show an intensity correlation called *antibunching*: the probability to detect a second photon directly after a first one is suppressed, which is a clearly non-classical behaviour (cf. equation 2.41). Equation 2.46 provides a criterion for single-photon emission. Under realistic conditions in an experiment, usually $g^{(2)}(0) < 0.5$ is accepted as a prove of single-photon emission. Experimentally, often a two-level system is employed to obtain single-photon states. When the excited state decays, a single photon is emitted. In this case the width of the antibunching feature depends on the lifetime of the excited state and on the pump rate [20]. Single-photon sources will be discussed in more detail in chapter 3.

In figure 2.4 normalized second-order correlation functions for three different sources, a classical (Gaussian) source, a coherent source, and a quantum (Fock state $|n = 1\rangle$) source are shown.
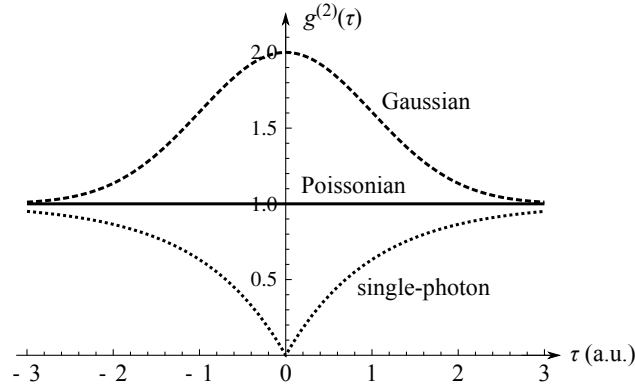
Figure 2.4: Theoretical second-order correlation functions of a Gaussian field, a coherent state, and a single-photon (Fock state $|n = 1\rangle$) state.

2.3 Measurements on Quantum States of Light

In the last section of this chapter, it is discussed what it means in quantum mechanics to perform a measurement. Experimental investigations on quantum states of light always have to use a light detector which renders a classical quantity. The task for the experimentalist in quantum physics is to construct devices that allow him/her to obtain information about the quantum states existing before the measurement from the classical values obtained during the measurement process.

Before discussing some aspects of the measurement of quantum states of light, it might be useful to recall the postulates of quantum mechanics [21]:

Postulate 1 (State Space) *Any physical system can be associated with a Hilbert space, i.e. a complex vector space with an inner product, which is called the state space of the system. The system is completely described by its state vector $|\psi\rangle$, which is a unit vector in the state space.*

Postulate 2 (Evolution) *The evolution of a closed quantum system is described by a unitary transformation U, i.e. the state $|\psi'\rangle$ at time t_2 is related to the state $|\psi\rangle$ at time t_1 by a unitary operator $U(t_1, t_2)$ depending only on t_1, t_2:*

$$|\psi'\rangle = U(t_1, t_2)|\psi\rangle. \tag{2.47}$$

Postulate 3 (Measurement) *A quantum measurement is defined by a set of measurement operators $\{M_j\}$ associated with the possible measurement outcomes $\{j\}$ acting on the state space of the system being measured. The set of measurement operators $\{M_j\}$ is complete, i.e. $\sum_j M_j^\dagger M_j = I$. The probability $p_{|\psi\rangle}(j)$ to measure outcome j when the system is in the state $|\psi\rangle$ is given by*

$$p_{|\psi\rangle}(j) = \langle\psi|M_j^\dagger M_j|\psi\rangle \tag{2.48}$$

and after the measurement the system is in the state

$$|\psi'\rangle = \frac{M_j|\psi\rangle}{\sqrt{\langle\psi|M_j^\dagger M_j|\psi\rangle}}. \tag{2.49}$$

Equation 2.49 states that after the measurement on $|\psi\rangle$ the system may be in a different state $|\psi'\rangle$. This is often referred to as the *collapse* of the wave function.

2.3.1 Measurements in Quantum Mechanics

The postulate on the quantum measurement (postulate 3) introduces a concept of the measurement process that is very different from the classical one. In most cases the outcomes of a measurement can be predicted only statistically and every measurement alters the system being measured.

Projective Measurements

A projective measurement, also called *von Neumann* measurement, is a special case of the measurement introduced in postulate 3. Often, one is primarily concerned with projective measurements. For further discussion see e.g. [21].

A projective measurement is associated with an *observable*, a Hermitian operator A. With $\{a\}$, $\{|a\rangle\}$ being the eigenvalues and corresponding eigenstates of A and using the projectors $P_a = |a\rangle\langle a|$, A can be written as a spectral decomposition

$$A = \sum_a a P_a. \tag{2.50}$$

The possible outcomes of the measurement are the eigenvalues $\{a\}$ of operator A. The probability $p_{|\psi\rangle}(a)$ to measure a is given by

$$p_{|\psi\rangle}(a) = \langle\psi|P_a|\psi\rangle = |\langle a|\psi\rangle|^2. \tag{2.51}$$

Equation 2.49 states that a measurement of the observable A on state $|\psi\rangle$ projects $|\psi\rangle$ on a state

$$|\psi'\rangle = \frac{P_a|\psi\rangle}{|\langle a|\psi\rangle|}, \tag{2.52}$$

i.e. the measurement of the observable A projects the initial state $|\psi\rangle$ on a normalised state $|\psi'\rangle$ parallel to one of the eigenstates $|a\rangle$ of A.

The Heisenberg Uncertainty Principle

Measurements of different observables A, B can depend on the order in which measurements are performed. If A and B do not have the same set of eigenstates, a measurement of A, i.e. a projection on one of A's eigenstates $|a\rangle$ followed by a measurement of B, i.e. a projection on one of B's eigenstates $|b\rangle$, can have a different result than a measurement of both observables with reversed order. The condition that A and B have the same eigenstates is equivalent to $[A, B]_- = 0$.

Measuring the observable A, the deviation ΔA_ψ of the measurement outcomes from the mean is given by

$$\Delta A_\psi^2 = \langle\psi|\left(A - \langle\psi|A|\psi\rangle\right)^2|\psi\rangle. \tag{2.53}$$

It is zero, if and only if $|\psi\rangle$ is an eigenstate of A. It can be shown that for two observables A, B the following inequality, the Heisenberg uncertainty principle, holds [22]

$$\Delta A_\psi \Delta B_\psi \geq \frac{1}{2}|\langle\psi|[A, B]_-|\psi\rangle|. \tag{2.54}$$

That means, two non-commuting observables cannot be measured with arbitrary precision at the same time. Pairs of non-commuting observables are e.g. position and momentum.

Generalised Measurements

Postulate 3 includes a very general description of the measurement process. Often the measurement is introduced as what was above called the special case of a projective measurement. For establishing a coherent quantum mechanical description this turns out not to be much of a difference, since the more general expression is equivalent to the one containing only projective measurements as long as they are extended by the ability to perform unitary transformations (postulate 2) [21].

A very useful tool for the description of generalised measurements is the *positive operator-valued measure* (POVM) formalism [23, 24]. When a measurement is performed on state $|\psi\rangle$ associated with the measurement operators $\{M_j\}$, a set $\{E_j\}$ of positive operators can be defined as

$$E_j := M_j^\dagger M_j. \tag{2.55}$$

Then the E_j are complete, i.e. $\sum_j E_j = I$, and the probability to measure j equals $p_{|\psi\rangle}(j) = \langle\psi|E_j|\psi\rangle$. The E_j are called the POVM elements associated with the measurement, the complete set $\{E_j\}$ is the POVM. It is straightforward to verify that for the projective measurement the measurement operators are the same as the POVM elements, $P_j = E_j$. (It can also be shown, that this is *only* the case for projective measurements [21].)

At first, the need for introducing this general formalism for describing measurements might not be apparent. Nevertheless, there are many cases where it is the preferred choice to express the measurement processes. For example in quantum information, the POVM model is applied very successfully when the task is to find the optimal way to distinguish quantum states from a known set. This problem is discussed in particular in chapter 6.

2.3.2 Analysis of Quantum States

A quantum object is described by its state vector $|\psi\rangle$. However, sometimes systems are prepared not in a pure quantum state, but in a statistical mixture of several states. These statistical mixtures are called mixed states.

Mixed States and Density Matrices

There is a fundamental difference between a mixed state and a superposition of pure states. Assuming two pure states $|\psi\rangle$, $|\phi\rangle$, the superposition $1/\sqrt{2}(|\psi\rangle + |\phi\rangle)$ is also a pure state and different from a statistical mixture of 50% state $|\psi\rangle$ and 50% state $|\phi\rangle$. A statistical mixture can be associated with a density matrix ρ, a Hermitian positive semi-definite operator of trace one. For a mixture of the pure states $|\psi_j\rangle$ occurring with probabilities η_j, the density matrix ρ of the mixed state is given by

$$\rho = \sum_j \eta_j |\psi_j\rangle\langle\psi_j|. \tag{2.56}$$

When a measurement associated with the measurement operators $\{M_m\}$ is performed on state ρ, the probability to obtain outcome m is given by

$$p_\rho(m) = \sum_j \eta_j \langle \psi_j | M_m^\dagger M_m | \psi_j \rangle = \text{Tr}\left(M_m^\dagger M_m \rho \right). \tag{2.57}$$

After measurement of outcome m the system is collapsed to the state

$$\rho'_m = \frac{M_m \rho M_m^\dagger}{\text{Tr}\left(M_m^\dagger M_m \rho \right)}. \tag{2.58}$$

To completely identify an arbitrary state one has to know all elements of its density matrix. However, there are some fundamental difficulties to measure all these entries performing measurements on a single quantum system.

Measurement Issues

For a quantum system in a state space of dimension n the corresponding density matrix ρ consists of $n \times n$ elements. All these have to be determined to completely identify ρ. However, there are two main obstacles:

1. The collapse of the wave function: When performing a measurement on a quantum object, the state is altered, i.e. after the measurement it is in a different state than before (see postulate 3). Additional measurements can only be performed on this new state.

2. The no-cloning theorem: It is not possible to copy an unknown quantum state on another system without altering the initial state.

That means, for a quantum system in an unknown state only one measurement can be performed; after that it is not any longer in the initial state. The initial state cannot be copied before doing the measurement.

One strategy to characterise the state of such a quantum system can be to prepare the system more than once assuming that all such systems be in the same state, i.e. they have the same density matrix. This matrix can then be reconstructed by doing one measurement on each system. However, this can be quite tedious, since the number of measurements necessary depends on the dimensions of the density matrix, and it is not applicable when the preparation cannot be done sufficiently often in the same way. Such a reconstruction of the density matrix is called quantum tomography. An overview about different techniques can be found in [25].

If some information about the state is known previously, other approaches might be more convenient. For example if the state in question is known to be one from a certain set of states, one would perform a measurement which discriminates the states from this set with the lowest possible error probability. For orthogonal states, this error probability can be zero. For non-orthogonal states, there will always be a non-zero

error probability, at least as long as one does not allow for inconclusive results. On the expense of allowing for inconclusive results, it might even be possible to discriminate non-orthogonal states with a vanishing error probability. These strategies will be discussed in more detail in chapter 6.

3 Single-Photon Sources

In the previous chapter it has been discussed that single-photons are light states which obey specific statistics. A single-photon source emits photons in a way that the probability to find a photon just after a first one has been present is highly reduced (cf. section 2.2.2).

In this chapter emitters are presented which provide these non-classical states of light. Two different types of single-photon sources are discussed in more detail: semiconductor quantum dots and the nitrogen-vacancy centre in diamond.

3.1 Introduction to Single-Photon Emitters

In section 2.2.2 it was shown that there is a fundamental difference in the photon statistics of classical light states and a single-photon number state. Single photons can thus not be obtained by just taking "a lot of light" from a bright (classical) source like a bulb or a laser and attenuating it until there is on average only one photon per detection time unit. Attenuation does not modify the statistical properties, but only lowers the average photon number, so attenuated light from a bulb would still obey thermal, and that from a laser Poissonian statistics. A single photon number state, on the other hand, contains always exactly one photon in the optical mode, without any statistical spread (cf. figure 2.3). Hence it takes more than a classical source and a strong attenuator to obtain true single-photon states. A very nice overview of single-photon sources in general can be found in [26].

3.1.1 Requirements for the Ideal Single-Photon Emitter

The ideal single-photon emitter would have a lot of properties that can be met only in parts by real sources. For different applications different characteristics are of more importance and this determines the choice of the actual source. Nevertheless, the ideal emitter would possess all these features:

Quantum efficiency: For the ideal source the emission probability for a single photon in the optical mode is 100%, the emission probability for multiple photon emission equals 0%.

Emission on demand: An ideal source is deterministic, i.e. it emits photons on demand with no jitter at a time defined by the user.
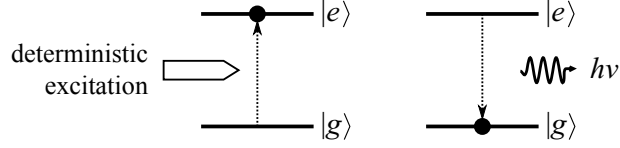
Figure 3.1: On-demand single-emitter source: An excited state $|e\rangle$ of a two-level system is pumped deterministically. When it decays spontaneously to the ground state $|g\rangle$, a single photon is emitted.

Fourier-limited emission line: The emission linewidth $\Delta\omega$ is given by the temporal widths $T = 2/\Delta\omega$ of the photons as described by the Wiener-Khinchin theorem (equation 2.37). T is determined by two specific times, the radiative lifetime T_1 of the emitter's excited state, and the dephasing time T_2 due to incoherent processes as e.g. phonon interactions, carrier scattering etc. The coherence time T of the emitted photons is given by

$$\frac{1}{T} = \frac{1}{2T_1} + \frac{1}{T_2}. \tag{3.1}$$

For an ideal source the dephasing time $T_2 \to \infty$, i.e. the emission linewidth is given only by the radiative lifetime T_1.

Wavelength range / tuning: For some applications a specific wavelength (range) may be required, e.g. for loss-free transmission in optical fibres, or the photon wavelength needs to overlap with a certain transition line. An ideal source-system is available in a variety of wavelengths and can be tuned spectrally.

3.1.2 Real Single-Photon Sources

In reality single-photon sources do not meet all the requirements one has in mind for the ideal emitter. However, since single-photon emission was demonstrated for the first time in 1977 [27] a lot of effort has been put into the development of different kinds of emitters to draw near the ideal one. A good overview of the types of sources available nowadays can be found in [28].

On-Demand Single-Emitter Sources

Many single-photon sources rely on single emitters with two discrete internal energy levels as shown in figure 3.1. An upper level $|e\rangle$ can be pumped deterministically and decays to the ground state $|g\rangle$ emitting a photon. Fluorescence from a single emitter with this energy structure exhibits single-photon statistics.

Single neutral atoms or ions are systems with energy levels similar to the one depicted in figure 3.1. Their electronic structure allows only certain energy states for
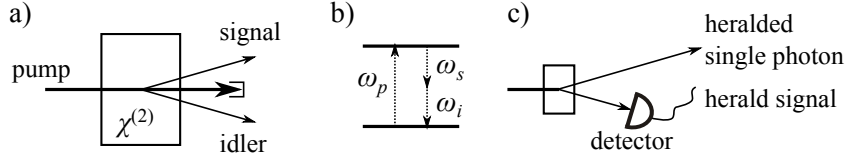
Figure 3.2: Parametric down-conversion: A pump photon of frequency ω_p is converted into two photons (signal of frequency ω_s and idler, ω_i) in a non-linear process (a) under the constraints of energy (b) and momentum conservation. The photon pair created in the process can be utilised as a source of heralded single photons (c).

the electrons and thus relaxations from higher to lower energy states can be used for single-photon emission [29–32]. Single-photon sources based on single neutral atoms or ions have the advantage that the emitters are all identical and thus can provide indistinguishable photons [33]. The disadvantage of these sources is that sophisticated trap systems are required to isolate the single emitter, which makes the sources not easy to integrate in more feasible setups or e.g. solid-state cavities.

As single atoms, single molecules can also serve as quantum emitters [34–36]. Due to different vibrational levels of the electronic states, a broad spectrum of transitions is spanned. However, most molecules exhibit blinking (due to the existence of additional dark states) and photo-bleaching, which reduces their utility.

An alternative to single atoms or molecules are solid-state single-photon emitters. A promising system are colour centres in diamond [20, 37, 38]. They consist of complexes in the diamond lattice where carbon atoms are replaced by other atoms or vacancies, exhibiting electronic structures with a discrete level scheme. The most common one is the nitrogen-vacancy centre, consisting of a nitrogen atom with an adjacent vacancy. This single photon emitter is discussed in more detail in section 3.3. The main advantage of these sources is that they emit single-photons at room temperature.

Last but not least, there is a broad variety of quantum dots, which can be employed as single-photon emitters. Quantum dots are semiconductors with extensions so small that carriers are confined in all three spatial dimensions, which results in a discrete energy spectrum [39–42]. They are described more extensively in section 3.2.

Other Sources

Although it might be the straightforward approach to use single emitters to produce single light quanta, single photons can also be generated in multiple emitter systems. These sources usually employ a classical pump beam to produce output photons with a certain probability. This means that the photons are not generated on-demand but in a probabilistic manner. Also the emission statistics may not be non-classical. A solution to these difficulties is to use processes in which photon pairs are generated. Then one photon can be used to herald the other one and the resulting conditional probability distribution obeys the non-classical single-photon statistics.

a)   b)
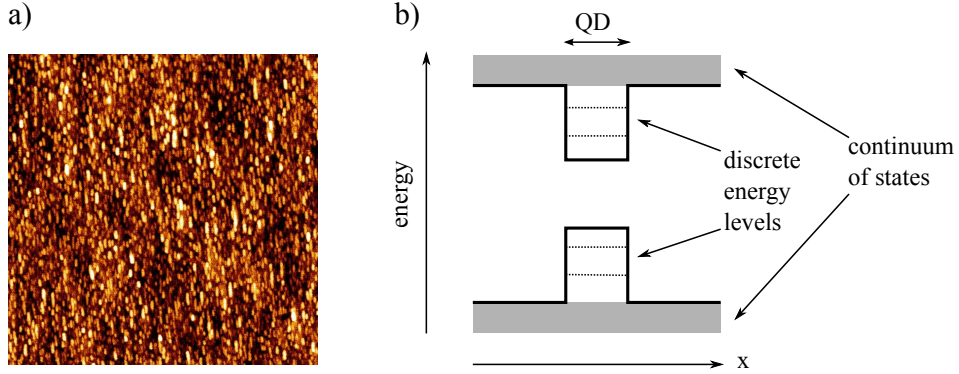
Figure 3.3: (a) 5 μm × 5 μm AFM picture of GaInP QDs on a GaP substrate. (b) Energy level structure of a QD in a semiconductor matrix with a higher band gap. Inside the dot there are quantised energy levels. The continuum of states in conduction and valence band are indicated in grey.

There are different schemes to obtain single photons from multiple emitter ensembles. One possibility is to use laser cooled atomic ensembles in a magneto-optical trap. In the ensemble heralded single photons can be produced via an off-resonant Raman transition [43, 44]. Another possibility to produce photon pairs is using four wave mixing in optical fibres [45, 46].

For quantum information applications, single photons are often obtained from spontaneous parametric down-conversion [47, 48]. In this setting a pair of two low energy photons is generated from one high energy photon in a non-linear process (figure 3.2). If one photon from the pair is used to herald the other one, this configuration can be utilised as a single-photon source [49].

3.2 Semiconductor Quantum Dots

A quantum dot (QD) is a solid state structure in which carriers are confined in all three dimensions. They consist of semiconducting material with a band gap modulation which results in carrier confinement. Usually, small islands of a semiconducting material are fabricated in a semiconducting matrix with a larger band gap. The energy levels of carriers become quantised when the confinement length is on the order of the de Broglie wavelength λ_{dB} of the carriers which is typically in the order of 10 nm-100 nm [50]. An atomic-force microscope (AFM) picture of InGaP QDs on a GaP substrate is shown in figure 3.3a. In figure 3.3b the energy level scheme is sketched. Inside the QD energy levels are quantised whilst in conduction and valence band of the matrix a continuum of states is available.

Due to their discrete energy spectrum QDs are sometimes denoted as "artificial atoms". Like single atoms, single QDs can serve as single photon emitters when an

a) b) c) d)
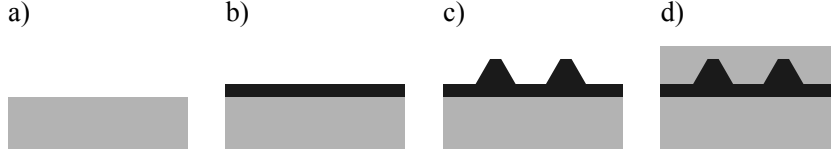
Figure 3.4: Stranski-Krastanov growth: On a semiconducting substrate (a) another semiconducting material with a slightly different lattice constant is deposited. After a few monolayers are grown (b), instead of uniform deposition small islands are formed (c) to release the stress due to the difference in lattices constants. The dots are capped with the substrate material (d).

electron-hole pair recombines emitting a photon. The advantage compared to single atoms is that QDs are spatially fixed inside a solid state matrix, and do not have to be retained using a complex trap geometry.

Nowadays QDs can be fabricated for a broad range of emission wavelengths. Nitride compounds as InGaN/GaN systems [51] cover the visible range, where also CSe/ZnSe dots (around 500 nm) [52] or InP/GaInP dots (650 nm-700 nm) [53] emit. In the near IR, In(Ga)As/GaAs (900 nm-1500 nm) [54–56] and InAs/InP (around 1500 nm) [57] compounds can be utilized.

Often the emission properties of QDs are improved by embedding the dots in cavity structures [58–61]. The cavity modifies the density of states and can thus enhance the dot's emission into a specific mode.

3.2.1 Fabrication

Here we focus on epitaxial QD growth since this is the method how dots for single-photon emission are commonly produced. A good overview about the growth process is given in [50]. In the epitaxial deposition one semiconducting material A is grown on the surface of another material B with a higher band gap, e.g. by thermal evaporation using molecular beam epitaxy (MBE) where atoms or molecules are deposited on the surface in an ultra-high vacuum atmosphere, or metal organic vapour phase epitaxy (MOVPE) where they are brought to the surface in a carrier gas (usually hydrogen or nitrogen). When depositing material A on B, one can classify three types of film growth depending on surface and interface tension: A can grow on B layer-by-layer (Frank-van-der-Merve growth), or can form islands (Volmer-Weber growth), or can form islands on a layer (Stranski-Krastanov growth). The QD utilised here (and in most cases) are Stranski-Krastanov (SK) grown as shown in figure 3.4. Material A (e.g. GaInAs) is deposited on substrate material B (e.g. GaAs), which has a slightly different lattice constant. When the A-film is few monolayers thick, the strain in the film due to the lattices constant mismatch leads to the formation of islands. The deposition is stopped when the islands have sizes small enough to form a potential well for carriers in all three dimensions. In order to establish a well-defined confinement,
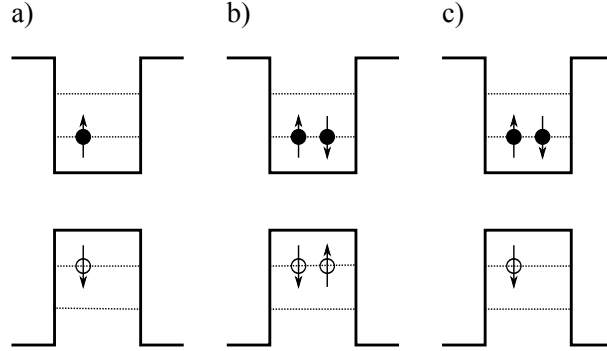
Figure 3.5: Excitations of a quantum dot: a) exciton, b) biexciton, c) (negatively) charged exciton.

the QDs are capped with the substrate material B.

Another possibility to fabricated QDs can be to deposit a layer of low band gap between barriers of a higher band gap material. Due to interface roughness fluctuations in the layer thickness occur which can result in lateral carrier confinement [62, 63]. However, trapping potentials are small compared to SK grown QDs. Another approach is to grow QD in nano-wires. The wires are produced using MOVPE on a gold droplet which acts as a catalyst [64]. Single-photon emission has been observed from these wire structures [65]. Colloidal QDs [66] can be synthesized from precursor compounds dissolved in a solution. By heating the precursors are transformed to monomers from which nano-crystals can be grown. Colloidal QDs are quite unstable due to surface effects as charge carrier trapping or quenching and therefore usually not suitable as single-photon sources.

3.2.2 Excitonic States and Excitation

Depending on the amount of carriers trapped inside the QD, different excited states are possible. Some of them are depicted in figure 3.5. The lowest excited state, the exciton, consists of one electron-hole pair (figure 3.5a). The state with two electron-hole pairs is called biexciton (figure 3.5b). Excited states can be uncharged (when there are as many holes as electrons present in the dot) and charged (when the amount of electrons and holes differ, e.g. figure 3.5c).

The spin of the exciton in z-direction (the growth direction of the QD) is composed of the spin of the exciton ($\pm 1/2$) and the one of the heavy hole ($\pm 3/2$), which results in four possible exciton spins of ± 1, ± 2. Only the states with spin ± 1 couple to the light field. Exciton states with spin ± 2 are called dark excitons.

The ideal dot grown in z-direction is symmetrical in the x-y-plane. In this case of a perfectly cylindrical dot the spin states $|\pm 1\rangle$ are degenerate. However, in reality most dots do no show this perfect symmetry. This leads to a fine structure splitting between
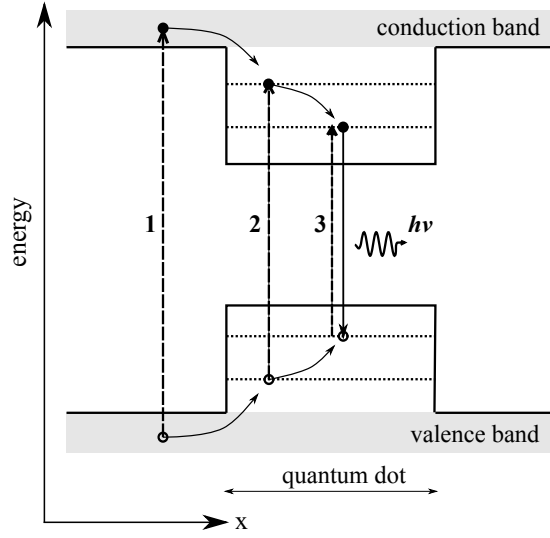
Figure 3.6: Excitation of a QD: The dot is excited either via off-resonant pumping (1), or quasi-resonant pumping to higher states in the QD (2), or resonant pumping to the lowest QD state (3). Carriers relax non-radiatively to the lowest energy state.

the bright exciton states $|e_1\rangle = (|+1\rangle - |-1\rangle)/\sqrt{2}$ and $|e_2\rangle = (|+1\rangle + |-1\rangle)/\sqrt{2}$, typically in the order of $\delta = 0\ldots 100~\mu$eV [67]. The biexciton state is a spin-singlet state which does not show a fine-structure splitting. It is very interesting to have dots with a vanishing fine structure splitting between the exciton states because they can be employed as on-demand sources of entangled photons [68].

Excitation Modes

Carriers in the quantum dot can be created by optical or electrical pumping, either continuously or pulsed. For off-resonant pumping, an electron-hole pair is created by exciting one electron to the conduction band outside the QD (figure 3.6). Carriers are captured by the QD and relax to the lowest energy level inside the dot non-radiatively. This takes place on short time scales (1 ps-100 ps) [67]. Using off-resonant pumping, excitations in a QD can be created easily. However, other carriers produced in conduction and valence band can be trapped close to the dot, resulting in a spectral shift of the QD's emission (spectral diffusion). For suppressing spectral diffusion, quasi-resonant pumping to a higher QD state (figure 3.6) has an important advantage. Here, no carriers are produced outside the dots. It it possible to occupy the QD with an electron-hole pair in a controlled way. For resonant excitation the lowest QD energy level is directly excited (figure 3.6), thus no additional relaxation is necessary to reach the lowest exciton state, but in this scheme it is very difficult to filter out the excitation light.

3.2.3 Single Photons from a Quantum Dot

A single QD can serve as a deterministic single-photon emitter: an exciton with total spin ± 1 in the QD recombines emitting a single photon. The QD can be excited deterministically using e.g. a pulsed laser. To obtain single photons one has to make sure to collect light from only one QD. Hence a low density QD sample must be utilised. Possibilities to lower the dot density after growing the dots is e.g. to etch pillars of diameters of the order of 100 nm or to superimpose the substrate with a mask layer [67].

Figure 3.7 depicts our setup for QD characterisation. SK grown QDs are operated at cryogenic temperatures, because otherwise trapped carriers would be able to escape the QD by thermal excitation before they recombine radiatively. Therefore the QD sample is mounted in a cryostat and kept at around 7 K. The sample can be excited either electrically or optically, and the fluorescence can be collected with a CCD camera, a spectrometer, or it is sent to a Hanbury-Brown-Twiss (HBT) setup to measure photon statistics. For the measurements described later in this thesis, an electrically pumped InGaAs QD in a GaAs matrix was utilised.
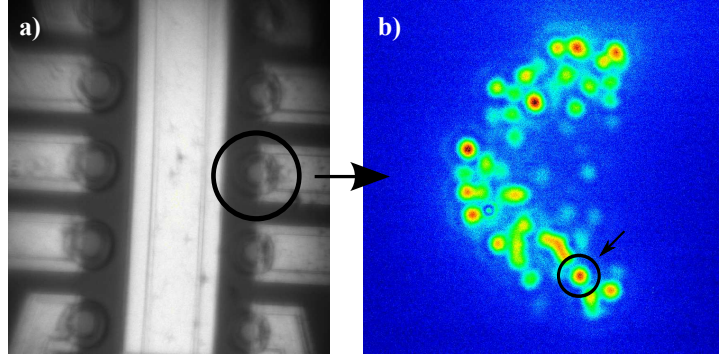
Figure 3.8 shows pictures of the sample taken with the CCD camera. The structure contains ten diode structures with QDs embedded in a cavity formed by two distributed Bragg reflectors, as described in detail in [69]. The cavity lowers the lifetime of the excited state and enhances the emission into the cavity modes. The diodes can be seen in figure 3.8a. Figure 3.8b shows the fluorescence from one of the diodes when 1.6 V are applied. Different QDs are excited at the same time. To obtain a single-photon source, a single one of them is filtered out using a 100 nm pinhole.

Figure 3.9 shows the emission spectrum of the dot marked in figure 3.8b with and without spectral filtering. The emission wavelength corresponds to the energy difference between ground state and excited state. Since the sample is kept at around 7 K, spectral broadening due to phonons does not play a major role. The main source for broadening of the natural linewidth are carrier fluctuations in the vicinity of the dot. Spectral linewidths of QDs can be measured interferometricly (see section 2.2.1).

To prove single-photon emission, the intensity auto-correlation function $g^{(2)}(\tau)$ has to be measured (see section 2.2.2). This is commonly done using a HBT setup, as described in detail in section 5.1.1. The QD's emission is sent on a non-polarizing 50:50 beam splitter with two single-photon detectors in its outputs (figure 3.7). From the time differences of clicks in detectors 1 and 2 the $g^{(2)}$-function can be obtained. Figure 3.10 shows a $g^{(2)}$-measurement for the InGaAs QD. An antibunching feature is observed with a minimum clearly below 0.5 indicating single-photon emission according to equation 2.46. The width of the antibunching dip is determined by the lifetime of the excited state and the time resolution of the detection unit. Here the depth is mainly given by the detection time resolution, but in general also stray light and dark counts of the detectors could play a role. The fit in figure 3.10 assumes that the measured data is a convolution of the ideal antibunching curve $1 - \mathrm{e}^{-\gamma|\tau|}$, with γ being the inverse lifetime of the excited state, and a Gaussian distribution of width 800 ps,
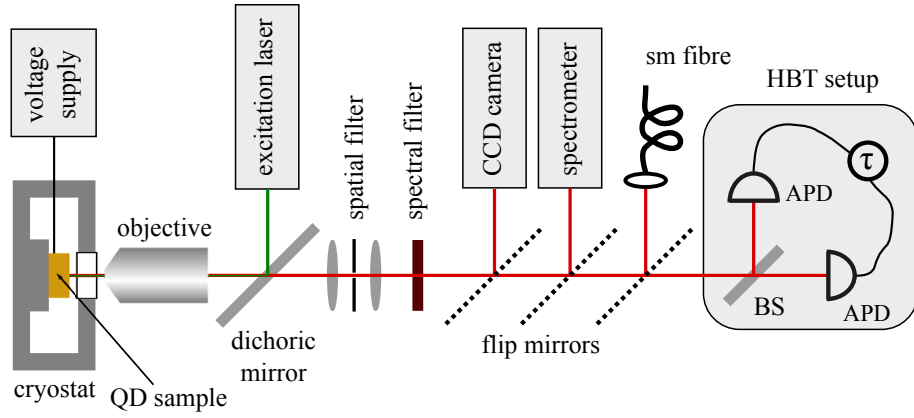
Figure 3.7: Setup for characterising QD single-photon sources. The QD sample is mounted in a cryostat. The QDs can be excited electrically applying an appropriate voltage or optically using an excitation laser. The luminescence is collected with an objective of numerical aperture 0.75 and can be filtered spatially using a pinhole and spectrally using interference filters. The light from the sample can be sent to a CCD camera, a spectrometer, or a Hanbury-Brown-Twiss (HBT) setup consisting of a 50:50 beam splitter (BS) and two avalanche photodiodes (APDs) for measuring the photon statistics (see section 5.1.1). The fluorescence can also be coupled into a single-mode (sm) optical fibre for sending the single photons to different experimental setups (as e.g. the ones described in sections 6.2.1 and 6.3.1).

Figure 3.8: Images of the QD sample taken with the CCD camera. (a) White light photo of the diode structure: the sample contains ten diodes with QDs. The bright lines are electrical connections. (b) Fluorescence from diode no. 8 when 1.6 V are applied. The QD utilised here is marked. For the experiments, it was filtered out spatially using a 100 nm pinhole.

a)

b)
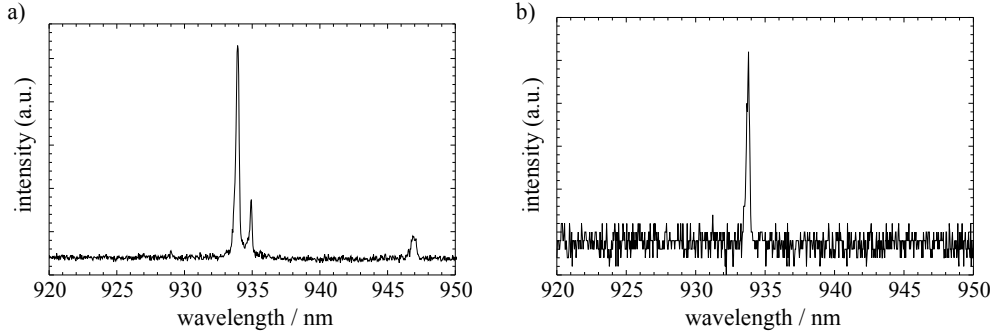
Figure 3.9: Spectrum of an electrically pumped InGaAs QD taken (a) without spectral filtering and (b) with a bandpass filter of width 1 nm at 934 nm.

which is the time resolution of the detection unit. Thus the only fit parameter is γ. For this measurement the fit renders a value of $\gamma^{-1} = 1$ ns for the lifetime of the excited state. This slight bunching observed on the left of the antibunching dip is due to cross talk between the detectors.

The electrically pumped InAs QD described here was employed as single-photon source for the state-discrimination experiments discussed in sections 6.2.1 and 6.3.1.
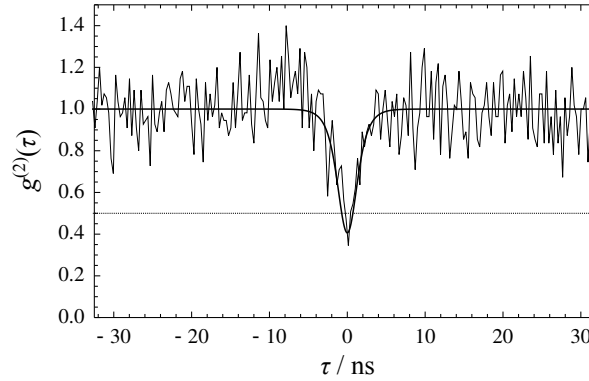
Figure 3.10: Single-photon emission from a quantum dot: An antibunching feature is observed in the $g^{(2)}$-measurement for light emitted by a continuously pumped InGaAs QD. $g^{(2)}(0) < 0.5$ (dashed line) indicates single-photon emission. The remaining counts at time differences $\tau = 0$ are mainly due to the limited time resolution. The slight bunching observed on the left of the antibunching dip is due to cross talk between the detectors: sometimes one APD emits a light pulse upon detection of a photon which can trigger the other APD.
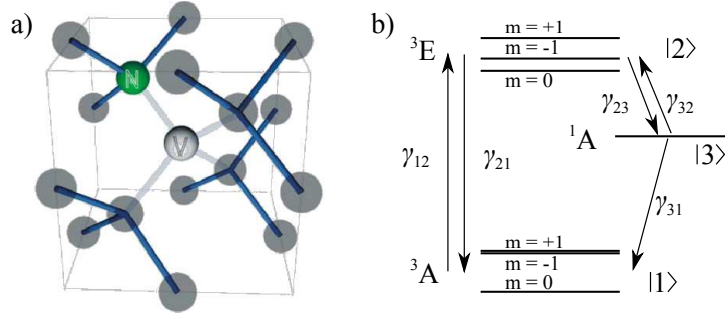
Figure 3.11: (a) Structure of the N-V$^-$ centre (from [20]). In the diamond lattice one carbon atom is replaced by a nitrogen atom with an adjacent vacancy. (b) Energy levels of N-V$^-$ centre. Luminescence is observed from the $|2\rangle \rightarrow |1\rangle$ transition between to triplet states whilst at least one dark single state ($|3\rangle$) is present.

3.3 The Nitrogen-Vacancy Centre in Diamond

Diamond is an outstanding material because of its exceptional physical characteristics, as e.g. its extreme hardness and thermal conductivity. Furthermore, it has striking optical properties, in particular a high refractive index of $n = 2.42$ (at 600 nm) and a wide transparency window down to around 200 nm due to its large electronic band gap of 5.5 eV [70].

In the diamond lattice, defect centres can be formed by impurity atoms replacing diamond atoms, sometimes accompanied by vacancies in the lattice. Nowadays, hundreds of these centres are known to be luminescent [20]. The defect centres possess discrete electronic energy states, hence single colour centres can serve as single-photon sources. For optical applications, they are appealing since they can be operated at room temperature and they emit in the visible wavelength range without bleaching. The most common among them is the nitrogen-vacancy (N-V) centre, where a nitrogen atom replaces a diamond atom in the lattice with an adjacent free lattice site [20] as shown in figure 3.11a. Due to its remarkable optical and spin properties it is a promising candidate for room temperature quantum information processing [71]. N-V centres are present in most natural and synthetic diamonds but their concentration can further be increased by irradiating the diamond with high-energy particles followed by annealing at around 700°C [72]. In the following, an overview of N-V centres as single-photon emitters is given.

3.3.1 Electronic Structure

Two different charge configurations occur for the N-V centre: the neutral (N-V^0) and negatively charged (N-V$^-$) centre with the additional electron presumably provided by other nitrogen atoms in the vicinity of the N-V centre [73, 74]. Therefore it depends on the amount of nitrogen defects in the diamond lattice which configuration is

predominant. For our experiments nitrogen-rich diamonds were used, thus the N-V$^-$ centre was the dominant one.

The electronic structure of the N-V centre is still not understood completely and subject to intense experimental and theoretical research [75–81]. The N-V$^-$ centre shows a zero-phonon line (ZPL) at 637 nm which is induced by a transition between a triplet excited state ^{3}E and the triplet ground state ^{3}A (figure 3.11b). At least one other dark singlet state (^{1}A) is present. All the transitions are sketched in figure 3.11b. The decay rate γ_{23} from $|2\rangle$ to the dark state $|3\rangle$ depends on the spin state of $|2\rangle$. For the decay $|3\rangle \rightarrow |1\rangle$, usually ^{1}A decays to the $m = 0$ spin state ^{3}A$_{m=0}$ [77]. These spin dependencies together with long spin dephasing times of up to milliseconds even at room temperature [82] allow for controlled preparation and optical readout of the spin which can be utilised to implement quantum information processing [82–88].

In this work, the N-V centre was employed as a single-photon source. However, also with respect to the statistical properties of light emitted by a single N-V centre, the presence of the dark state $|3\rangle$ plays a role. The features of the N-V centre as a room-temperature single-photon emitter are discussed in the next paragraph.

3.3.2 Single-Photon Emission

Single-photon emission from colour centres in diamond was for the first time shown in 2000 by Kurtsiefer et al. for the N-V centre [37]. Later non-classical light emission was also observed for other defect centres as the nickel-nitrogen complex [89], the silicon-vacancy centre [90], and the chromium centre [91]. The striking feature of these sources is that they emit single photons at room temperature (in contrast to self-assembled semiconductor QDs) without exhibiting photobleaching (in contrast to single molecules or colloidal QDs).

Figure 3.12 depicts our setup for characterisation of the N-V centres. Nano-diamonds of a size of a typically between 20 nm and 35 nm are spin-coated on a coverslip. Around 1% of them contain a single N-V centre. The sample preparation is described in detail in [92]. The N-V centre is excited at 514 nm using a Ar-ion laser, and the fluorescence is collected with an oil immersion objective. It can be sent to a CCD camera, a spectrometer, or to a Hanbury-Brown-Twiss (HBT) setup to measure photon statistics. It can also be coupled into a single-mode optical fibre as for the measurement described in section 5.2.

In figure 3.13a a typical room temperature spectrum of a N-V centre is shown. Both the ZPL of the N-V^0 centre at 576 nm and the ZPL of the N-V$^-$ centre at 637 nm can be identified, but most of the emission is into the bright phonon sideband. The presence of both ZPLs in the spectrum of a single centre indicates a continuous conversion between both charge states. To understand the intensity auto-correlation function depicted in figure 3.13a, the energy level structure of the N-V centre has to be taken into account. This is done in the next paragraph.
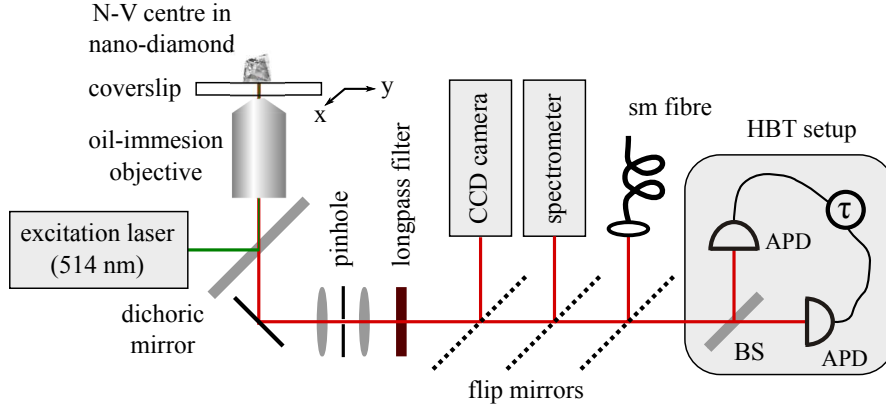
Figure 3.12: Setup for characterising N-V-centre single-photon sources. Nano-diamonds containing N-V centres are spin-coated on a coverslip mounted on a translation stage, to move the sample in order to identify a nano-diamond containing a single N-V centre. The N-V centre is excited optically with a Ar-ion laser at 514 nm. The fluorescence is collected with an oil-immersion objective and can be filtered spatially using a pinhole. The excitation light is blocked out with a 570 nm longpass filter. The fluorescence can be sent to a CCD camera, a spectrometer, or a Hanbury-Brown-Twiss (HBT) setup consisting of a 50:50 beam splitter (BS) and two avalanche photodiodes (APDs) for measuring the photon statistics (see section 5.1.1). The fluorescence can also be coupled into a single-mode (sm) optical fibre for sending the single photons to different experimental setups (as the one described in section 5.2).
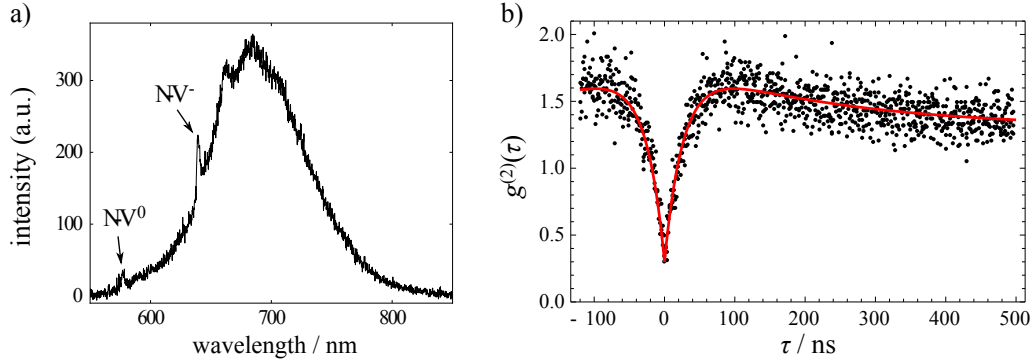
Figure 3.13: (a) Room temperature emission spectrum of a single N-V centre: both ZPLs can be observed at 576 nm and 637 nm, respectively. Most of the emission is into the phonon sideband. (b) Measurement of the $g^{(2)}$-function. Single-photon emission is observed clearly. The bunching is due to the presence of the dark state. The red line is a fit according to the rate-equation model described in the text.

3 Single-Photon Sources

Rate Equation Model

For operation at room temperature and optical pumping far off resonance, coherent effects do not have to be taken into account. Hence a rate equation model can by applied for the populations n_1, n_2, n_3 of states $|1\rangle$, $|2\rangle$, and $|3\rangle$ (figure 3.11b):

$$\frac{\mathrm{d}n_1(t)}{\mathrm{d}t} = -\gamma_{12}n_1(t) + \gamma_{21}n_2(t) + \gamma_{31}n_3(t) \tag{3.2}$$

$$\frac{\mathrm{d}n_2(t)}{\mathrm{d}t} = \gamma_{12}n_1(t) - (\gamma_{21} + \gamma_{23})n_2(t) + \gamma_{32}n_3(t) \tag{3.3}$$

$$\frac{\mathrm{d}n_2(t)}{\mathrm{d}t} = \gamma_{23}n_2(t) - (\gamma_{31} + \gamma_{32})n_3(t). \tag{3.4}$$

Since the photons are emitted at the transition $|2\rangle \to |1\rangle$, the autocorrelation function $G^{(2)}(\tau)$ (equation 2.33) for the photon flux is here given by the population n_2 of the excited state and the emission rate γ_{21}

$$G^{(2)}(\tau) = \gamma_{21} \cdot n_2(\tau). \tag{3.5}$$

For $\tau \to \infty$ the normalised intensity autocorrelation function $g^{(2)}(\tau)$ equals 1 (see section 2.2.2). Assuming the initial conditions $n_1(0) = 1$, $n_2(0) = 0$, and $n_3(0) = 0$, a solution for $g^{(2)}(\tau)$ is given by [20, 93, 94]

$$g^{(2)}(\tau) = \frac{G^{(2)}(\tau)}{G^{(2)}(\tau \to \infty)} = 1 + Ce^{-\Gamma_2\tau} + (1 - C)e^{-\Gamma_3\tau}, \tag{3.6}$$

with the coefficient and decay times being [93]

$$C = \frac{\Gamma_3(\gamma_{31} + \gamma_{32} - \Gamma_2)}{(\gamma_{31} + \gamma_{32})(\Gamma_2 - \Gamma_3)} \quad \text{and} \tag{3.7}$$

$$\Gamma_{2,3} = \frac{1}{2}(A \pm \sqrt{A^2 - 4B}) \tag{3.8}$$

using the abbreviations

$$A = \gamma_{12} + \gamma_{21} + \gamma_{23} + \gamma_{31} + \gamma_{32} \quad \text{and} \tag{3.9}$$

$$B = \gamma_{12}(\gamma_{23} + \gamma_{31} + \gamma_{32}) + \gamma_{21}(\gamma_{31} + \gamma_{32}) + \gamma_{23}\gamma_{31}. \tag{3.10}$$

Here, the $g^{(2)}$-function is determined by all the transition rates γ_{12}, γ_{21}, γ_{23}, γ_{31}, and γ_{32}. $g^{(2)}(0) = 0$ indicates single-photon emission. The presence of the third state $|3\rangle$ induces an additional bunching feature in the $g^{(2)}$-function.

Figure 3.13b shows a measured intensity autocorrelation function of a N-V centre using a standard HBT setup (see section 5.1.1). Antibunching is observed with a dip depth of 0.2, clearly indicating single-photon emission (cf. section 2.2.2). Compared to the $g^{(2)}$-measurement of a typical SK grown QD (figure 3.10), the width of the

antibunching dip is very large for the N-V centre, which is due to its long lifetime. In bulk diamond the lifetime is known to be around 12 ns [95]. The defect centres utilised here, were located inside a nano-diamond of a diameter of a few 10 nm. Lifetimes of the excited state of 30 ns to 50 ns were observed. Equation 3.6 was used to fit the measurement, but there was a constant background assumed as another fitting parameter due to stray light and detector dark counts.

4 Nanowire Superconducting Single-Photon Detectors

For detection of light at the single-photon level, different types of detectors are utilized. There are basically two different classes of detectors, exploiting either the photoelectric effect or the fact that absorption of light can disrupt superconductivity. This chapter deals with one of the latter. Firstly, an overview of the important characteristics of single-photon detectors and of different types of detectors is given. In the second section, nanowire superconducting single-photon detectors (NSSPDs) are discussed in more detail theoretically. In the next section, detector layout and electronics for the NSSPDs used in this work are described, and a technique to couple a single-mode optical fibre to a NSSPD is introduced. In the last section, details about the performance of our NSSPDs are given.

4.1 Introduction of Single-Photon Detectors

The energy of a single photon is given by the Planck constant h times the photon's frequency ν, i.e. $E_{ph} = h\nu$. For a photon of wavelength of $\lambda = 600$ nm this energy equals $E_{ph} = 2$ eV. It is a challenging task to detect as small an energy. However, there are a lot of applications requiring the ability to measure single photons nowadays, ranging from single-molecule detection to quantum information processing. Various single-photon detectors have been developed based on different technological approaches. Often a trade-off between different qualities of the detector have to be found to obtain a device that suits the experimental needs. A good overview of the current state of the art can be found in [96], whereas in [97] the well-established detector types are discussed more deeply.

4.1.1 Characteristics of a Single-Photon Detector

Different detector types posses very different qualities, depending on their working principle and the materials used. A bunch of parameters quantifies the performance of a single-photon detector. In particular, there are six main characteristics:

Detection efficiency. The detection efficiency η is the probability to register a count when a photon impinges on the detector. It can be quite challenging to measure η because of the difficulty to determine the number of incoming photons. Possible experimental solutions are to compare the detector with a detector of known quantum

efficiency, to use a calibrated light source or heralded single photons [98, 99].

Dead time. The dead time of the detector is the time it needs to recover its original detection efficiency after a photon has been registered. The dead time limits the speed of the detector, i.e. the maximum number of photons it is able to detect within a certain time.

Timing jitter. The variation of the time difference between a photon hitting the detector and the detector signal being output is denoted timing jitter. It limits the detector's time resolution.

Dark count rate. There is a non-zero probability that the detector generates an output signal although no photon has been absorbed. These counts are called a dark counts.

Spectral range. Depending on their constituent materials detectors are only sensitive to photons of a certain spectral range. The smaller the photon's energy the more difficult is its detection. But especially the low energy IR photons of wavelength 1.55 μm are of interest in many applications since losses in optical fibres are lowest there.

Photon number resolution. Most single-photon detectors can only distinguish between zero and 'one or more' photons. However, for quantum information applications like linear optical quantum computing [6] and quantum key distribution [1] a photon number resolving detector is crucial.

4.1.2 Current Detector Technologies

There are various technical approaches to build a single-photon detector. When a photon is absorbed at the detector, its energy is used to create an electric signal, e.g. creating carriers in the absorbing material or a change in resistance. In the following, an overview of the four most common devices used in quantum information applications nowadays is given. A more detailed listing can be found in [96, 97].

Photomultiplier Tubes

Photomultiplier tubes (PMTs) are based on the photoelectric effect, i.e. the emission of an electron from a cathode caused by absorption of a photon. A PMT is basically a vacuum tube with a photocathode. The emitted electron is multiplied by a cascade of secondary electron emission generated in a series of electrodes after the photodiode, producing a macroscopic voltage pulse. PMTs cover a spectral range of 115 nm - 1700 nm, but with large differences in performance. In the visible, quantum efficiencies of 40% can be achieved at low dark count rates of 100 Hz and a temporal jitter of 300

ps using GaAsP photocathodes [96]. At 1550 nm, however, the performance of PMTs is relatively poor. Quantum efficiencies of a few percent can be found at a dark count rate of 200 kHz, which results in a very low sensitivity.

Avalanche Photodiodes

Avalanche photodiodes (APDs) are probably the most frequently used single-photon detectors. They consist of semiconductor materials and their working principle is based on the inner photoelectric effect. The configuration of an APD is similar to a pin-diode. Absorption of photons takes place in the intrinsic layer. The absorption of a photon creates an electron-hole pair there. The APD is operated applying a reverse bias voltage usually slightly below the break-down voltage, but for single photon counting slightly above it (Geiger-mode APD). Carriers created in the intrinsic layer by photon absorption are multiplied due to impact ionization. Multiplication factors range from a few 100 for usual APDs up to 10^8 for Geiger-mode devices. The most commonly used material for detection applications in the visible is silicon. With Si-APDs quantum efficiencies up to 70% can be achieved (at 700 nm) at very low dark count rates of around 100 Hz resulting in a high sensitivity of the device. However, the spectral range is limited by the band gap in silicon; only photons of wavelengths up to 1100 nm can be detected, the telecommunication wavelengths at 1300 nm and 1500 nm are outside the spectral range of Si-APDs. For these wavelengths other materials, e.g. InGaAs, have to be used, which have a much poorer performance regarding quantum efficiency (around 20%) and dark counts (1-20 kHz). Dead times are typically in the order of 100 ns.

Superconducting Transition Edge Sensors

Superconducting transition edge sensors (TESs) are superconducting bolometers that were first developed for astronomical applications [100]. They consist of a superconducting material operated very close to the critical temperature, where small changes in temperature result in a large change in resistance. A photon can thus be detected through the small increase in temperature in the material where it is absorbed. Contrary to the other well-established detector types, TESs provide photon number resolution since the change in resistance strongly depend on the energy absorbed [101]. Quantum efficiencies of over 90% are observed in the near IR [102]. However, the disadvantage of this detector type is that it has to be operated at temperatures as low as 100 mK, which requires a very sophisticated experimental setup. For some applications the comparatively long dead time of typically 1 µs [102] might be inconvenient, although also faster detectors with only 190 ns dead time have been reported [103].

Nanowire Superconducting Single-Photon Detectors

The operation principle of nanowire superconducting single-photon detectors (NSSPDs) is similar to the one of TESs. The fact that absorption of a photon can disrupt su-

perconductivity is exploited. In contrast to the TES, a NSSPD is operated well below the superconductor's critical temperature but close to its critical current. The breakdown of superconductivity is a collective effect of the reduction of the cooper-pair density where a photon has been absorbed and an increase of the current density in other regions due to the expulsion of the supercurrent from the low cooper-pair density area. NSSPDs posses a broad spectral range at reasonable quantum efficiencies, low dark count rates, and short dead times. They can be operated at 4.2 K, which makes them much more easy to handle then other superconducting single-photon detectors. The rest of this chapter deals with NSSPDs in more detail, both theoretically and experimentally. In chapter 5 an application of a NSSPD in a very fundamental quantum-optical experiment is presented.

## 4.2 Theory of the Nanowire Superconducting Single-Photon Detector

NSSPDs posses a lot of outstanding characteristics that makes them suitable for many applications in quantum optics, as characterisation of single-photon sources [104–106], quantum key distribution [107, 108], and single plasmon detection [109]. They are able to operate in a very broad wavelength range with a low dark count rate, have short dead times, and a small temporal jitter. Their development started with the investigation of the photoresponse of superconducting thin films [110]; in this context a film is "thin" when its thickness is smaller than the photon's thermalisation length. Nowadays sophisticated nano-patterned structures consisting of up to 17 parallel meandering wires are used for photon detection [111], but since many processes in these patterns are the same as in non-structured thin films, this section starts with a description of the processes taking place in a superconducting film after photon absorption.

4.2.1 Photoresponse of Superconducting Thin Films

When a photon is absorbed in a superconducting film, it breaks a Cooper pair and creates an excited electron with energy close to the photon energy and a low energy quasiparticle. The electron's excitation energy is transferred to other Cooper pairs via electron and phonon scattering and hence the quasiparticle density increases in the area where the photon has been absorbed. The size of this hot spot grows as hot electrons diffuse out of its centre. This formation process competes with the cooling process when electrons loose their energy through electron-phonon scattering and phonons escape into the substrate. Time scales for these processes in a thin NbN layer have been measured by Il'in et al. [112]. An overview of their results is given in figure 4.1.

A first model for describing the evolution of the number of quasiparticles N has been
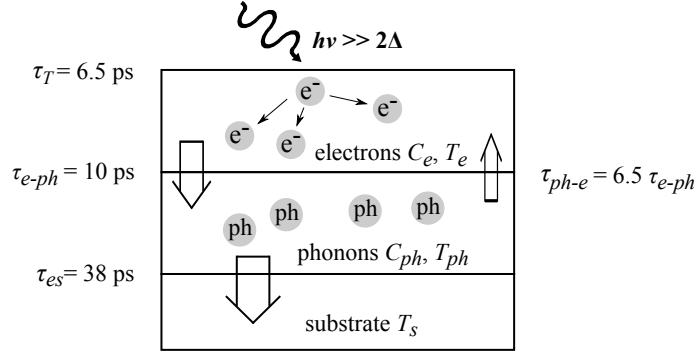
Figure 4.1: Time scales for relaxation processes in NbN thin films (after [112]). The characteristic times are the electron thermalisation time τ_T, the times τ_{e-ph} and τ_{ph-e} for electron-phonon and phonon-electron scattering, and the time τ_{es} for phonon escape to the substrate.

developed by Rothwarf and Taylor [113]

$$\frac{dN}{dt} = I_0 - RN^2 + \beta N_\omega \tag{4.1}$$

$$\frac{dN_\omega}{dt} = \frac{RN^2}{2} - \beta \frac{N_\omega}{2} - \frac{N_\omega - N_{\omega T}}{\tau_\gamma} \tag{4.2}$$

where I_0 is the number of quasiparticles created by photon absorption, R is the quasiparticle recombination coefficient, N_ω is the total number of phonons with energy $\hbar\omega > 2\Delta$, β the probability for breaking of Cooper pairs by such phonons, τ_γ is the characteristic time for phonons to escape to the substrate and $N_{\omega T}$ the thermal concentration of phonons.

Later this model has been refined for temperatures close to the critical temperature T_C, introducing a week perturbation [112, 114]:

$$c_e \frac{dT_e}{dt} = -\frac{c_e}{\tau_{e-ph}(T_e - T_{ph})} + P(t) \tag{4.3}$$

$$c_{ph} \frac{dT_{ph}}{dt} = \frac{c_{ph}}{\tau_{ph-e}}(T_e - T_{ph}) - \frac{c_{ph}}{\tau_{es}}(T_{ph} - T_0). \tag{4.4}$$

Here, T_e and T_{ph} are the electron and phonon effective temperatures, c_e and c_{ph} are the electron and phonon specific heats, $P(t)$ is the perturbation, T_0 is the temperature of the substrate, and τ_{e-ph}, τ_{ph-e}, and τ_{es} are the electron-phonon energy relaxation time, the phonon-electron energy relaxation time, and the phonon escape time to the substrate, respectively. In this model the electron and phonon effective temperatures are assumed to be established instantaneously and to be uniform throughout the sample (2-temperature-model).

Kadin and Johnson firstly proposed a hot-electron single-photon detector based on these effects [110]. In this proposal, a photon absorbed in a superconducting thin film causes a hot spot. The voltage drop across the current-biased film is sensitive to the presence of this hot spot. The disadvantage of this proposal is, that the film has to be operated close to T_C, which makes it difficult to measure the detector response because only small currents can be applied.

4.2.2 Current Assisted Detection in a Superconducting Nanowire

A different detection mechanism was later proposed by Semenov et al. [115]. Here, the detector is operated well below its critical temperature T_C, but biased close to its critical current I_C. It consists of a superconducting wire of width of the order of 100 nm fabricated of a thin film, usually in a meander structure in order to provide an area large enough to focus a light beam on. When a photon has been absorbed, a normal state appears across the wire as a collaborative effect of the hot-spot formation and the bias current.

In figure 4.2 the development of the resistive state after photon absorption is sketched. When a photon is absorbed in the wire, a Cooper pair is broken into a highly excited electron and a quasiparticle (figure 4.2a). The electron scatters with other Cooper pairs creating secondary non-equilibrium quasiparticles. Their concentration increases due to hot-electron thermalisation and a normal-conductive spot is formed when the concentration of non-equilibrium electrons exceeds the normal-conductive state concentration. The supercurrent flows around the hot spot (figure 4.2b). If the bias current is close enough to the critical current, this results in a current density in the vicinity of the normal-conductive spot which exceeds the critical current density (figure 4.2c). Formation of a normal-conductive state across the wire is the consequence (figure 4.2d). The wire will return to the superconducting state when cooling takes place due to phonon escape into the substrate and quasiparticles recombine to Cooper pairs. Formation and collapse of the normal-conducting state can be observed measuring the voltage drop along the wire, which will be non-zero only when the wire is not superconducting.

Hot-Spot Size

A detailed description of formation process and size of the hot spot can be found in [115]. In a wire with a thickness d small compared to the thermalisation length, the flow of non-equilibrium quasiparticles produced by photon absorption can by described by a two-dimensional diffusion equation for the quasiparticle concentration $C(r,t)$

$$\frac{\partial C}{\partial t} = D\frac{1}{r}\left(\frac{\partial C}{\partial r} + r\frac{\partial^2 C}{\partial r^2}\right) + \frac{C - C_0}{\tau} \qquad (4.5)$$

where r is the distance from the point where the photon has been absorbed at $t = 0$, D is the normal state diffusivity, τ^{-1} is the quasiparticle recombination rate, and
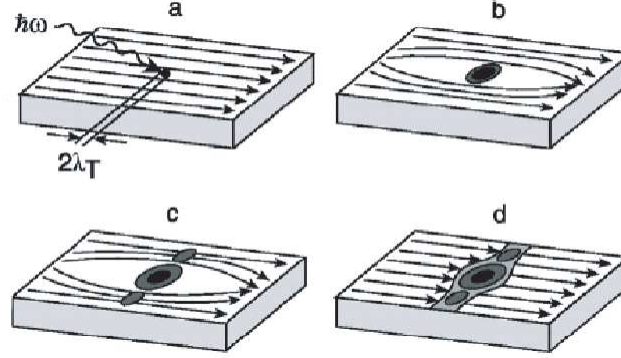
Figure 4.2: Working principle of a NSSPD: Absorption of a photon (a) causes a normal-conducting hot-spot (b). The supercurrent is repelled to the sidewalks where thus the crictical current density is exceeded (c). A normal conducting state is formed across the wire (d). From [116].

C_0 is the equilibrium concentration. Assuming that diffusion and thermalisation are independent, the solution of equation 4.5 is given by

$$C(r,t) = \frac{M(t)}{4\pi Ddt} \exp\left(-\frac{r^2}{4Dt}\right) \exp\left(-\frac{t}{\tau}\right) + C_0. \tag{4.6}$$

Here $M(t)$ is the multiplication factor, i.e. the maximum value $M(t)$ reaches during thermalisation is the quantum yield of the photon absorption process. The radius r_n of the normal-conducting spot is given by $C(r_n, t) = C_n$ where $C_n = N_0 k_B T_C$ is the concentration of equilibrium quasiparticles at the transition temperature T_C and N_0 is the normal metal density of states at the Fermi level.

Considering a wire of width w and critical current I_C, for the minimum radius r_{min} of a normal-conducting spot that is big enough to trigger a detector event at an applied bias current I, follows

$$\frac{w - 2r_{min}}{w} = \frac{I}{I_C}. \tag{4.7}$$

Thus the condition for the hot-spot radius r_n to trigger the detector is given by

$$r_n \geq \frac{w}{2}\left(1 - \frac{I}{I_C}\right). \tag{4.8}$$

Dead Time

In section 4.2.1 times scales have been given for a hot-spot decay to the superconducting state. In a thin NbN film, relaxation times are faster than 100 ps [112]. However, for nano-patterned structures as NSSPDs, much longer recovery times of up to several

nanoseconds are observed [105, 117, 118]. These long restitution times can be understood taking kinetic inductance into account [119]. The origin of kinetic inductance is the kinetic energy of the electrons accelerated by the electric field. In normal metals the kinetic inductance is negligibly small. However, in superconductors the electrons posses a much higher mobility and thus the kinetic induction can be much bigger than in normal metals, depending on the geometry of the device. For a superconducting wire with conductivity $\mathcal{L}_k$ and cross section A along the wire, the kinetic inductance L_K is given by

$$L_k = \mathcal{L}_k \int ds/A(s). \tag{4.9}$$

Kerman et al. [119] investigated detector dead times for different lengths of the meandering nanowire. Their results show that the kinetic inductance is actually the limiting factor for the detector's dead time. The longer the wire, the longer is the NSSPD's dead time. For a typical detector of an active area of 10 μm $\times$10 μm this results in a dead times of around 5 ns.

Hence, a possibility to reduce dead times is to shorten the length of the superconducting wire. On the other hand, a shorter wire results in a smaller active area of the detector, which will be more difficult to focus the light on, and thus in a smaller detector efficiency. A possibility to circumvent this problem is to fabricate detectors which consist of an array of parallel meanders [111, 120, 121]. By making the wires shorter the kinetic inductance can be minimised and dead times can be decreased to of a few 100 ps, i.e. to the time scale of phonon escape to the substrate.

Dark Counts

There are many different sources for dark counts in a NSSPD. Blackbody radiation from the surroundings of the detector is insignificant because the detector is submerged in liquid helium and hence all surrounding parts are kept at 4.2 K. A possible source for dark counts is noise superimposed on the bias current. In the experimental setup, typically efforts are made to reduce this noise by implementing low-pass filters in the bias supply line. Nevertheless, for bias currents extremely close to I_C, contributions to the dark counts due to current noise cannot be suppressed completely.

However, more important contributions to the dark counts are due to intrinsic fluctuations in the superconducting film, mainly fluctuations of the order parameter and thermal excitations of vortex-antivortex pairs (VAPs) [122, 123].

Fluctuations of the order parameter can reduce the Cooper-pair density, resulting in the same effects as a reduction of Cooper pairs due to photon absorption. For fluctuations in a disk-like volume with diameter $2a \geq \xi$, with ξ being the superconducting coherence length, in a strip of width w and thickness d the minimum number of fluctuating Cooper pairs δN_s to trigger the detector is given by [123]

$$\delta N_s = \frac{\pi}{4} awd N_0 \Delta(I,T) \left(1 - \frac{I}{I_C}\right) \tag{4.10}$$

where N_0 is the electron density of states at the Fermi level and $\Delta(I,T)$ equals the gap energy. The probability p of such fluctuations is given by a Boltzmann distribution

$$p \propto \exp\left(-\frac{\Delta F}{k_B T}\right) \tag{4.11}$$

with ΔF being the change in free energy associated with the fluctuation, given by $\Delta F = \delta N_s \Delta(I,T)$.

Magnetic vortices which are not paired in VAPs can be another source of dark counts. In two-dimensional superconducting films, there exists a second transition at temperature $T_{BKT} < T_C$, known as the Berezinskii-Kosterlitz-Thouless transition [124]. Between T_C and T_{BKT} bound VAPs and unbound vortices coexist, while below T_{BKT} all vortices are bound to VAPs. Although NSSPDs are usually operated below T_{BKT}, the bias current reduces the binding energy of the VAPs and thermal activation may lead to unbinding of a VAP. The unbound parts move in opposite directions towards the strip edges causing a voltage pulse.

Yet, there is no coherent theory for modelling the dependence of the dark counts of a NSSPD on the applied bias current I or on the operating temperature T. A phenomenological approach can be found in [125]. Based on the experimental data Kitaygorski et al. describe the dark count dependency on the bias current by an exponential:

$$\Gamma_{dk}(I) \propto \Gamma_0 \exp\left(\frac{I}{I_C}\right). \tag{4.12}$$

4.3 Detector Setup

In this section our NSSPD system is presented which was set up in cooperation with the Delft University of Technology. A sketch is shown in figure 4.3. It consists of three parts, the detector chip itself which is submerged in liquid helium, the readout electronics, and the optical coupling to the detector. Due to its fix fibre coupling the detector can be easily implemented in different optical experiments. In the following the different parts of the detector system are depicted, and the fabrication of the detector chip and the fibre coupling procedure will be described.

4.3.1 Detector Chip

The heart of the detector system is a meandering superconducting nanowire. It is biased close to its critical current so that a breakdown of the superconducting state can be observed when a photon is absorbed in the wire, as explained in section 4.2.2. The wire is fabricated on a sapphire substrate and connected to two gold contacts. This part of the detector system will in the following be denoted "detector chip".
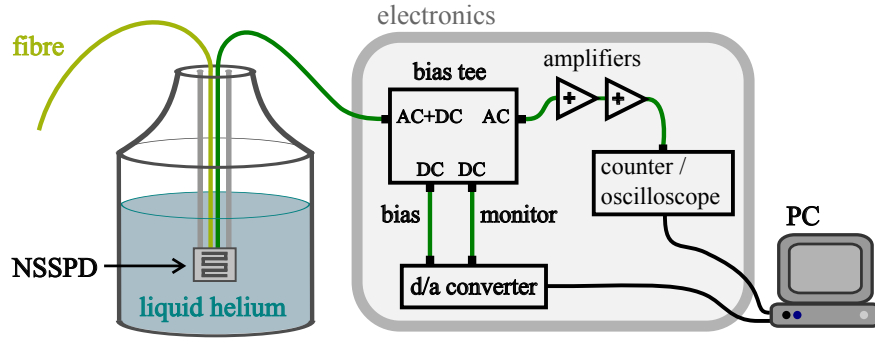
Figure 4.3: Sketch of the NSSPD system: The detector chip is mounted on a dip-stick and submerged in liquid helium. Light can be coupled to the detector through an optical fibre. Electrically the detector is connected to a bias tee. The short pulses from the detector indicating photon absorption are amplified after the ac port and coupled to a counter or an oscilloscope. The dc port of the bias tee is used to provide the bias current for the detector. At an additional dc port the bias voltage dropping at the detector is monitored to make sure the detector does not stay in the normal-conducting state.
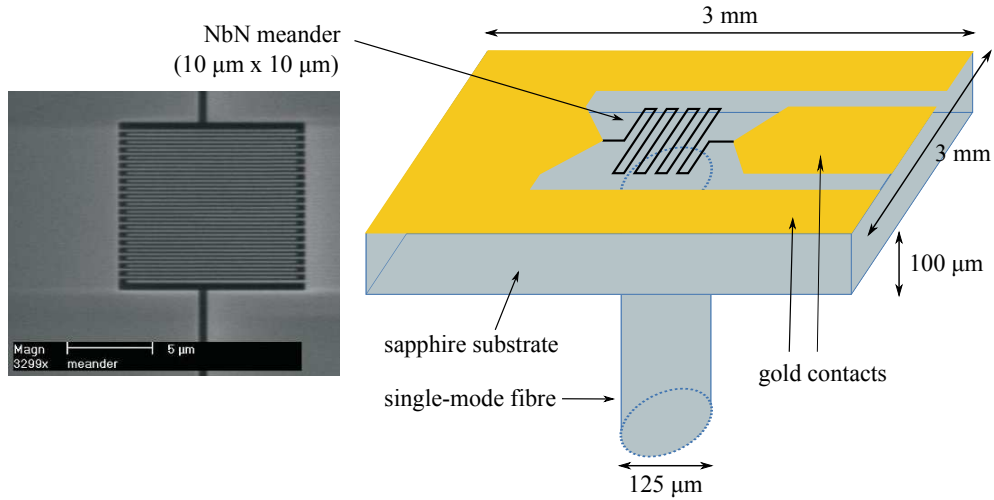
Figure 4.4: Scheme of the detector chip. The NbN meandering wire is the active area of the detector. A scanning tunnelling microscope picture of this part is shown on the left. It is fabricated on a sapphire substrate and electrically connected to two gold contacts. A single-mode optical fibre is glued to the back side of the sapphire, opposite to the active area.
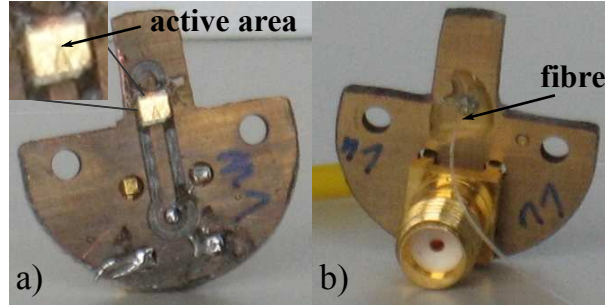
Figure 4.5: Photograph of the printed circuit board. (a) Front side of the board. The detector is glued on a printed circuit board and the gold contacts are bonded to the board (the bonds are to thin to be seen here). Inset: Magnification of the detector chip. Mainly the gold contacts can be seen. The active area (meandering wire) sits between the contacts. (b) Back side of the board. The detector chip is placed over a hole in the board. An optical fibre is fed through the hole and glued on the back side of the detector chip.

Layout

Figure 4.4 depicts a scheme of the detector chip. A photograph of the detector chip glued on a printed circuit board is shown in figure 4.5. The detector's active area consists of a meandering NbN wire with a size of 10 µm × 10 µm. The wire is 5 nm thick and 100 nm wide. The gaps between wires are also 100 nm thick which results in a filling factor of 50% for the active area. The meander structure is fabricated on a sapphire substrate and the wire ends are connected to two gold contacts. The dimensions of the chip are 3 mm × 3 mm × 100 µm. For optical access to the detector area, a single-mode optical fibre is glued to the back of the sapphire substrate opposite to the active area. For a description of the fibre-coupling procedure see section 4.3.3.

Fabrication

All detector structures used for this work were fabricated at Delft University of Technology by Sander N. Dorenbos and Valery Zwiller. A detailed description of the fabrication procedure can be found in [118].

At first, a NbN film of a thickness of 5 nm is grown epitaxially on the sapphire substrate [126]. Meander structure and gold contacts are fabricated using electron beam lithography. The lithographic procedure consists of two steps. In the first step, the gold contacts are defined. The structures are written on a polymethyl methacrylate (PMMA) resist spinned on the substrate previously. PMMA is a positive resist, i.e. during development it is removed from the areas that were exposed to the electron beam. After developing the resist, gold is deposited on the sample surface. When the resist is solved, gold laying on the resist comes off but it stays at the areas exposed to the electron beam before.
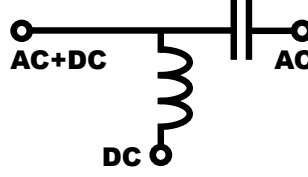
Figure 4.6: Scheme of a bias-tee. Low frequency signals pass the device at the dc port, high frequency signals at the ac port.
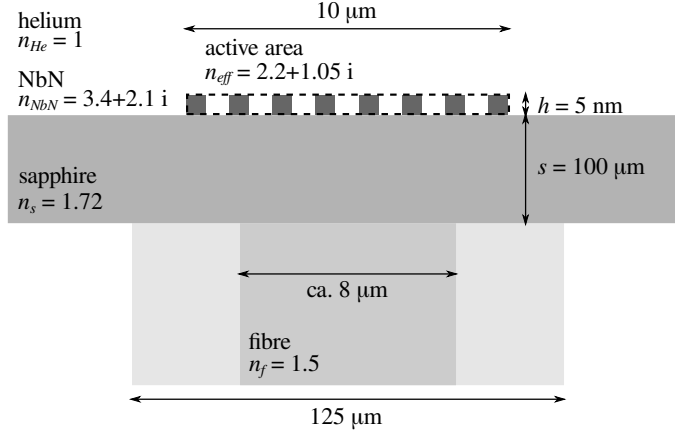
The meander is written in a second step using hydrogen silsequioxane (HSQ) as a negative resist. After developing the resists, the HSQ stays at the parts previously exposed to the electron beam and forms a mask for the meander structure. Also the gold contacts were covered with HSQ. All the parts not covered were removed using reactive ion etching. Finally the HSQ resist is removed by dipping the sample in buffered hydrofluoric acid.

4.3.2 Electronics

As described in section 4.2.2, the detection of light with a NSSPD is based on the detection of the voltage pulses. For electrical connection, the detector chip is glued on a printed circuit board and the gold contacts on the chip are bonded to the board (see figure 4.5). A coaxial cable is connected to the back side of the board. The board is mounted on a dip stick in order to place the detector in a helium dewar. The cable is fed to the outside of the dewar, all other electric components are operated at room temperature.

The voltage drop along the wire is zero as long as it is superconducting. When a normal conducting state occurs across the wire, a voltage pulse can be detected. Since its amplitude is on the order of some nanovolts, the pulse needs to be amplified for further processing. The voltage length is in the nanosecond range, so two amplifiers of 2 GHz bandwidth (miteq) are used. They amplify by 36 dB each, resulting in an overall amplification of 72 dB.

The black part of figure 4.3 depicts the electronics. The element next to the detector is a bias-tee which is a passive element that separates high and low frequency parts of an electrical signal, as shown in principle in figure 4.6. The AC+DC port of the bias tee is connected to the detector. The bias current is provided through the DC port and the high frequency voltage pulses are output at the AC port. There is an additional DC at our device which is used to monitor the d.c. voltage over the wire. It equals zero unless the detector switches permanently to the normal conducting state (e.g. because its critical temperature is exceeded). The voltage pulses from the detector are amplified at the bias tee's AC port for further analysis, which is done either by a pulse counter or an oscilloscope.

helium
$n_{He} = 1$

NbN
$n_{NbN} = 3.4+2.1\,i$

active area
$n_{eff} = 2.2+1.05\,i$

10 µm

$h = 5$ nm

sapphire
$n_s = 1.72$

$s = 100$ µm

ca. 8 µm

fibre
$n_f = 1.5$

125 µm

Figure 4.7: Cross section of the fibre coupled detector chip. Light is coupled in through an optical fibre. It passes the fibre-sapphire and the sapphire-NbN interface before it can be absorbed in the meandering wire.

4.3.3 Fibre Coupling

For a detector with an active area as small as 10 µm × 10 µm, it is not trivial to couple light to it efficiently. For different reasons optical coupling by an optical single-mode fibre has many advantages over free space light coupling. In a fibre-coupled configuration it is easier to keep the detector at 4.2 K by submerging it in a helium dewar. Since all surrounding parts including the fibre and the electrical connections are on liquid helium temperature, counts due to thermal photons are negligible. A fix fibre coupling to the detector is also very convenient for implementing the detector quickly in different experimental setups.

As sketched in figure 4.4 we glued the fibre on the back side of the sapphire substrate, opposite to the detector's active area.

Geometry and Theoretical Coupling Factor

Figure 4.7 shows a cross section of the fibre-coupled detector chip. The single-mode optical fibre is glued directly to the polished sapphire substrate of the chip using a commercial epoxy glue. Light from the fibre crosses 100 µm of sapphire and two interfaces (glass-sapphire and sapphire-detector) before it can be absorbed at the active area. There are three main reasons for losses (i.e. photons that are not absorbed at the active area) in this configuration. Firstly, the light beam widens while travelling through the sapphire to a diameter larger than the active area. Secondly, at both interfaces photons are reflected back, and last but not least, the absorption in the detector is limited by its small height h of only 5 nm.

For the first effect, the numerical aperture (NA) of the fibre and the mode field diameter d_f at the fibre facet, given by the manufacturer as NA = 0.13 and $d_f =$

5 nm, together with the sapphire substrate thickness $s = 100\,\mu$m and refractive index $n_s = 1.72$ have to be used to calculate the percentage of the light intensity that hits the detector's active area of $10\,\mu$m $\times$ $10\,\mu$m. Here, the diameter of the beam is defined as the difference between the points where the field amplitude has decayed to a fraction of e^{-2} of its maximal value. Applying all the values given above, the diameter of the beam at the active area is $d_b = 20\,\mu$m. Assuming a Gaussian distribution for the field amplitude and perfect alignment, this leads to a percentage of $p_w = 70\%$ of the light coupled into the sapphire substrate to arrive at the detector's active area.

Reflection losses can be calculated using Fresnel's equations. For incidence of light perpendicular to an interface of two media with (complex) refractive indices n_1, n_2, the fraction of intensity reflected or transmitted at the interface, R and T, respectively, is given by

$$R = \left| \frac{n_1 - n_2}{n_1 + n_2} \right|^2 \tag{4.13}$$

$$T = \left| \frac{2n_1}{n_1 + n_2} \right|^2 \cdot \mathrm{Re}\left(\frac{n_2}{n_1} \right) \tag{4.14}$$

Using equation 4.14 with the refractive indices $n_f = 1.5$ for the fibre and $n_s = 1.72$ for sapphire, the transmission $T_{\text{f-s}}$ at the fibre-sapphire interface can be calculated to $T_{\text{f-s}} = 99.5\%$. The maximum efficiency η_f of our fibre coupling is hence

$$\eta_f = p_w \cdot T_{\text{f-s}} = 70\% \tag{4.15}$$

For calculating the absorption at the active area, a detailed calculation of transmission and reflection of an absorbing film can be found in [127]. Taking into account the refractive index for niobium nitride $n_{\text{NbN}} = 3.4 + 2.1\,\mathrm{i}$, the refractive index for helium $n_{\text{He}} = 1$, and the filling factor of 50%, the effective refractive index of the active are is assumed to be $n_{\text{eff}} = \frac{1}{2}(n_{\text{NbN}} + n_{\text{He}}) = 2.2 + 1.05\,\mathrm{i}$. Applying this value to the calculations in [127], the reflection and transmission for our meandering detector equal $R_m = 9.9\%$ and $T_m = 51.5\%$, respectively. The percentage of the incident photons absorbed at the detector's active area, i.e. the efficiency η_m of the meander structure is then given by

$$\eta_m = 1 - R_m - T_m = 38.6\%. \tag{4.16}$$

Whilst for the fibre coupling efficiency η_f possible improvements are straightforward (e.g. by further thinning the sapphire substrate), η_m is mainly determined by the small detector height and its material, its limitations are therefore more fundamental. Improvements can be made by making the photons pass the detector more often, as by inserting it into a cavity structure [128], which, however, reduces the detector's spectral range dramatically.

Taking the geometry of the fibre coupling and the meander structure with the respective reflective indices into account and assuming that every photon absorbed triggers
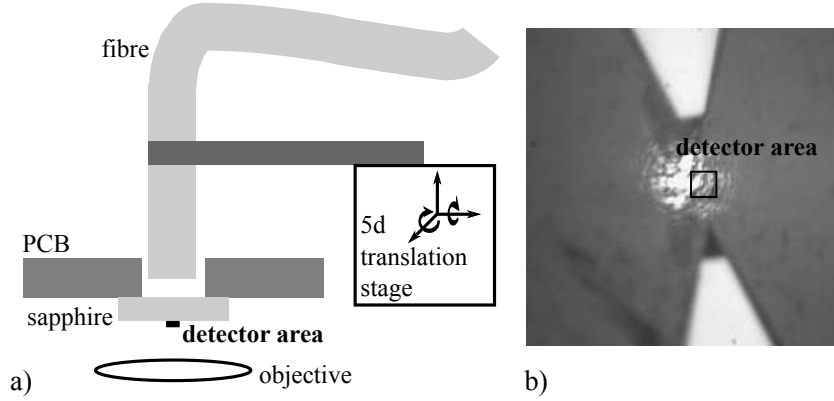
Figure 4.8: (a) Set-up for the fibre coupling. The detector chip is mounted on an inverted microscope. Light is coupled into the fibre which is aligned opposite the detector's active area using a 5d-translation stage. (b) Picture taken through the microscope. The active area can be seen on the right of the light spot at the fibre's end facet. The bright triangles are the gold contacts.

the detector, the theoretical maximum device efficiency η_d can thus be calculated as

$$\eta_d = \eta_f \cdot \eta_m = 27\%. \tag{4.17}$$

Coupling Procedure

Originally the detector chip is fabricated on a 400 μm thick sapphire substrate. If one glued a fibre directly on its backside, arriving on the front side the light beam would have widened to a spot size of 66 μm which is large compared to the detector area of 10 μm × 10 μm. Therefore, in a first step it was thinned to a thickness of 100 μm and polished. A coupling stage was built on an inverted microscope (Olympus). It consists of a fibre holder mounted on a 5d-translation stage as shown in figure 4.8a. The detector chip was glued to the printed circuit board (see section 4.3.2) before the fibre coupling. For the alignment of the fibre core opposite to the detector area, visible light was coupled into the fibre. In figure 4.8b a photo of the detector chip taken from the front side is shown. The bright triangles are parts of the gold contacts with the detector's active area between their apexes. The bright spot on the left of the active area is light coming from the facet of the optical fibre being held on the backside of the detector chip. For fibre coupling, the end facet of the fibre is aligned to the active area and glued to the substrate's backside. Figure 4.5 shows a photograph of the fibre-coupled detector.
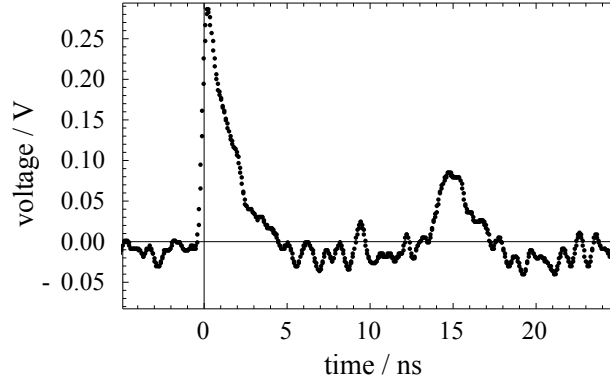
Figure 4.9: Typical voltage trace after photon absorption taken with an oscilloscope of 1 GHz bandwidth.

## 4.4 Detector Characteristics

In section 4.1.1 the main characteristics of a single-photon detector have been summed up. In this section these features will be discussed in terms of our detector system.

4.4.1 Timing Properties

The NSSPD's response to a photon absorbed at its active area is a voltage pulse. Figure 4.9 shows such a pulse after amplification recorded with an oscilloscope of 1 GHz bandwidth. Characteristic is a steep slope of a few 100 ps until the signal reaches its maximum. This rise time of the pulse is given by the time scale of the processes creating a hot-spot in the superconducting wire (see section 4.2.2). This is followed by a comparatively long decay. The pulse height of 300 mV corresponds to a height of 7.5 nV before amplification. The second pulse after 14.5 ns is a reflection due to impedance mismatch.

Dead Time

The detector's dead time is given by the length of the voltage pulse after photon absorption. When superconductivity is re-established, the detector is operable again. In figure 4.9 a the voltage drops to zero again after 4 ns. A dead time of only a few nanoseconds is short compared to dead times of most other single-photon detectors (cf. section 4.1.1). The short detector's dead time not only enables us to measure high count rates of 250 MHz, it also allows for resolving comparatively small photon arrival time differences, which was a key element for the experiment presented in chapter 5.
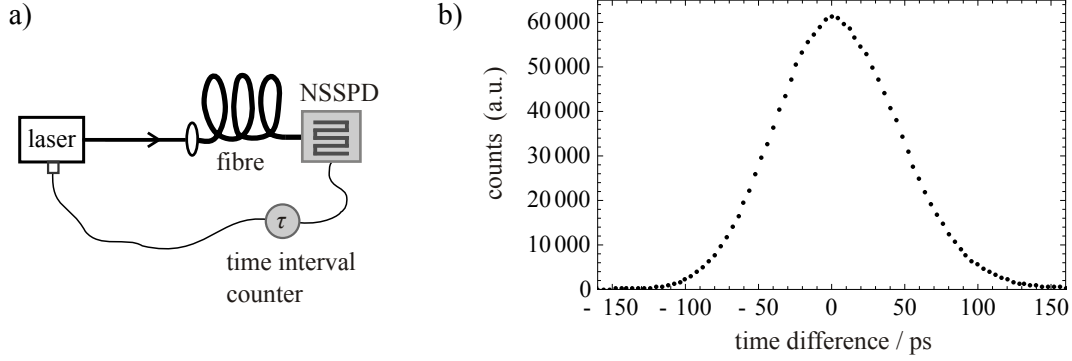
Figure 4.10: (a) Set-up for the jitter measurement. (b) Temporal jitter of the detector measured applying femtosecond optical pulses.

Temporal Jitter

The temporal jitter of a detector determines its temporal resolution. Here, the jitter has been measured using femtosecond optical pulses and a commercial time interval counter (TIC). A scheme of the setup is shown in figure 4.10a. A pulsed Titanium-Sapphire Laser (Coherent) was used to provide femtosecond pulses, which were attenuated and sent to the NSSPD. The voltage pulses from the detector and the synchronisation pulse from the laser were fed to the TIC of 4 ps resolution (PicoQuant). Figure 4.10b shows the outcome of the correlation measurement. From the width of the peak the temporal resolution of our detector system can be determined to 100 ps. It is not clear whether the limiting factor here is the detector structure itself or the read-out electronics. The jitter of the laser's synchronisation pulses does not have to be taken into account because an auto-correlation measurement on these pulses with the TIC showed a temporal jitter of less than 50 ps.

4.4.2 Sensitivity

Dark counts and quantum efficiency determine the detector's noise equivalent power NEP at wavelength λ, defined by

$$\text{NEP} = \frac{hc}{\lambda} \frac{\sqrt{R}}{\eta} \tag{4.18}$$

where R is the dark count rate and η the detector's quantum efficiency. The NEP is a measure for the sensitivity of a detector.
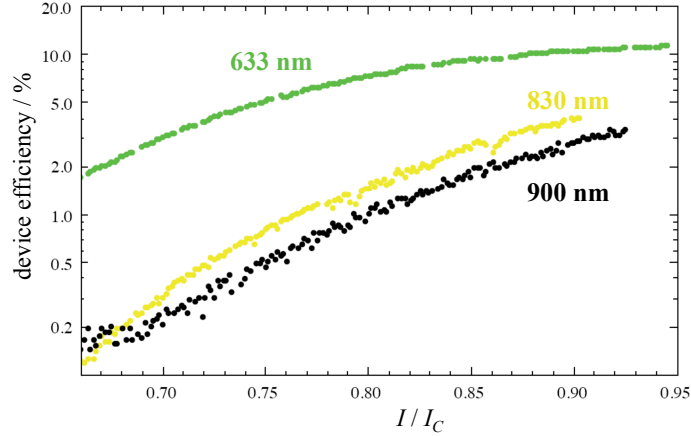
Figure 4.11: Device efficiency against the reduced bias current for three different wavelengths (633 nm, 830 nm, and 900 nm). The efficiency increases with increasing photon energy. For photons of 633 nm wavelength the efficiency saturates at 90% of the critical current.

Device Efficiency

The device efficiency is the fraction of photons detected by the device relative to all photons coupled to the detector. When measuring the efficiency the crucial point is how to determine the amount of incoming photons. Here, this was done using detectors of known quantum efficiency, a commercial Si-APD (Perkin Elmer) or a commercial Si-Photodiode (Spectrum Detector). The later is only able to detect photon powers of at least 2 nW, therefore in this case the intensity of the light source was measured with the photodiode and then attenuated by a known amount before sending the light to the NSSPD. For that, neutral density filters were placed in the light beam before coupling to the optical fibre. Since the exact attenuation is strongly dependent on the exact position of the filter in the light beam, this was a major source of errors.

Figure 4.11 shows the device efficiency of a typical detector against the reduced bias current, measured for three different wavelengths (633 nm, 830 nm, and 900 nm). For the ideal NSSPD, there would be a threshold bias current for every photon wavelength: for currents larger than that, the absorption of a photon would always cause a detector click, for currents smaller than the threshold the current density flowing around the hot-spot would not be enough to trigger the detector (cf. section 4.2.2). The measurements do not show that strict a threshold behaviour. For light at 633 nm the device efficiency saturates beginning at around $0.88\,I_C$. At this point the bias current is big enough that every absorbed photon causes a breakdown of the superconducting state. For smaller bias currents not all absorbed photons trigger the detector, but some of them do. The probability for this to happen depends e.g. on the position of photon absorption. Another reason for the smooth slope is, that at currents smaller than the threshold current, the absorption of a photon increases the probability for a dark count induced

	calculated (section 4.3.3)	actual values
fibre coupling	$\eta_f = 70\%$	$\tilde{\eta}_f > 26\%$
absorption at meander	$\eta_m = 38.6\%$	$\tilde{\eta}_m \approx \eta_m = 38.6\%$
meander efficiency	$\eta_y = 1$ (perfect meander)	$\tilde{\eta}_y < 1$
device efficiency	$\eta_d = 27\%$	$\tilde{\eta}_d = 10\%$

Table 4.1: Calculated and actual efficiencies. Different factors have to be taken into account, the fibre coupling, the percentage of photons absorbed at the meander, and the efficiency of the meander, i.e. the percentage of absorbed photons that actually trigger the detector (see text).

by fluctuations. For the other two wavelengths (830 nm, 900 nm) no such saturation is observed. Probably, the photon energy here is not large enough for every absorbed photon to trigger the detector.

In section 4.3.3 the maximum device efficiency η_d for our detector system was calculated (equation 4.17). The maximum device efficiency η_d is composed of two components, the absorption of the NbN meander structure η_m and the maximum efficiency of the fibre coupling to the active area η_f. The results of section 4.3.3 are recalled in table 4.1. The experimental device efficiency $\tilde{\eta}_d$ is mainly given by three components

$$\tilde{\eta}_d = \tilde{\eta}_f \cdot \eta_m \cdot \tilde{\eta}_y. \tag{4.19}$$

Here, $\tilde{\eta}_f$ is the experimental fibre-coupling efficiency and η_m the absorption of the meander (see section 4.3.3). $\tilde{\eta}_y$ is the percentage of photons absorbed at the meander that trigger a detector pulse. In equation 4.17, for the perfect meander $\eta_y = 1$ was assumed. However, the uniformity of the meandering wire is crucial for an optimum yield η_y: if the wire diameter varies along the meander, the smallest diameter determines the critical current. That means that when applying a bias of e.g. $I = 0.9\,I_C$, for all the parts where the wire diameter is larger, the actual bias current is less than 90% of the critical current, which results in a lower efficiency there [129], so experimentally $\tilde{\eta}_y < 1$ is probable. The highest efficiencies $\tilde{\eta}_d$ obtained with our devices experimentally are around 10%. From this using equations 4.16 and 4.19 with $\tilde{\eta}_y < 1$, a lower bound for our fibre-coupling efficiency $\tilde{\eta}_f$ can be calculated as $\tilde{\eta}_f > 26\%$. This is similar to the highest coupling factor of 33% reported for a comparable fibre-coupling approach [117]. All the values for the different efficiencies are summed up in table 4.1.

Dark Counts

In figure 4.12 dark counts of a typical detector are shown against the reduced bias current I/I_C. Up to 90% of the critical current there are typically less than 10 dark counts per second. With higher bias currents the dark counts increase exponentially (cf. section 4.2.2). At a current of 93% of the critical current, the value the NSSPD
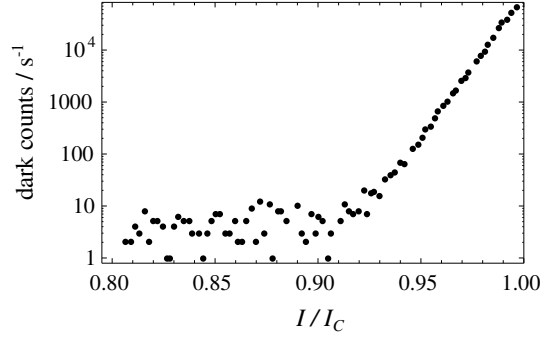
Figure 4.12: Dark counts of a NSSPD against the reduced bias current. At currents larger than 90% of I_C an exponential increase of dark counts is observed.

was usually operated at $50 \, \text{s}^{-1}$ are measured. The choice of the current applied for a measurement is a trade-off between device efficiency and dark counts of the detector. Both increase with increasing bias current. At best the device efficiency saturates before the exponential increase starts. Then the value for I should be chosen within this current interval.

4.4.3 Photon Number Resolution

Theoretically NSSPDs can provide photon number resolution, because the response of the detector depends on the energy deposited in the superconducting wire. However, the variations are small and experimentally very difficult to observe.

One approach to obtain information about the photon energy is to exploit the fact, that the shape of the voltage pulse depends on the energy absorbed [115, 130]. Experimentally, it has been shown that for the voltage pulse amplitude distribution both mean and amplitude depend on the photon energy [131, 132]. For wavelengths larger than the hot-spot regime cut-off, where the detection mechanism changes from the hot-spot type to the unbinding of vortex-antivortex pairs (cf. section 4.2.2), this dependency can be used experimentally [130]. Using this approach, an energy resolution of 0.6 eV has been reported for near-infrared wavelengths [132].

Another way to obtain energy resolution is to measure at different bias currents. In a very simple model, the detector could only be triggered when the photon energy deposited in the wire creates a hot spot large enough to exceed the critical current density in its sidewalks (cf. figure 4.2). In this simple model, there are bias current intervals where the device is sensitive to more than 0, more than 1, more than 2 etc. photon at the time, which could be used to obtain information about the photon number. However, the dependency of the device efficiency on the bias current (and thus also its dependency on the photon number) is not that simple (cf. section 4.4.2). Nevertheless, there are ideas to use the dependence of the device efficiency on the bias current to obtain energy resolution, as the one presented in [133]. Here the efficiency is

measured while the bias current is swept. The current at which the quantum efficiency starts to saturate (cf. section 4.4.2) is a measure for the size of the hotspot, from which the absorbed energy can be calculated. It is, however very difficult to determine this point experimentally.

Nowadays, the more practicable way to obtain information about the photon mumber is to utilise detector arrays consisting of several parallel meanders [111, 120, 121]. They produce an electrical output propotional to the number of meanders triggered by the light field.

# 5 Measuring the Quantum Nature of Light with a Single Detector

In chapter 2 it was discussed how to formulate a quantum theory of light. The first hint for the quantisation was Einstein's explanation of the photoelectric effect (section 2.1.1). Later, experimental observations were made for the light emitted by quantum sources, a classical theory fails to describe. In this context, the second-order auto-correlation function of the electric field $g^{(2)}$ was discussed in section 2.2.2. A $g^{(2)}$-function exhibiting values smaller than 1 cannot be derived employing a classical theory.

In this chapter the experimental aspects of how to measure second-order correlation functions of the electric field are discussed. The observation of non-classical $g^{(2)}$-functions enforces a quantum theory of light. To eliminate other sources for the quantum effects measured, it is of interest to perform an experiment as fundamental as possible. Certainly the most fundamental setup has to contain a source emitting non-classical states of light and a single-photon detector. An experiment built up with only these two components is presented in this chapter. However, since this is not the standard design for measuring $g^{(2)}$-functions, in the first section of this chapter the most commonly established method to measure second-order correlation functions is discussed.

5.1 Intensity Correlation Measurements with Two Detectors

The first experiment to measure light intensity correlations was carried out by R. Hanbury Brown and R. Q. Twiss in 1954 [134]. Their experimental setup is in principle utilised until today for various purposes, and in their honour it is called Hanbury-Brown-Twiss (HBT)-setup. Although it was originally developed for an astrophysical experiment [134], soon its applicability in other areas was recognised [135].

Nowadays second-order correlation measurements are performed for many goals. Here, we are interested in the demonstration of quantum-light emission. But there is a bunch of other applications, some of which will be given shortly at the end of this section.
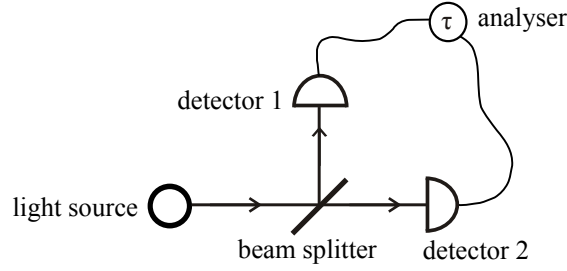
Figure 5.1: Scheme of the HBT setup. L ight is sent to a (50:50) beam splitter. In each of its outputs a detector is placed, and time differences between detector clicks (or instants of time of the clicks) are recorded.

5.1.1 Second-order Correlation Functions from a Hanbury Brown and Twiss-type Measurement

Figure 5.1 shows a scheme of the typical HBT-setup. Light from the source is sent to a (50:50) beam splitter. In each output of the beam splitter a detector is placed. The time differences between photon arrivals are measured in either of two ways:

Start-Stop Method

Using the first method, a click in detector 1 starts a clock which is stopped by the next click in detector 2. The measured time difference τ between start and stop photon is saved. Thus a distribution of start-stop time differences can be obtained, which is related to the $g^{(2)}$-function.

An evaluation of this relation is given in [136]. Assuming that the probability to detect a photon from the source is η and the background rate, i.e. detection events due to stray light or detector dark counts, is b, the probability density $p(\tau)$ to measure a stop event at time τ after a start event has occurred at time $\tau = 0$ is given by

$$p(\tau) = (\eta g^{(2)}(\tau) + b) \cdot \left(1 - \int_0^\tau p(t)\mathrm{d}t \right) \tag{5.1}$$

where the first factor is the probability that a stop event is measured at time τ, and the second factor the probability that no stop event has been detected before. Substituting $P(\tau) = \int_0^\tau p(t)\mathrm{d}t$, $P(\tau)$ satisfies the differential equation

$$\frac{\mathrm{d}}{\mathrm{d}\tau} P(\tau) = (\eta g^{(2)}(\tau) + b)(1 - P(\tau)) \tag{5.2}$$

which is solved by

$$P(\tau) = 1 - C \cdot \exp\left(-\int_0^\tau (\eta g^{(2)}(t) + b)\mathrm{d}t \right). \tag{5.3}$$

With the condition $P(0) = 0$ (no stop event has occurred at $\tau = 0$) the integration constant C can be calculated to $C = 1$. Hence the probability density $p(\tau) = \frac{\mathrm{d}P(\tau)}{\mathrm{d}\tau}$ equals

$$p(\tau) = (\eta g^{(2)}(\tau) + b) \cdot \exp\left(-\int_0^\tau (\eta g^{(2)}(t) + b)\mathrm{d}t \right). \tag{5.4}$$

Since $\lim_{\tau \to \infty} g^{(2)}(\tau) = 1$, for large time differences $p(\tau)$ decays exponentially, whereas for short time differences τ it approaches $p(\tau) \approx \eta g^{(2)}(\tau) + b$.

The start-stop method is relatively easy to realise electronically using a time-to-amplitude converter, and has the advantage, that the histogram of time differences can be evaluated during the measurement. A disadvantage of this method might be, that the $g^{(2)}$-function is not measured directly. But for low photon count rates, the measured distribution of start-stop time differences approximates $g^{(2)}(\tau)$ (or more precisely $\eta g^{(2)}(\tau) + b$) very well, since in this case the integral in equation 5.1 approximates zero.

Time-Tag Method

Using the time-tag method, arrival times are saved using the internal clock of the analyser. Typically these data are saved in a buffer and are then written to the hard drive. This enables the device to record photon bursts of size of the buffer with the writing time to the hard drive not being the limiting factor. Later a distribution of time differences can be calculated from the data obtained from all photon pairs.

The advantage of this method is, that the $g^{(2)}$-function, or to be more precise the distribution $d(\tau) = \eta g^{(2)}(\tau) + b$, is thus measured directly. A disadvantage can be that big amounts of data accumulate which have to be evaluated later. Furthermore, the data can not be evaluated during the measurement, i.e. the experiment can be assessed only after data acquisition is finished.

5.1.2 Applications of Intensity Correlation Measurements

As pointed out above, the measurement of second-order correlations of the electric field can be used to prove very fundamental (quantum) effects, such as antibunching behaviour of non-classical sources. For this temporal auto-correlation functions are determined, usually applying the standard HBT setup (figure 5.1). Other essential statistical effects, such as photon bunching in light from a thermal source or the characteristic changes of the $g^{(2)}$-function at the laser threshold, can be measured as well.
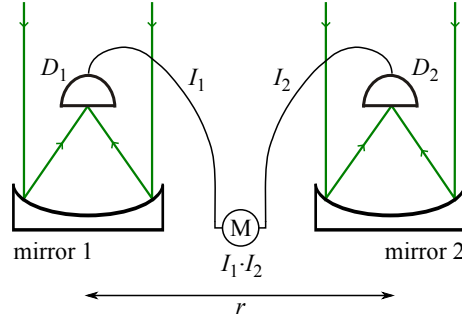
Figure 5.2: Scheme of the original HBT experiment. Light from a star is sent to two mirrors at distance r and detected at detectors D_1 and D_2. The photocurrents I_1 and I_2 are fed to the multiplier M. The product is proportional to the intensity correlations of the electric field at the positions of D_1, D_2.
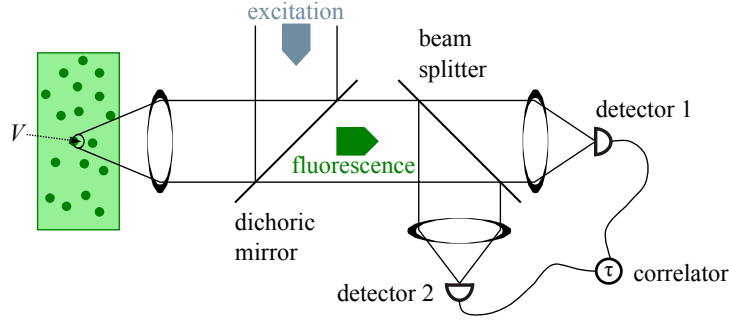
Figure 5.3: Scheme of a FCS setup. Fluorescence from a volume V in the sample is collected. From the intensity correlations parameters that determine the particle dynamics can be obtained.

Beyond fundamental considerations, measuring intensity correlations can provide useful information, also for classical light sources. In the original work by Hanbury Brown and Twiss it was shown how the angular radius of a star can be determined measuring intensity correlations [134]. Here, spatial rather than temporal intensity correlations are observed, but the principle is the same as for temporal autocorrelation measurements. Intensities of the light of the same star are measured at two different positions. By varying the distance r between the positions of two detectors $D1$, $D2$ spatial intensity correlations of the light source can be measured. From this informations the size of the light source (the star) can be obtained (figure 5.2).

Furthermore, intensity correlation measurements are used to study particle dynamics. In fluorescence correlation spectroscopy (FCS) a sample containing fluorescing particles is investigated. In a typical FCS setup, the fluorescence from a small volume V inside the sample is sent to an apparatus to analyse the temporal $g^{(2)}$-function, e.g.

a standard HBT setup (figure 5.3). The measured intensity correlations depend on the particle dynamics inside the sample. Such diffusion coefficients, average concentrations, chemical reaction rates, molecular rotational Brownian motion, singlet-triplet dynamics, and spectral dynamics can be observed [137].

## 5.2 Measurement of Photon Statistics with a Single Detector

The HBT setup is applied in so many experimental setups nowadays that it is often automatically thought of when it comes to the matter of measuring photon statistics. For demonstrating single-photon emission, sometimes one can hear interpretations of the HBT experiment in which the beam splitter plays a major role, such as that due to the quantum nature of light photons cannot be "divided" at the beam splitter which explains the antibunching feature. Of course, the *only* reason for employing a beam splitter and two detectors is that usually the correlation times to be measured are shorter than the detector's dead time. To circumvent this problem, two detectors are utilised. However, the most fundamental experiment to demonstrate emission of non-classical light just consists of a quantum-light source and a single-photon detector (figure 5.4). In this section an experiment built with only these two components is presented.
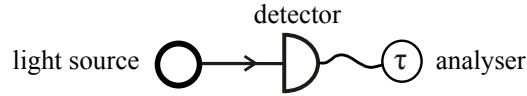

Figure 5.4: The most fundamental experiment to demonstrate the quantum nature of light consists of a quantum light source and one single-photon detector.

5.2.1 Experimental Setup

The key elements for resolving antibunching with a single detector are first a very fast single-photon detector and second a comparatively slow quantum emitter. For detection we utilise a nanowire superconducting single-photon detector (NSSPD). A detailed description of the device was given in chapter 4. The important feature here is the short dead time of around 4 ns. Commercial single-photon detectors, as avalanche photodiodes (APDs) typically possess dead times which are at least one order of magnitude larger (cf. section 4.1.2). As single-photon source we make use of a single nitrogen-vacancy (N-V) colour centre in diamond. This type of non-classical light source has been discussed in more detail in section 3.3. Here the important characteristic is the long lifetime of 30 ns - 50 ns, which these defect centres can possess when implemented in a nano-crystal.
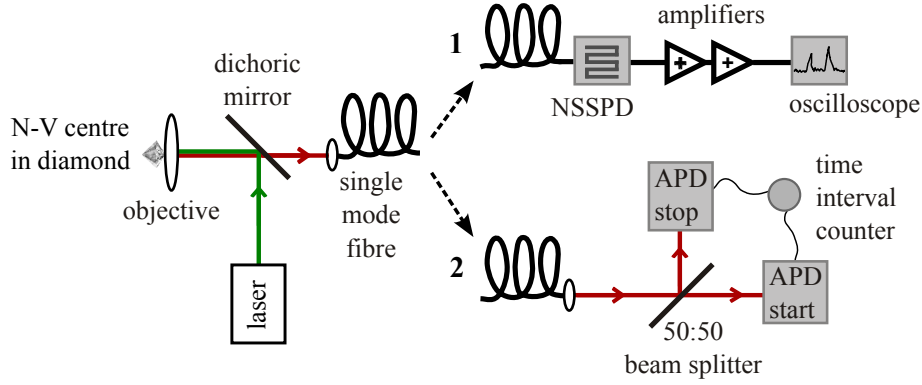
Figure 5.5: Experimental setup: A single N-V centre in a diamond nano-crystal is excited with a 532 nm cw laser. Its emission is collected via a confocal optical microscope, coupled to a single mode optical fibre, and detected in two configurations: 1. a single fibre-coupled NSSPD and 2. a standard free beam Hanbury-Brown-Twiss (HBT) setup containing a beam splitter and two avalanche photodiodes (APDs). Correlations are analysed by a fast 1 GHz oscilloscope or by a time interval counter.
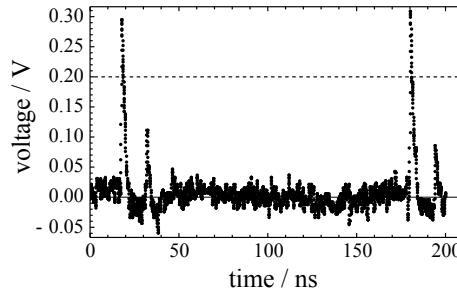
Figure 5.6: Typical voltage trace with two detection events recorded with the oscilloscope. Only double events with a time difference of between 5 ns and 200 ns were collected. With the trigger level at 0.2 V (dashed line) the spurious reflections (see section 4.4.1) were not detected.

The experimental setup is depicted in figure 5.5. A single N-V centre was located using an inverted microscope as described in [92]. It is pumped optically using a continuous-wave laser at 532 nm. The fluorescence from the N-V centre is coupled into a single mode optical fibre and sent directly to the NSSPD (figure 5.5, configuration 1). For comparison the light from the same source can also be coupled into a conventional free-space HBT setup (figure 5.5, configuration 2) with two commercial APDs (Perkin Elmer).

The information about photon arrival time differences is obtained using a oscilloscope of 1 GHz bandwidth (Tektronics) for the read-out of the NSSPD voltage pulses. The oscilloscope was programmed to save a pulse trace whenever a threshold of 200 mV is

exceeded a second time within a time window of 5 ns - 200 ns after a first event. A typical trace is shown in figure 5.6. Afterwards the saved traces are analysed using a Sage script and time differences between to subsequent events are extracted to obtain a histogram.

5.2.2 Experimental Results

Before employing the quantum emitter we performed two test experiments with classical light. Light from an attenuated laser was coupled into only one of the APDs (inset of figure 5.7 a). The voltage output from the detector was fed into the oscilloscope and read out as described in the previous section. The measured $g^{(2)}$-function (figure 5.7 a) shows an absence of coincidence counts at time intervals shorter than 30 ns. This is due to the dead time of the APD preventing detection of coincidence events within a 30 ns time interval. For correlation times between 30 ns and 50 ns a bunching feature is observed due to the APD's afterpulsing. Afterpulsing is induced by carriers trapped in the APD for longer times than the dead time. They can cause a second detector click shortly after the detector is operable again after a photon has been detected. The afterpulsing probability according to the manufacturer is 0.5% . Here this is relevant since at our photon count rates of around 300,000 s^{-1} the probability for a second photon to arrive within a time window between 30 ns and 200 ns after a first one is 5%, i.e. one out of eleven events when a second pulse is detected is due to afterpulsing. These events account for the bunching observed in figure 5.7a. In a second test we coupled attenuated laser light into the NSSPD (inset of figure 5.7b) and again measured the $g^{(2)}$-function. The result is shown in figure 5.7b. Obviously, there are no correlations between incoming photons and, more important, no suppression of coincidence events in the time window of interest. Furthermore, no afterpulsing is observed.

Figure 5.8 shows the results of the $g^{(2)}$-function measurement for the N-V centre emission. The measurement was done in both configurations of the setup depicted in figure 5.5. Blue dots correspond to the $g^{(2)}$-function measured with the single NSSPD. It has a pronounced antibunching dip which fits well to a three-level rate equation model (solid black line, see section 3.3.2). Red dots correspond to the standard HBT measurement employing two APDs. Obviously, both measurements reveal the quantum nature of the photon stream in the same manner proving that a statistical analysis of a stream of single photons can very well be performed with a single detector only.
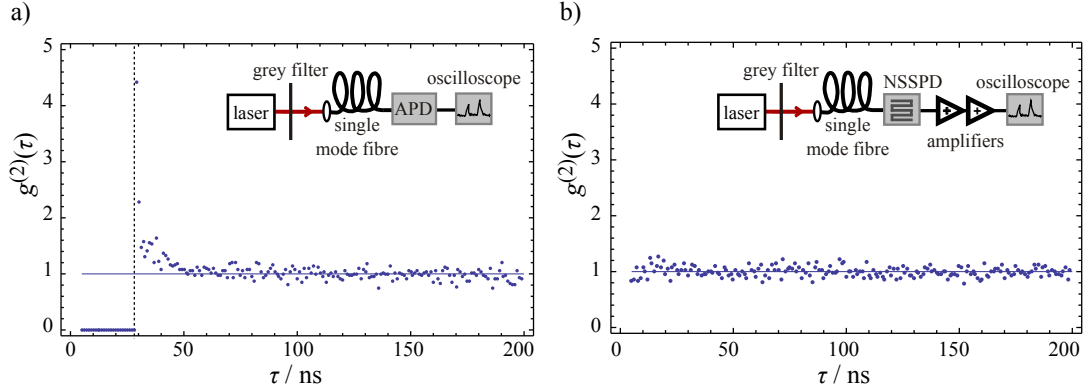
Figure 5.7: Second-order correlations of a laser field measured with a single detector for time differences τ between 5 ns and 200 ns. (a) Using a commercial APD, a dead time of 29 ns can be observed (indicated by dashed line). The bunching observed between correlation times of 30 ns and 50 ns is due to afterpulsing. For a rate of 300,000 s^{-1} and an afterpulsing probability of 0.5% one out of eleven events is an afterpulsing event and contributes to the area above the solid line ($g^{(2)}(\tau) = 1$). (b) Same measurement with a NSSPD with a dead time below 5 ns. Since only time differences larger than 5 ns were recorded no dead time effect was resolved. The absence of any correlation indicates a Poissonian photon number distribution.
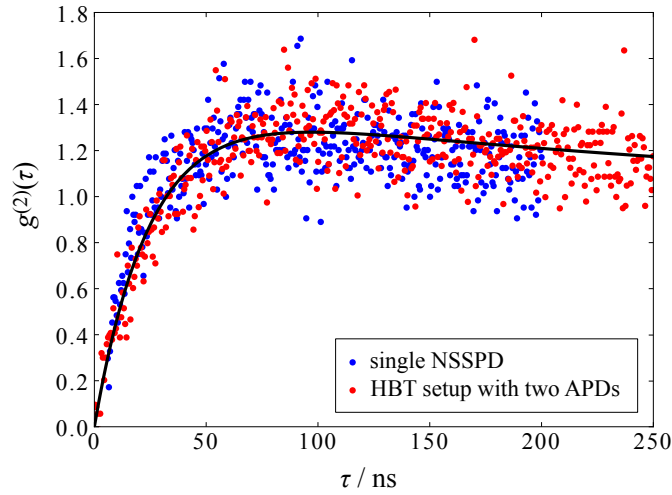
Figure 5.8: Measurement of the $g^{(2)}$-function in the single detector configuration 1 of figure 5.5 (blue dots) and the standard HBT configuration, configuration 2 of figure 5.5 (red dots), respectively. The black line is a fit to a three-level rate equation model: as shown in section 3.3 an additional bunching is observed due to occasional population of a metastable singlet state.

6 State Discrimination Strategies

In quantum theory, a measurement on a quantum object generally alters the initial state. In section 2.3, difficulties have been outlined that occur when the task is to identify an arbitrary quantum state, caused by the collapse of the wave function and the no-cloning theorem.

In this chapter, the scenario of discriminating states from a given set of possible states is examined. Often, the state to be identified is not arbitrary but is one from a known set. In quantum information and communication [21], e.g. in quantum cryptography [1], this is usually the set $\{|0\rangle, |1\rangle\}$ of the states in which 0 and 1 are encoded.

In the first part of this chapter, some terms and definitions of different discrimination strategies are introduced. In the second part, an experiment to discriminate two non-orthogonal mixed single-photon states unambiguously is presented, and in the last part an experiment where two such states (which cannot be discriminated unambiguously) are discriminated with maximum confidence is shown.

## 6.1 Introduction to the Discrimination of Quantum States

In this work, only cases where two light states are discriminated are discussed. These states are fully characterised by their density operators ρ_1 and ρ_2. Generalised measurements (cf. section 2.3.1) with three possible measurement results are considered: the measurement outcome indicates either state 1 or state 2 (conclusive results) or neither of the two states is identified (inconclusive results). This kind of measurement can be associated with a set of three positive operators E_0, E_1, E_2, also called detection or probability operators [138]. The detection operators are defined in a way that $\mathrm{Tr}\,(\rho_j E_k)$, $j, k \in \{1, 2\}$, is the probability that with the state initially being ρ_j the measurement outcome indicates that it was state ρ_k. E_0 represents inconclusive measurement results, i.e. $\mathrm{Tr}\,(\rho_j E_0)$ is the probability for an inconclusive result given the initial state ρ_j. The E_k fulfil the relation

$$E_0 + E_1 + E_2 = I_d \tag{6.1}$$

with I_d being the identity operator in the d-dimensional Hilbert space spanned by the eigenstates of ρ_1 and ρ_2 corresponding to non-zero eigenvalues.

If all the measurement operators are mutually orthogonal, the measurement is a projective (or von Neumann) measurement but this is not necessarily the case. In general, the set $\{E_0, E_1, E_2\}$ is a positive operator-valued measure (POVM) as introduced in section 2.3.1.
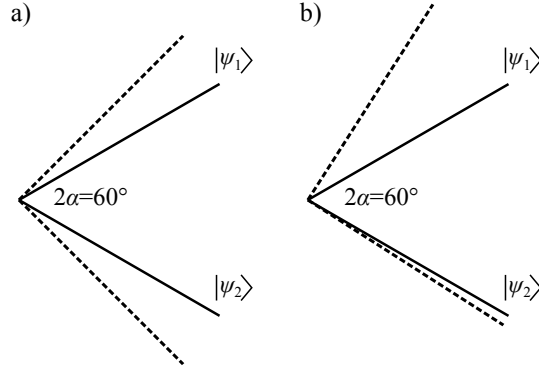
Figure 6.1: Minimum-error discrimination of two pure states $|\psi_1\rangle$ and $|\psi_2\rangle$ separated by an angle $2\alpha = 60°$. The dashed lines show the basis for the optimum projective measurement for the cases (a) $\eta_1 = \eta_2 = 0.5$ and (b) $\eta_1 = 0.1$, $\eta_2 = 0.9$. The error obtained by a projective measurement on this basis is given by $P_H = 6.7\%$ and $P_H = 2.3\%$ for case (a) and (b), respectively.

To characterise a measurement, important figures of merit are the probability Q to obtain inconclusive results and the error probability P for the conclusive results. Assuming that the states ρ_1, ρ_2 occur with known prior probabilities η_1, η_2 ($\eta_1 + \eta_2 = 1$), we define $\rho = \eta_1 \rho_1 + \eta_2 \rho_2$. The probability for an inconclusive result is then given by

$$Q = \mathrm{Tr}\,(\rho E_0) = 1 - \mathrm{Tr}\,(\rho E_1) - \mathrm{Tr}\,(\rho E_2) \tag{6.2}$$

and the overall error probability equals

$$P_{\text{error}} = \eta_1 \mathrm{Tr}\,(\rho_1 E_2) + \eta_2 \mathrm{Tr}\,(\rho_2 E_1)\,. \tag{6.3}$$

6.1.1 Minimum-Error Discrimination and Helstrom Bound

The case that inconclusive results are not allowed, i.e. $E_0 = 0$ and thus $Q = 0$, is known as minimum-error discrimination. In this case it can be shown that the overall minimum of P is reached at the Helstrom bound [139]

$$P_H = \frac{1}{2}\left(1 - \mathrm{Tr}|\eta_2 \rho_2 - \eta_1 \rho_1|\right) \tag{6.4}$$

where $|A| = \sqrt{A^\dagger A}$ for any operator A. The minimum error probability P_H is obtained when E_1 projects on the subspace spanned by the eigenstates of $\eta_2 \rho_2 - \eta_1 \rho_1$ belonging to negative eigenvalues [140]. Minimum-error discrimination is a projective measurement.

An example for two non-orthogonal pure states $|\psi_1\rangle$, $|\psi_2\rangle$ is depicted in figure 6.1. Here, $|\psi_1\rangle$ and $|\psi_2\rangle$ are separated by an angle of $60°$. Figure 6.1a shows the basis to project on performing the minimum-error measurement for the case of equal prior

possibilities $\eta_1 = \eta_2 = 1/2$, in figure 6.1b it is assumed that the probability for state $|\psi_2\rangle$ is nine times higher than for $|\psi_1\rangle$, i.e. $\eta_1 = 0.1$ and $\eta_2 = 0.9$. Using equation 6.4 the minimum-error probability is given by $P_H = 6.7\%$ for the case $\eta_1 = \eta_2 = 1/2$ and by $P_H = 2.3\%$ for the case $\eta_1 = 0.1$ and $\eta_2 = 0.9$.

6.1.2 Optimum Maximum-Confidence Discrimination

The confidence C_j, $j \in \{1, 2\}$, is a figure of merit that characterises the reliability of each conclusive outcome. It is defined as the conditional probability that the state ρ_j was prepared given that outcome j was detected, i.e. [141]

$$C_j = P(\rho_j|j) = \frac{P(\rho_j, j)}{P(j)} = \frac{\eta_j \operatorname{Tr}(\rho_j E_j)}{\operatorname{Tr}(\rho E_j)} = \operatorname{Tr}\left(\tilde{\rho}_j \tilde{E}_j\right) \tag{6.5}$$

with $\tilde{\rho}_j = \eta_j \rho^{-1/2} \rho_j \rho^{-1/2}$, $\tilde{E}_j = \operatorname{Tr}(\rho E_j)^{-1} \rho^{1/2} E_j \rho^{1/2}$, and ρ again being $\rho = \eta_1 \rho_1 + \eta_2 \rho_2$. Denoting $\nu_{max}^{(1)}$ and $\nu_{min}^{(1)}$ the largest and the smallest eigenvalue of $\tilde{\rho}_1$, respectively, it can be shown that maximum confidences for the measurement outcomes $C_1^{(max)}$ and $C_2^{(max)}$ are given by [142]

$$C_1^{(max)} = \nu_{max}^{(1)} \quad \text{and} \quad C_2^{(max)} = 1 - \nu_{min}^{(1)}. \tag{6.6}$$

The measurement with maximum confidence is generally not unique [143]. A maximum-confidence measurement is called optimum when the probability Q to obtain inconclusive results (equation 6.2) is as small as possible [142].

   A strategy to find the generalised measurement operators for a optimal maximum-confidence measurement for two mixed states is investigated in [142]. Generally, the minimisation of Q is a difficult task, but for the case that $\operatorname{rank}(E_1, E_2) \leq 1$ a complete analytical solution can be found.
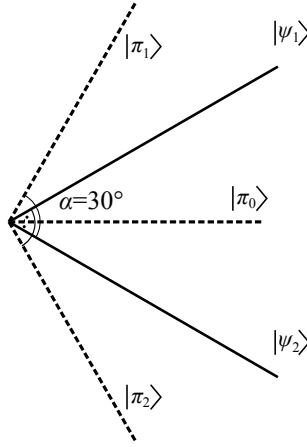
6.1.3 Optimum Unambiguous Discrimination

A measurement is called unambiguous when $\operatorname{Tr}(\rho_1 E_2) = \operatorname{Tr}(\rho_2 E_1) = 0$, which is possible only if the supports[1] of ρ_1, ρ_2 are not identical [144]. Optimum unambiguous discrimination of two mixed states is defined as an unambiguous measurement which minimises the probability Q to obtain inconclusive results (equation 6.2). Thus, optimum unambiguous discrimination is the special case of optimum maximum-confidence discrimination with $C_1^{(max)} = C_2^{(max)} = 1$.

   As an example, optimum unambiguous discrimination of two non-orthogonal pure states $|\psi_1\rangle$, $|\psi_2\rangle$ is sketched in figure 6.2. The vectors $|\pi_1\rangle$, $|\pi_2\rangle$, $|\pi_0\rangle$ are shown from which the measurement operators $E_j = |\pi_j\rangle\langle\pi_j|$, $j = 0, 1, 2$ for optimum unambiguous

---

[1]The support of a mixed state is the space spanned by its eigenvectors belonging to non-zero eigenvalues.

Figure 6.2: Optimum unambiguous discrimination of two pure states $|\psi_1\rangle$ and $|\psi_2\rangle$ with $\eta_1 = \eta_2 = 1/2$, separated by an angle $2\alpha = 60°$. The dashed lines indicate the states $|\pi_1\rangle$, $|\pi_2\rangle$, and $|\pi_0\rangle$, from which the measurement operators for optimum unambiguous discrimination $E_1 = |\pi_1\rangle\langle\pi_1|$, $E_2 = |\pi_2\rangle\langle\pi_2|$, and $E_0 = |\pi_0\rangle\langle\pi_0|$ are obtained.

discrimination are obtained. In this example the $|\pi_j\rangle$ are given by [141]

$$|\pi_1\rangle \;=\; \frac{\sqrt{1-\cos\gamma}}{\sin^2\gamma}\cdot\left(|\psi_1\rangle - \cos\gamma|\psi_2\rangle\right) \tag{6.7}$$

$$|\pi_2\rangle \;=\; \frac{\sqrt{1-\cos\gamma}}{\sin^2\gamma}\cdot\left(|\psi_2\rangle - \cos\gamma|\psi_1\rangle\right) \tag{6.8}$$

$$|\pi_0\rangle \;=\; \frac{\sqrt{\cos\gamma}}{\sin^2\gamma}\cdot\Big(\left(|\psi_1\rangle - \cos\gamma|\psi_2\rangle\right) + \left(|\psi_2\rangle - \cos\gamma|\psi_1\rangle\right)\Big) \tag{6.9}$$

with $\gamma = 2\alpha$ being the angle between $|\psi_1\rangle$ and $|\psi_2\rangle$, i.e. $\cos\gamma = \langle\psi_1|\psi_2\rangle$. Obviously, here $\langle\psi_1|\pi_2\rangle = \langle\psi_2|\pi_1\rangle = 0$.

Experimental Optimum Unambiguous Discrimination of two Pure States

Experimentally, optimum unambiguous discrimination of two pure states has already been performed more than one decade ago [145, 146]. Here, a short overview of the experiment performed by Clarke et al. [146] is given because our experimental setup used to discriminate two mixed states (section 6.2) is very similar, and the experiment discriminating two pure states is a good showcase to understand the basic ideas.

In the experiment, the task is to discriminate two (non-orthogonal) polarisation states $|\psi_+\rangle$ and $|\psi_-\rangle$, given by

$$|\psi_\pm\rangle = \cos\alpha|H\rangle \pm \sin\alpha|V\rangle \tag{6.10}$$

input: $|\psi_\pm\rangle = \cos\alpha |H\rangle \pm \sin\alpha |V\rangle$

HWP: half-wave plate
PBS: polarising beam splitter

output: $\sin\alpha\,(|V\rangle \pm |H\rangle)$
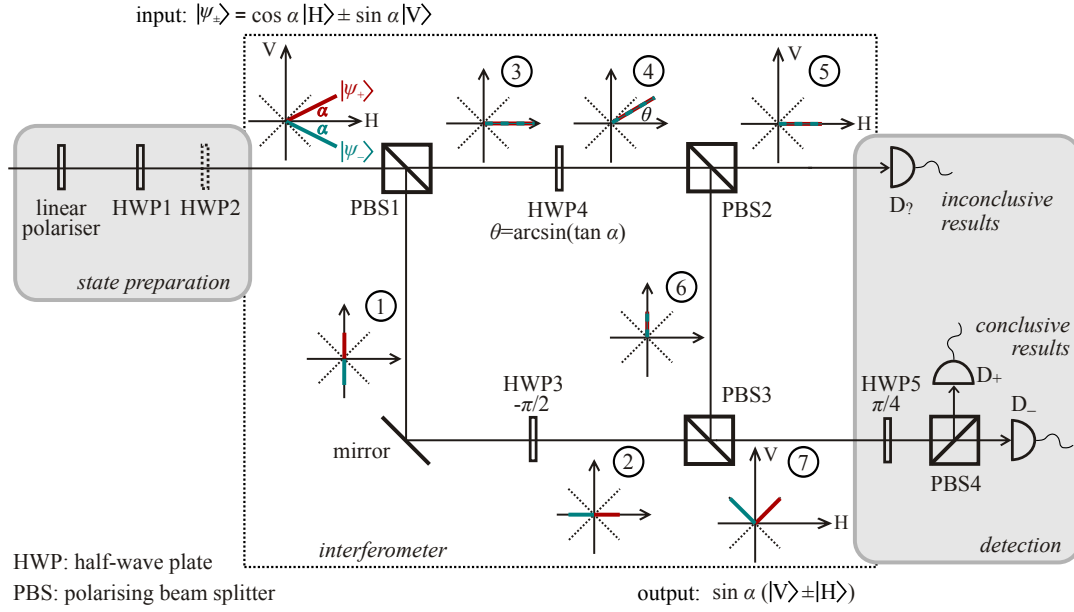
Figure 6.3: Setup for optimum unambiguous discrimination of two pure polarisation states $|\psi_+\rangle$ and $|\psi_-\rangle$ separated by an angle 2α. The input state $|\psi_\pm\rangle$ is prepared using a linear polariser and half-wave plates HWP1, HWP2 as described in the text. The polarisation states after different manipulation steps in the interferometer are summed in table 6.1. The inconclusive results are detected at detector $D_?$. At stage 7 either of two orthogonal states $1/\sqrt{2}(|V\rangle \pm |H\rangle)$ can be found with probability $2\sin^2\alpha$ (see table 6.1), which are discriminated without errors at detectors D_+ and D_-, respectively.

input	$|\psi_\pm\rangle = \cos\alpha|H\rangle \pm \sin\alpha|V\rangle$
stage 1	$\pm \sin\alpha|V\rangle$
stage 2	$\pm \sin\alpha|H\rangle$
stage 3	$\cos\alpha|H\rangle$
stage 4	$\cos\alpha(\cos\theta|H\rangle + \sin\theta|V\rangle)$
stage 5	$\cos\alpha\cos\theta|H\rangle = \cos\alpha\sqrt{1-\tan^2\alpha}\,|H\rangle$
stage 6	$\cos\alpha\sin\theta|V\rangle = \cos\alpha\tan\alpha|V\rangle = \sin\alpha|V\rangle$
output	$\sin\alpha(|V\rangle \pm |H\rangle)$

Table 6.1: States after different manipulation steps (see figure 6.3). The non-orthogonal input states $|\psi_\pm\rangle$ are transformed to one of the orthogonal output states $1/\sqrt{2}(|V\rangle \pm |H\rangle)$ with probability $|\sin\alpha(|V\rangle \pm |H\rangle)|^2 = 2\sin^2\alpha$.

where $|H\rangle$ and $|V\rangle$ denote the horizontal and vertical polarisation basis vectors, respectively, and $0 \leq \alpha \leq \pi/4$ is the half angle of separation between the states, thus $\langle\psi_+|\psi_-\rangle = \cos 2\alpha$.

Figure 6.3 shows the experimental setup to discriminate $|\psi_+\rangle$ and $|\psi_-\rangle$ unambiguously with minimum amount of inconclusive results. The input state is prepared using a linear polariser and one or two half wave plates (HWPs). HWP1 is adjusted such that it turns the polarisation to prepare $|\psi_+\rangle$. HWP2 performs an inversion of the polarisation with respect to the horizontal axis, i.e. by placing HWP2 $|\psi_+\rangle$ is transferred to $|\psi_-\rangle$ independently of α. After preparation, the input state $|\psi_\pm\rangle = \cos\alpha|H\rangle \pm \sin\alpha|V\rangle$ is sent to an interferometer as depicted in figure 6.3, which contains three polarising beam splitters (PBS1-3) and two HWPs. At HWP1 the polarisation is rotated by $-\pi/2$ and at HWP2 by $\theta = \arcsin(\tan\alpha)$. The transformations on the input state $|\psi_\pm\rangle$ by the interferometer are shown in figure 6.3 and table 6.1.

In summary, the interferometer transforms the non-orthogonal input states into orthogonal output states $(|\psi_\pm\rangle_7)$. The transformation is not in all the cases successful. If it fails, a photon is detected at detector $D_?$. The failure probability, i.e. the probability to obtain inconclusive results is given by

$$Q = ||\psi_\pm\rangle_5|^2 = \cos^2\alpha(1 - \tan^2\alpha) = \cos^2\alpha - \sin^2\alpha = \cos 2\alpha. \qquad (6.11)$$

The orthogonal output states can be discriminated without error at detectors D_+ ($|\psi_+\rangle$ prepared) and detector D_- ($|\psi_-\rangle$ prepared). The probability to obtain conclusive results is

$$P_{\text{concl}} = ||\psi_\pm\rangle_7|^2 = 2\sin^2\alpha = 1 - Q. \qquad (6.12)$$

6.2 Experimental Optimum Unambiguous Discrimination of Two Mixed Single-Photon States

For optimum unambiguous discrimination of mixed states, the discrimination strategies are basically the same as for the case of pure states, for which examples have been given above. However, theoretical evaluation and experimental implementation are more challenging. The optimum measurement for unambiguously discriminating between a pure state and a mixed state was already derived in 2003 [147] and experimentally realised one year later [148]. For distinguishing two mixed states, complete solutions for the optimum measurement have been obtained for special cases [144, 149–153] and recently a classification of the measurements yielding optimum unambiguous discrimination between two completely arbitrary mixed states has been given [153]. Experimentally, so far state discrimination [145, 146, 148, 154–157] was mostly based on photons from a laser beam, except for two recent ones using photons from parametric down conversion for extending the strategy of minimum-error discrimination to the availability of multiple copies [158] and to entangled states [159].

Here, the experimental realisation of optimum unambiguous discrimination between

two mixed single-photon states is presented. The mixed states refer to a four-dimensional Hilbert space, represented by the photon polarisation and its spatial paths. The states belong to a special class of similar states, $\rho_2 = U\rho_1 U^\dagger$. States of this kind have been proposed for secure quantum cryptography based on two mixed states [160] and the optimum measurement for unambiguously discriminating them has been theoretically derived in [152]. The photons for this experiment were obtained from a quantum-dot based true single-photon source. The experimental results presented in this section have been published in [161].

6.2.1 Experimental Implementation

The experimental implementation for unambiguously discriminating two mixed states ρ_1, ρ_2 presented here is based on a proposal by Herzog and Benson [141]. It starts from a general mixed single-photon state

$$\rho_0 = r_{11}|H\rangle_1\langle H|_1 + r_{22}|V\rangle_2\langle V|_2 + r_{12}|H\rangle_1\langle V|_2 + r_{21}|V\rangle_2\langle H|_1 \qquad (6.13)$$

where $|H\rangle_i$ and $|V\rangle_i$ refer to horizontal and vertical polarisation, respectively, and the indices $i = 1, 2$ correspond to the two output ports of a polarizing beam splitter. The states to be discriminated, ρ_1 and ρ_2, are obtained with equal probability $\eta_1 = \eta_2 = 1/2$ from ρ_0 via

$$\rho_1 = U^{(+)}\rho_0 U^{(+)\dagger} \quad \text{or} \quad \rho_2 = U^{(-)}\rho_0 U^{(-)\dagger}. \qquad (6.14)$$

Here, the unitary transformations $U^{(+)}$ and $U^{(-)}$ are composed of rotations by an angle α in two mutually orthogonal two dimensional subspaces, spanned by the states $|H\rangle_1$ and $|V\rangle_1$, on the one hand, and $|H\rangle_2$ and $|V\rangle_2$, on the other hand. $U^{(\pm)} = U_1^{(\pm)} \otimes U_2^{(\pm)}$ is chosen in a way that

$$U_1^{(\pm)}|H\rangle_1 = \cos\alpha|H\rangle_1 \pm \sin\alpha|V\rangle_1 \equiv |r_\pm\rangle \qquad (6.15)$$

$$U_2^{(\pm)}|V\rangle_2 = \cos\alpha|H\rangle_2 \pm \sin\alpha|V\rangle_2 \equiv |s_\pm\rangle \qquad (6.16)$$

with $0 \leq \alpha \leq \frac{\pi}{4}$. The states ρ_1 and ρ_2 are two mixed states of rank 2, the supports of which jointly span a four dimensional Hilbert space. It has been shown [141] that for these particular mixed states unambiguous discrimination with minimum failure probability is achieved in a generalized measurement which performs an optimum unambiguous discrimination between the pairs of pure states $|r_\pm\rangle$ on the one hand and $|s_\pm\rangle$ on the other hand, yielding the minimum probability for inconclusive results $Q = \cos 2\alpha$ which does not depend on ρ_0.

A setup for the experimental realisation of unambiguous state discrimination of ρ_1 and ρ_2 was proposed in [141] as shown in figure 6.4. To create ρ_1 or ρ_2 a polarising beam splitter (PBS) and two half-wave plates (HWPs) are utilised. The interferometers placed in the outputs of the PBS are basically the same as the one in figure 6.3.

Figure 6.5 depicts a scheme of the setup utilised here and figure 6.6 a photograph of the interferometers. It is equivalent to the one proposed in [141], but its more compact
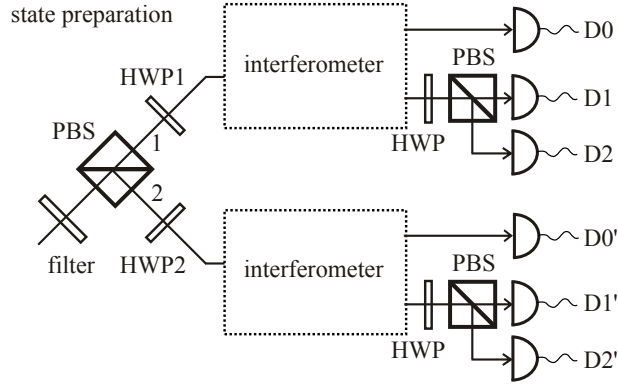
Figure 6.4: Setup for optimum unambiguous discrimination of two mixed single-photon states ρ_1 and ρ_2 as proposed in [141]. The input state is prepared using a polarising beam splitter (PBS) and half-wave plates (HWPs) as described in the text. The interferometers are basically the same as the one in figure 6.3. Inconclusive results are detected at detectors D0 and D0′, conclusive results at D1, D1′ and D2, D2′ respectively.
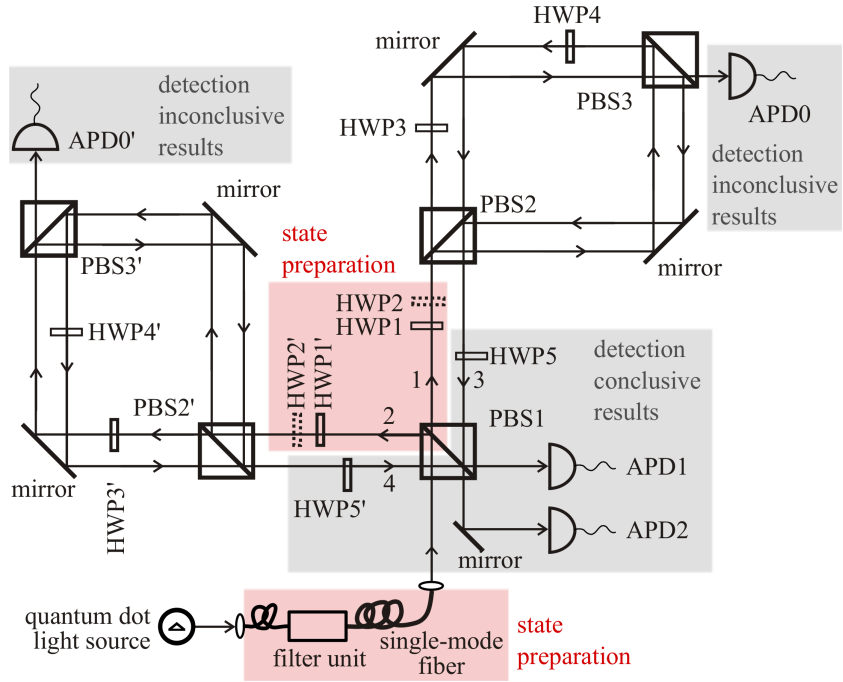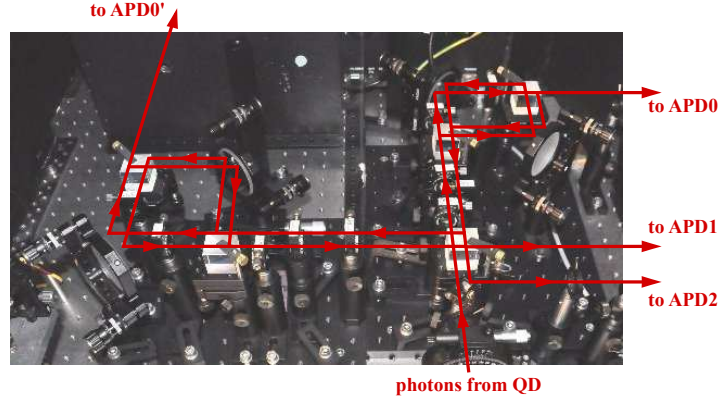

Figure 6.5: Experimental setup for optimum unambiguous discrimination of two mixed single-photon states ρ_1 and ρ_2. The input state is prepared and transformed as described in the text. The inconclusive results are detected at the avalanche photodiodes APD0 and APD0′, conclusive results at APD1 and APD2, respectively.

Figure 6.6: Photograph of the interferometers.

design results in several experimental advantages. Firstly, it obviously requires less detectors. Secondly, the interferometers are very stable because in each interferometer the light in both arms passes the same mirrors and beam splitters. Due to this stability there was no need for active stabilisation. Still the measurement could be repeated on following days without any realignment.

The incoming light passes a first polarizing beam splitter (PBS1). The photon state after PBS1 is given by equation 6.13. The transformation $U^{(+)}$ or $U^{(-)}$ is done at half-wave plates HWP1, HWP1′, HWP2, HWP2′. At HWP1 and HWP1′ the polarisation is turned by α and $-(90 - \alpha)$, respectively. Thus the state ρ_1 is prepared according to equation 6.14. To prepare ρ_2 HWP2 and HWP2′ are inserted additionally. After preparation of either ρ_1 or ρ_2, the states $|r_\pm\rangle$ and $|s_\pm\rangle$ have to be discriminated at the two different paths of the setup, respectively. For this task HWP3, HWP3′ are set to turn the polarisation of the light by an angle $\theta_3 = \arcsin(\tan\alpha)$ and HWP4, HWP4′ by $\theta_4 = \frac{\pi}{2}$ [141]. The inconclusive results are detected at the avalanche photodiodes APD0 and APD0′. At the output of each interferometer the states $|r_+\rangle$, $|s_+\rangle$ or $|r_-\rangle$, $|s_-\rangle$ are transformed to orthogonal states collinear to $|V\rangle_3 \pm |H\rangle_3$ and $|V\rangle_4 \pm |H\rangle_4$ where + (-) applies for the case that ρ_1 (ρ_2) was prepared initially. By rotating the interferometer outcomes at HWP5, HWP5′ by angles of $\theta_5 = \frac{\pi}{4}$, $\theta_{5'} = -\frac{\pi}{4}$, the conclusive results for input states ρ_1 (ρ_2) are detected at APD1 (APD2).

The single-photon source employed here consists of a single InGaAs/GaAs quantum dot embedded in a microcavity [162]. A detailed characterisation is shown in section 3.2.3. In this experiment we used continuous electrical pumping. A fibre-coupled tunable filter of 1 nm width (Koshin Kogaku) was used to spectrally filter out the exciton emission. The device has a single-photon emission rate of 30 kHz (after spectral filtering). Figure 3.10 shows a measurement of the $g^{(2)}$-function, clearly demonstrating single-photon emission.
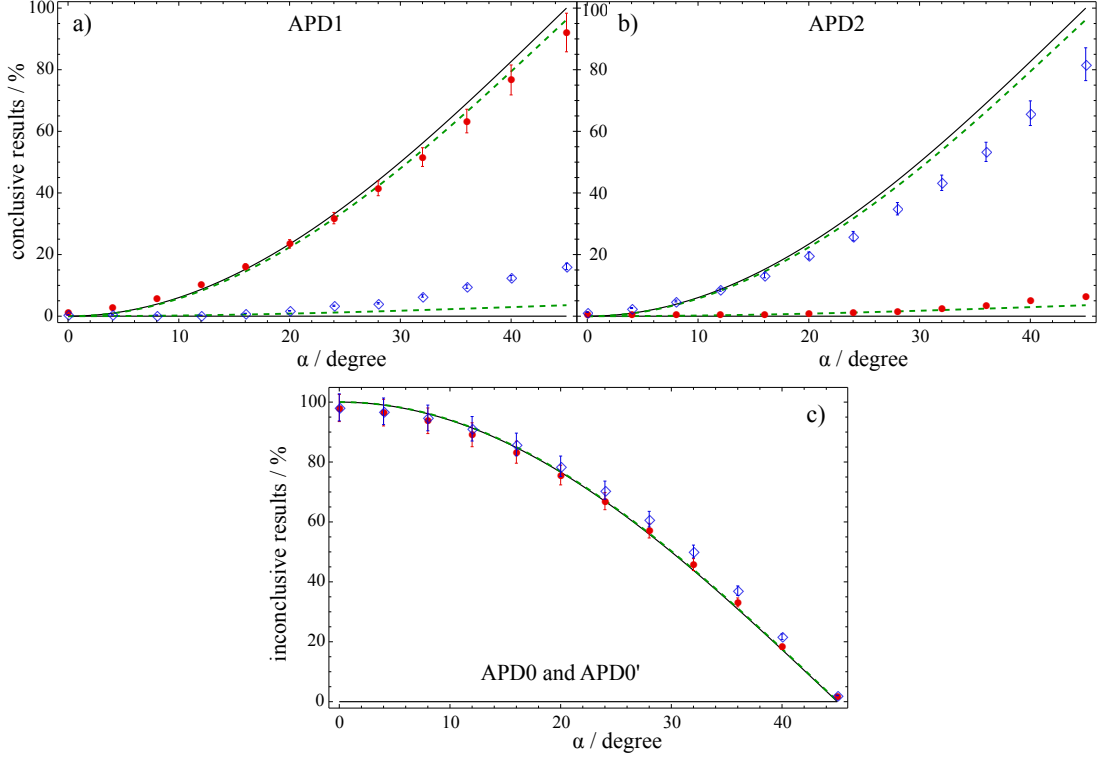
Figure 6.7: Experimental results for optimum unambiguous discrimination of two mixed single-photon states ρ_1 and ρ_2 against the half angle of separation α for the cases that ρ_1 (red circles) and ρ_2 (blue diamonds) were prepared. The black lines show the theoretical curves (equations 6.17 and 6.18), and the dashed green lines modified expectations, taking the imperfections of the HWPs into account (see text). (a), (b) Percentage of conclusive results (counts on APD1 and APD2, respectively). (c) Percentage of inconclusive results (sum of counts on APD0 and APD0′).

6.2.2 Experimental Results

In figures 6.7a-c the measurement results are shown for the two mixed input states ρ_1 (red dots) and ρ_2 (blue diamonds). All count rates are given in percent of the sum of count rates on the four APDs. The total count rate was typically around 2000 s^{-1}. The count rates have a statistical error of around 5% (error bars). Also shown are the theoretical curves (black lines), which are given by given by [141]

$$Q = \cos 2\alpha \tag{6.17}$$

for the relative number of inconclusive results and

$$1 - Q = 2\sin^2 \alpha \tag{6.18}$$

for the conclusive ones. The non-vanishing count rate on APD1 (APD2) for the case that ρ_2 (ρ_1) was prepared initially is mainly due to imperfections of the optical elements, especially the HWPs. When the polarisation is rotated by 90°, the error of the HWPs is around 0.3%, i.e. 0.3% of the intensity is not rotated. Taking this error into account, the theoretical expectations can be modified, as also shown in figures 6.7a-c (dashed green lines).

For the case that ρ_1 was prepared initially (red dots), the experimental data matches very well with the modified theoretical expectations. However, for the input state ρ_2 the performance of our setup is not as good. The reason is, that switching between the two input states is done by placing two additional HWPs (HWP2 and HWP2′ in figure 6.5). This causes in a slight displacement of the input beams of both interferometers resulting in an inferior performance of the setup. The interferometers could be realigned for this case (at the expense of inferior operation for the input state ρ_1), but it was not possible to obtain optimal performance for both cases at the same time.

Figure 6.8 depicts the error rates. The experimental error rates are the number of counts on the "wrong" APD divided by the number of all conclusive results, i.e. the counts on APD2 (APD1) divided by the counts on APD1 and APD2 for the case that ρ_1 (ρ_2) was prepared initially. Theoretically, the errors should be zero but taking the imperfections of the HWPs into account (dashed green line), there is still a non-vanishing possibility for counts on the wrong APD. For the case that ρ_1 was prepared initially, our expectations were met. The higher error rates for the the input state ρ_2 arises from the misalignment of the beams when HWP2 and HWP2′ are inserted.

Also shown in figure 6.8 is the Helstrom bound $P_H = \frac{1}{2} - \frac{1}{4}\mathrm{Tr}|\rho_1 - \rho_2|$ (equation 6.4), i.e. the theoretical error rate for the projective measurement which discriminates
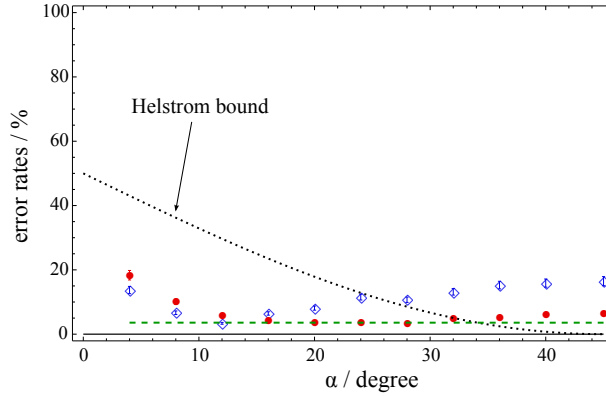
Figure 6.8: Error rates for the conclusive results for the cases that ρ_1 (red circles) and ρ_2 (blue diamonds) were prepared against the half angle of separation α. The dashed green line shows the expected error rate taking the imperfections of the HWPs into account. The dotted line is the theoretical limit for the projective measurement achieving minimum-error discrimination (see text).

ρ_1 and ρ_2 with minimum error probability (dotted black line). Since for orthogonal state, the states can theoretically be discriminated without errors by a projective measurement, for half angles of separation close to 45° the experimental errors that were obtained with our setup are above the minimum error applying a projective measurement. However for for half angles of separation below around 30°, our experimental errors are below the theoretical error limit for discrimination by a projective measurement, i.e. in these cases the application of our measurement scheme is superior to the best possible projective measurement.

This experiment is the first experimental realisation of optimum unambiguous discrimination between two quantum states which both are mixed.

6.3 Experimental Optimum Maximum-Confidence Discrimination of Two Mixed Single-Photon States

In the last part of this chapter, a case is discussed where two photon states can not be discriminated unambiguously. Here, the strategy of optimum maximum-confidence discrimination is pursued.

The density matrix ρ of a photon in two-dimensional Hilbert space, here describing the polarisation state of a photon in a definite path, can in general be written as

$$\rho = p|\psi\rangle\langle\psi| + (1-p)\frac{I_2}{2} \tag{6.19}$$

where $|\psi\rangle$ denotes some pure state, p with $0 < p \le 1$ characterises the purity, and I_2 is the identity operator in the two-dimensional Hilbert space. Different mixed states of this kind have identical supports and thus cannot be discriminated unambiguously.

In this section an experiment for optimum maximum-confidence discrimination of two partly polarised single-photon states with the same purity is described. Some of the experimental results presented here have been published in [161].

6.3.1 Experimental Implementation

For the implementation of the maximum-confidence discrimination measurement we utilised partially polarised photons. Their density matrix can be written in the form of equation 6.19, then $|\psi\rangle$ denotes a pure polarisation state, and p is a measure for the degree of polarisation. The states ρ_+ and ρ_- to be discriminated here are defined by

$$\rho_\pm = p|\psi_\pm\rangle\langle\psi_\pm| + (1-p)\frac{I_2}{2} \quad \text{with} \quad |\psi_\pm\rangle = \cos\beta|H\rangle \pm \sin\beta|V\rangle \tag{6.20}$$

Figure 6.9: Experimental setup for optimum maximum-confidence discrimination of two mixed single-photon states ρ_+ and ρ_-. The input state is prepared and transformed as described in the text. The inconclusive results are detected at avalanche photodiode APD0, conclusive results at APD1 and APD2, respectively.

When assuming equal prior probabilities for ρ_+ and ρ_-, the maximum confidences C_+ and C_- for the measurement are [142]

$$C_+ = C_- = \frac{1}{2}\left(1 + \frac{p\sin 2\beta}{\sqrt{1 - p^2\cos^2 2\beta}}\right). \qquad (6.21)$$

They are achieved in a generalised measurement, at the expense of inconclusive results. Here, the minimum probability of inconclusive results is given by [141, 142],

$$Q = p\cos 2\beta. \qquad (6.22)$$

By contrast, for the projective minimum-error measurement without inclusive results, the maximum confidences are given by [142]

$$C_+^{(\text{proj})} = C_-^{(\text{proj})} = \frac{1}{2}(1 + p\sin 2\beta). \qquad (6.23)$$

The measurement scheme applied here was proposed by Herzog and Benson [141] for discriminating two partially polarised single-photon states with the same degree of polarisation with maximum confidence and optimally, i.e. with the smallest possible probability of inconclusive results. Figure 6.9 shows the experimental setup.

The same true single-photon source as described in section 6.2.1 consisting of an

InGaAs/GaAs QD was utilised. It was verified experimentally that the light emitted by the QD source has no preferential polarisation. For spectral filtering of a single excitonic transition in the QD, it passes a fibre-coupled filter unit (Koshin Kogaku) which contains a longpass and a tunable bandpass of a width of 1 nm. After the fibre-coupled filter unit it is in a partially linearly polarised state $\rho = p|\psi\rangle\langle\psi| + (1-p)\frac{I_2}{2}$, where $p = 0.55$ was measured.

At the half-wave plates HWP1 (HWP1 and HWP2) the state ρ_+ (ρ_-) as given by equation 6.20 is prepared with probability 1/2. At HWP3 the polarisation is turned by

$$\theta_3 = \arccos\sqrt{\frac{2p\cos 2\beta}{1 + p\cos 2\beta}}. \tag{6.24}$$

at HWP4 by $\theta_4 = \frac{\pi}{2}$, and at HWP5 by $\theta_5 = \frac{\pi}{4}$ as proposed in [141]. The results are collected at three avalanche photodiodes (APDs), the inconclusive results at APD0 and the conclusive ones at APD1, indicating the presence of ρ_+, and at APD2 for ρ_-, respectively. A total count rate of around 2000 s^{-1} was measured when using the true single-photon source.

6.3.2 Experimental Results

Figure 6.10 shows the measured count rates against the half angle of separation β between the $|\psi_\pm\rangle$ (see equation 6.20). Red circles indicate initial preparation of ρ_+, blue diamonds preparation of ρ_-. All count rates are given in percent of the sum of count rates on the four APDs and have a statistical error of around 5% (error bars). The total count rate was typically around 2000 s^{-1}. The black lines depict the theoretical curves. For the inconclusive results (figure 6.10c) it is given by equation 6.22. For the conclusive results (figure 6.10a and b) the theoretical curves are obtained from equations 6.21 and 6.22 (see appendix A) and result in

$$R_{1,2} = \frac{1 - p\cos 2\beta}{2}\left(1 + \frac{p\sin 2\beta}{\sqrt{1 - p^2\cos^2 2\beta}}\right) \tag{6.25}$$

and

$$W_{1,2} = \frac{1 - p\cos 2\beta}{2}\left(1 - \frac{p\sin 2\beta}{\sqrt{1 - p^2\cos^2 2\beta}}\right), \tag{6.26}$$

where R_j (W_j), $j = 1, 2$, is the fraction of "right" ("wrong") results on APDj. As in section 6.2.2, a modified theoretical curves were calculated, taking the imperfections of the HWPs into account. It was assumed that rotating the polarisation by 90°, the error of the HWPs is 0.3%, i.e. 0.3% of the intensity is not rotated. The dashed green lines in figures 6.7a-c show the expected values including the HWP errors.

Here, the agreement with the theoretical expectations is not as good as for the unambiguous-state-discrimination (USD) experiment (section 6.2.2). It seems that inconclusive results are detected with a higher efficiency than conclusive ones. A
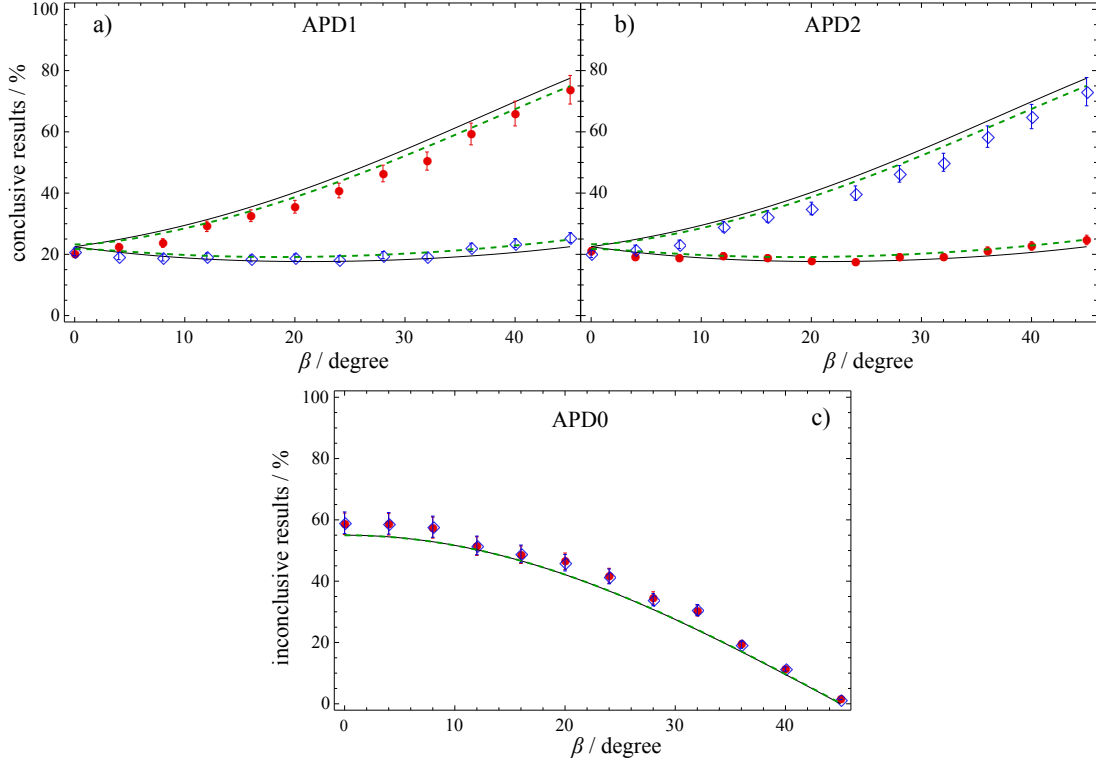
Figure 6.10: Experimental results for optimum maximum-confidence discrimination of two mixed single-photon states ρ_+ and ρ_- against the half angle of separation β. Red circles indicate preparation of ρ_+, blue diamond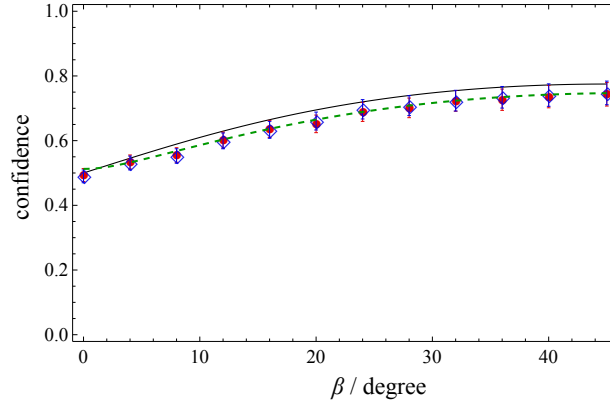s preparation of ρ_-. The black lines are the theoretical curves given by equations 6.25, 6.26, and 6.22, and the dashed green lines the theoretical expectations taking the imperfections of the HWPs into account (see text). (a), (b) Conclusive results (counts on APD1 and APD2, respectively), given as a percentage of all counts on the three APDs. (c) Inconclusive results (counts on APD0) as a percentage of all counts on the three APDs.

reason could be a better alignment of APD0 or a bad alignment of one of the optical elements after PBS2 (see figure 6.9). Unlike in the USD experiment, there is not a big difference in performance of the setup for the cases that HWP2 is or is not placed. However, the conclusive results on the "right" APDs are slightly lower than expexted. Probably here the interferometer was not optimised for one of the preparation states, but was in a "tradeoff" position between the best alignment for ρ_+ and ρ_-, respectively (cf. discussion in section 6.2.2).

Figure 6.11 shows the results for the confidence against the half angle of separation β for the cases that ρ_+ (red dots) or ρ_- (blue diamonds) was prepared. Here, the theoretical curve (black line) is given by equation 6.21. The dashed curve depicts the expected behaviour taking the imperfections of the HWPs into account. The measured

Figure 6.11: Confidence against the half angle of separation β for the cases that ρ_+ (red circles) and ρ_- (blue diamonds) were prepared initially. The black line depicts the theoretical curve and the dashed green line gives the expected values when the imperfections of the HWPs are taken into account (see text).

confidences are in agreement with the expected values for large angles of separation. For small angles, however, the measured confidence is slightly smaller than expected, which is probablity due to the imperfect alignment for both input states (see above).

According to equations 6.21 and 6.23, allowing for inconclusive theoretically results in a better confidence than for the case of a projective minimum-error measurement. However, for $p = 0.55$ the theoretical confidences $C_\pm$ for the implemented optimum maximum-confidence measurement and the confidences $C_\pm^{(\text{proj})}$ arising from the projective minimum-error measurement differ in less than 0.02 for all angles β. This difference is too small to be resolved by the experimental data.

Still, this experiment shows that optimum-minimum error discrimination could be implemented experimentally for the first time for two mixed states from a true single-photon source.

7 Summary and Outlook

7.1 Summary

Subject of this work were experiments that deal with different aspects of the detection of quantum states of light. The two main questions addressed in particular were firstly, to perform an experiment as fundamental as possible to prove the quantum nature of light, and secondly, the experimental implementation of strategies to discriminate mixed single-photon states unambiguously or, when this is not possible, with maximum confidence.

The quantum nature of light has been postulated since A. Einstein explained the photoelectric effect assuming energy quantisation for the light field. This non-classical behaviour can be proven by measuring the photon statistics of a quantum emitter. Usually, this is done with the so-called Hanbury-Brown-Twiss (HBT) setup, which consists of a beam splitter and two detectors. Here, it was shown that this experiment can be simplified substantially, and for the first time the quantum nature of light was demonstrated with a setup with only a quantum emitter and a single detector. This was possible utilising a nanowire superconducting single-photon detector (NSSPD). These detectors have been developed within the last decade and exploit the fact that superconductivity can be disturbed, when photons are absorbed in the superconductor. They provide some advantages over the well-established avalanche photodiodes, namely their ability to work at very low dark count rates even in the infra-red (IR), their low jitter, and, what was crucial here, very short dead times of only a few nanoseconds. The detector structures utilised here were fabricated at Delft University of Technology. In this thesis, a procedure was developed to couple these structures effectively to a single-mode optical fibre. As quantum emitter a single nitrogen-vacancy centre in a diamond nano-crystal was utilised, with a lifetime of around 30 ns, which is long compared to the dead time of our detector.

In the other main part of this work, experiments were performed that implement different strategies for optimal discrimination of quantum states. In quantum mechanics, a measurement involves the projection of the measured state on a certain basis, which means that usually not all the information necessary to fully identify the state (i.e. to reconstruct its density matrix) can be obtained from only one measurement. That means that, e.g., two non-orthogonal states cannot be discriminated without errors by one projective measurement. However, under certain conditions there are ways to discriminate such states unambiguously at the expense of allowing for inconclusive results. In this work experimental unambiguous discrimination of two mixed single-photon states was carried out for the first time. Furthermore, in

a different scenario, where unambiguous discrimination of the states is not possible, optimum maximum-confidence discrimination of two single-photon states could be implemented. The states to be discriminated were prepared with single-photons from a quantum-dot source. Thus, true single-photon states are utilised here to implement prove-of-principle experiments that require a setup of a complexity much beyond the standard characterisation setups as e.g. HBT setups or Michelson interferometers.

7.2 Outlook

The ability to detect single photons is necessary for every experiment where single photons are utilised. There are prominent applications in the field of quantum information and quantum communication, as quantum key distribution [1], quantum computing [163], or quantum entanglement and teleportation [164]. But also the investigation of the coupling between light and quantum emitters, or research in the area of plasmonics [165] require measurements on non-classical states of light. All these fields are subject of intense research at the moment, and the requirements for detection tools will thus be increasing further.

When photons are utilised for the transmission of quantum states over long distances, i.e. distances beyond a few metres, usually optical fibres are the transmission channel of choice. Since wavelengths of 1.3 μm or 1.5 μm are attenuated least in these fibres, detectors operating in the near IR are required. NSSPDs exhibit a good performance in this wavelength range, with a dark count rate of below 100 Hz at a reasonable quantum efficiency (which can even be increased by implementing them into cavity structures [128]). For instance, for long distance quantum key distribution, NSSPDs are employed in a rapidly growing amount of experiments [107].

Fast development takes place in implementing quantum sources into cavity structures, as e.g. Fabry-Perot resonators build of pairs of distributed Bragg reflectors [58], photonic crystal cavities [59], or whispering-gallery resonators [166]. In these setups, the emission into the cavity modes is enhanced due to the modification of the density of states by the cavity, and the source's lifetime is reduced. Thus, such sources are able to emit single photons at increased emission rates. That means, fast detectors, i.e. detectors with short dead times, are needed in order to make use of high emissions rates. For such sources, the intensity correlation times become shorter, which results in a need for a better time resolution in intensity-correlation measurements. NSSPDs are able to meet these demands, and they will become even faster, when the wire length is further decreased.

Shorter detector wires are becoming possible since recently progress is reported on the development of detectors which contain arrays of parallel wires [111, 120, 121]. Besides providing shorter dead times, this enables the detectors to discriminate between different photon numbers, which will be interesting for many future applications, especially in the implementation of quantum computing using linear optics [6].

In this work, it was shown that photon antibunching can be measured using only

a single detector, instead of the widely used HBT setup. The simplification can be made, when detectors are available with a dead time much shorter than the correlations times to be measured. With the expected decrease in detector dead times (which is e.g. for NSSPDs achieved by using parallel meander structures) this means that in many experiments HBT setups could be replaced by single detectors. Furthermore, a setup like the one utilised here can also instantaneously record higher order correlations, as e.g. $g^{(3)}$-functions. Using large detector arrays, it will also be possible to construct a $g^{(2)}$-*camera* which can take spatially resolved intensity-correlation images. Intensity correlation measurements are not only of interest in quantum optics, but also in a lot of classical application as fluorescence correlation spectroscopy [137]. Therefore a simplification of the experimental tools will have an impact in a wide range of applications.

When single photons are used to encode and transmit information, the photon state has to be read out by the receiver. For a fast and error-free communication it is important to obtain the necessary information about the photon states efficiently, i.e. by one measurement with high confidence and high success probability. Hence it is important to follow optimal state discrimination strategies. In particular, imperfect transmission channels result in non-orthogonal and mixed photon states. The experiments performed in this work give first examples how to deal with such kind of states in the future.

A Appendix

Theoretical Values for the Conclusive Results in the Optimum Maximum-Confidence Measurement

In section 6.3.2 the theoretical values R_j (W_j), $j = 1, 2$, is the fraction of "right" ("wrong") results on APDj are given. These can be obtained from equations 6.21 (confidences $C_\pm$) and 6.22 (fraction of inconclusive results Q) as shown here.

The confidence $C = C_\pm$ is equal for both input states and equals

$$C = \frac{R_1}{R_1 + W_1} = \frac{R_2}{R_2 + W_2} \tag{A.1}$$

for the respective cases that ρ_+ and ρ_+ were prepared initially. In both cases the count rates on all three APDs sum up to 1, i.e.

$$1 - Q = R_1 + W_2 = R_2 + W_1. \tag{A.2}$$

Replacing $W_2 = R_2 - R_1 + W_1$ from equation A.2 in equation A.1 results in

$$R_1^2 - (R_2 + W_1)R_1 + R_2 W_1 = 0 \tag{A.3}$$

which has the solutions $R_1 = W_1$ and $R_1 = R_2$. Here, $R_1 = W_1$ is the trivial case with $R_2 = W_2$ and $C = 1/2$, contradicting equation 6.21. For $R_1 = R_2$ follows $W_1 = W_2$, and thus the denominator in equation A.1 can be replaced by $1 - Q$ (from equation A.2), which gives

$$C = \frac{R_{1,2}}{1 - Q}. \tag{A.4}$$

Using also equations 6.21 and 6.22, it follows

$$
\begin{aligned}
R_{1,2} &= C(1-Q) = \frac{1}{2}\left(1 + \frac{p \sin 2\beta}{\sqrt{1 - p^2 \cos^2 2\beta}}\right) \cdot (1 - p \cos 2\beta) = \\
&= \frac{1 - p \cos 2\beta}{2}\left(1 + \frac{p \sin 2\beta}{\sqrt{1 - p^2 \cos^2 2\beta}}\right)
\end{aligned}
\tag{A.5}
$$

A Appendix

and

$$
\begin{aligned}
W_{1,2} &= 1 - Q - R_{1,2} = (1 - C)(1 - Q) = \\
&= \left(1 - \frac{1}{2} - \frac{1}{2}\frac{p\,\sin 2\beta}{\sqrt{1 - p^2\cos^2 2\beta}}\right) \cdot (1 - p\cos 2\beta) = \\
&= \frac{1 - p\cos 2\beta}{2}\left(1 - \frac{p\,\sin 2\beta}{\sqrt{1 - p^2\cos^2 2\beta}}\right).
\end{aligned}
\tag{A.6}
$$

Abbreviations

a.u.	arbitrary units
ac	alternate current
AFM	atomic-force microscope
APD	avalanche photodiode
BS	beam splitter
CCD	charge-coupled device
DBR	distributed Bragg reflector
dc	direct current
e.g.	*exempli gratia* (for example)
et al.	*et alii* (and others)
etc.	*et cetera* (and so forth)
FCS	fluorescence correlation spectroscopy
HBT	Hanbury-Brown-Twiss
HSQ	hydrogen silsequioxane
HWP	half-wave plate
i.e.	*id est* (that is)
IR	infra-red
MBE	molecular beam epitaxy
MOVPE	metal organic vapour phase epitaxy
N-V	nitrogen-vacancy
NEP	noise equivalent power
NSSPD	nanowire superconducting single-photon detector
PBS	polarising beam splitter
PMMA	polymethyl methacrylate
PMT	photomultiplier tube
POVM	positive operator-valued measure
QD	quantum dot
QKD	quantum key distribution
SK	Stranski-Krastanov
sm	single-mode
TES	transition-edge sensor
TIC	time interval counter
USD	unambiguous state discrimination
UV	ultraviolet
VAP	vortex-antivortex pair
ZPL	zero phonon line

Bibliography

[1] N. Gisin, G. Ribordy, W. Tittel, and H. Zbinden. Quantum cryptography. *Rev. Mod. Phys.*, 74(1):145–195, 2002.

[2] C. H. Bennett and G. Brassard. Quantum cryptography: Public key distribution and coin tossing. *Proc. IEEE Int. Conf. on Computers, Systems and Signal Processing, Bangalore, India*, pages 175–179, 1984.

[3] R. P. Feynman. Simulating physics with computers. *Int. J. Theor. Phys.*, 21(6–7):467–488, 1982.

[4] P. W. Shor. Algorithms for quantum computation: discrete logarithms and factoring. *Proc. 35th Ann. Symp. on Found. Comp. Science, IEEE*, pages 124–134, 1994.

[5] L. K. Grover. Quantum mechanics helps in searching for a needle in a haystack. *Phys Rev. Lett.*, 79(2):325–328, 1997.

[6] E. Knill, R. Laflamme, and G. J. Milburn. A scheme for efficient quantum computation with linear optics. *Nature*, 409(4):46–52, 2001.

[7] Y. Makhlin, G. Schön, and A. Shnirman. Josephson-junction qubits with controlled couplings. *Nature*, 398:305–307, 1999.

[8] G. R. Guthöhrlein, M. Keller, K. Hayasaka, W. Lange, and H. Walther. A single ion as a nanoscopic probe of an optical field. *Nature*, 414:49–51, 2001.

[9] R. Hanson, L. P. Kouwenhoven, J. R. Petta, S. Tarucha, and L. M. K. Vandersypen. Spins in few-electron quantum dots. *Rev. Mod. Phys.*, 79(4):1217–1265, 2007.

[10] E. Schrödinger. Quantisierung als Eigenwertproblem. *Ann. Physik*, 79:361–376, 1926.

[11] W. Heisenberg. *Die physikalischen Prinzipien der Quantentheorie*. Hirzel, Stuttgart, 1930.

[12] J. von Neumann. *Mathematische Grundlagen der Quantenmechanik*. Springer, Berlin, Heidelberg, New York, 1932.

[13] A. Einstein. Über einen die Erzeugung und Verwandlung des Lichtes betreffenden heuristischen Gesichtspunkt. *Annalen der Physik*, 17(6):132–148, 1905.

Bibliography

[14] M. Planck. Über das Gesetz der Energieverteilung im Normalspectrum. *Annalen der Physik*, 4:553–566, 1901.

[15] M. O. Scully and M. S. Zubairy. *Quantum Optics*. Cambridge University Press, 1997.

[16] D. F. Walls and G. J. Milburn. *Quantum Optics*. Springer, Berlin Heidelberg New York, 1994.

[17] R. J. Glauber. The quantum theory of optical coherence. *Physical Review*, 130:2529–2539, 1963.

[18] H. A. Bachor. *A guide to experiments in quantum optics*. Wiley-VCH, 1998.

[19] D. T. Phillips, H. Kleiman, and S. P. Davis. Intensity-correlation linewidth measurement. *Phys. Rev.*, 153(1):113–115, 1967.

[20] F. Jelezko and J. Wrachtrup. Single defect centres in diamond: A review. *phys. stat. sol. a*, 203(13):3207–3225, 2006.

[21] M. A. Nielsen and I. L. Chuang. *Quantum Computation and Quantum Information*. Cambridge University Press, 2000.

[22] W. Heisenberg. Über den anschaulichen Inhalt der quantentheoretischen Kinematik und Mechanik. *Zeitschr. f. Physik*, 43:172–198, 1927.

[23] J. M. Jauch and C. Piron. Generalized localizability. *Helvetica Physica Acta*, 40:559–570, 1967.

[24] P. Busch, M. Grabowski, and P. Lahti. *Operational Quantum Physics*. Springer, Berlin, 1995.

[25] G. M. D'Ariano, M. G. A. Paris, and M. F. Sacchi. Quantum tomography. *Adv. in Imaging and Electron Phys.*, 128:205–308, 2003.

[26] B. Lounis and M. Orrit. Single-photon sources. *Rep. Prog. Phys.*, 68(5):1129–1179, 2005.

[27] H. J. Kimble, M. Dagenais, and L. Mandel. Photon antibunching in resonance fluorescence. *Phys. Rev. Lett.*, 39(11):691–695, 1977.

[28] M. D. Eisaman, A. Migdall J. Fan, and S. V. Polyakov. Single-photon sources and detectors. *Rev. Sci. Instrum.*, 82:071101, 2011.

[29] A. Kuhn, M. Hennrich, and G. Rempe. Deterministic single-photon source for distributed quantum networking. *Phys. Rev. Lett.*, 89(6):067901, 2002.

[30] J. McKeever, A. Boca, A. D. Boozer, R. Miller, J. R. Buck, A. Kuzmich, and H. J. Kimble. Deterministic generation of single photons from one atom trapped in a cavity. *Science*, 303(5666):1992–1994, 2004.

[31] B. B. Blinov, D. L. Moehring, L. M. Duan, and C. Monroe. Observation of entanglement between a single trapped atom and a single photon. *Nature*, 428:153–157, 2004.

[32] M. Keller, B. Lange, K. Hayasaka, W. Lange, and H. Walther. Continuous generation of single photons with controlled waveform in an ion-trap cavity system. *Nature*, 431:1075–1078, 2004.

[33] J. Beugnon, M. P. A. Jones, J. Dingjan, B. Darquie, G. Messin, A. Browaeys, and P. Grangier. Quantum interference between two single photons emitted by independently trapped atoms. *Nature*, 440:779–782, 2006.

[34] F. De Martini, G. Di Giuseppe, and M. Marrocco. Single-mode generation of quantum photon states by excited single molecules in a microcavity trap. *Phys. Rev. Lett.*, 76(6):900–903, 1996.

[35] C. Brunel, B. Lounis, P. Tamarat, and M. Orrit. Triggered source of single photons based on controlled single molecule fluorescence. *Phys.Rev. Lett.*, 83(14):2722–2725, 1999.

[36] B. Lounis and W. E. Moerner. Single photons on demand from a single molecule at room temperature. *Nature*, 407:491–493, 2000.

[37] C. Kurtsiefer, S. Mayer, P. Zarda, and H. Weinfurter. Stable solid-state source of single photons. *Phy. Rev. Lett.*, 85(2):290–293, 2000.

[38] A. Beveratos, R. Brouri, T. Gacoin, J.-P. Poizat, and P. Grangier. Nonclassical radiation from diamond nanocrystals. *Phys. Rev. A*, 64(6):061802, Nov 2001.

[39] P. Michler, A. Kiraz, C. Becher, W. V. Schoenfeld, P. M. Petroff, Lidong Zhang, E. Hu, and A. Imamoglu. A quantum dot single-photon turnstile device. *Science*, 290:2282–2285, 2000.

[40] C. Santori, D. Fattal, J. Vuckovic, G. S. Solomon, and Y. Yamamoto. Indistinguishable photons from a single-photon device. *Nature*, 419:594–597, 2002.

[41] V. Zwiller, T. Aichele, W. Seifert, J. Persson, and O. Benson. Generating visible single photons on demand with single InP quantum dots. *Appl. Phys. Lett.*, 82(10):1509–1511, 2003.

[42] A. J. Shields. Semiconductor quantum light sources. *Nature Phot.*, 1:215–223, 2007.

Bibliography

[43] C. W. Chou, S. V. Polyakov, A. Kuzmich, and H. J. Kimble. Single-photon generation from stored excitation in an atomic ensemble. *Phys. Rev. Lett.*, 92(21):213601, 2004.

[44] D. Felinto, C. W. Chou, J. Laurat, E. W. Schomburg, H. de Riedmatten, and H. J. Kimble. Conditional control of the quantum states of remote atomic memories for quantum networking. *Nature Phys.*, 2:844–848, 2006.

[45] J. Sharping, J. Chen, X. Li, P. Kumar, and R. Windeler. Quantum-correlated twin photons from microstructure fiber. *Opt. Express*, 12(14):3086–3094, 2004.

[46] J. Fulconis, O. Alibart, W. Wadsworth, P. Russell, and J. Rarity. High brightness single mode source of correlated photon pairs using a photonic crystal fiber. *Opt. Express*, 13(19):7572–7582, 2005.

[47] W. H. Louisell, A. Yariv, and A. E. Siegman. Quantum fluctuations and noise in parametric processes. i. *Phys. Rev.*, 124(6):1646–1654, 1961.

[48] D. C. Burnham and D. L. Weinberg. Observation of simultaneity in parametric production of optical photon pairs. *Phys. Rev. Lett.*, 25(2):84–87, 1970.

[49] B. Y. Zeldovich and D. N. Klyshko. Field statistics in parametric luminescence. *JETP Lett.*, 9:40–43, 1969.

[50] A. Rastelli, S. Kiravittaya, and O. G. Schmidt. *Growths and Control of Optically Active Quantum Dots*, chapter 2, pages 31–69. Springer, 2009.

[51] N. Grandjean and M. Ilegems. Visible InGaN/GaN quantum-dot materials and devices. *Proc. IEEE*, 95(9):1853–1865, 2007.

[52] S. H. Xin, P. D. Wang, A. Yin, C. Kim, M. Dobrowolska, J. L. Merz, and J. K. Furdyna. Formation of self-assembling CdSe quantum dots on ZnSe by molecular beam epitaxy. *Appl. Phys. Lett.*, 69(25):3884–3886, 1996.

[53] G. J. Beirne, M. Jetter, M. Rossi, J. Porsche, F. Scholz, H. Schweizer, and T. J. Glynn. Optical studies of GaInP/GaP quantum dots. *J. Lumin.*, 102–103:1–6, 2003.

[54] C. Santori, M. Pelton, G. Solomon, Y. Dale, and Y. Yamamoto. Triggered single photons from a quantum dot. *Phys Rev. Lett.*, 86(8):1502–1505, 2001.

[55] Z. Yuan, B. E. Kardynal, R. M. Stevenson A. J. Shields, C. J. Lobo, K. Cooper, N. S. Beattie, D. A. Ritchie, and M. Pepper. Electrically driven single-photon source. *Science*, 295:102–105, 2002.

[56] B. Alloing, C. Zinoni, V. Zwiller, L. H. Li, C. Monat, M. Gobet, G. Buchs, A. Fiore, E. Pelucchi, and E. Kapon. Growth and characterization of single quantum dots emitting at 1300 nm. *Appl. Phys. Lett*, 86:101908, 2005.

[57] D. Elvira, R. Hostein, F. Bruno, L. Monniello, A. Michon, G. Beaudoin, R. Braive, I. Robert-Philip, I. Abram, I. Sagnes, and A. Beveratos. Single InAsP/InP quantum dots as telecommunications-band photon sources. *arXiv:1108.2439v1 [cond-mat]*, 2011.

[58] G. S. Solomon, M. Pelton, and Y. Yamamoto. Single-mode spontaneous emission from a single quantum dot in a three-dimensional microcavity. *Phys. Rev. Lett.*, 86(17):3903–3906, 2001.

[59] T. Yoshie, A. Scherer, J. Hendrickson, G. Khitrova, H. M. Gibbs, G. Rupper, C. Ell, O. B. Shchekin, and D. G. Deppe. Vacuum rabi splitting with a single quantum dot in a photonic crystal nanocavity. *Nature*, 432:200–203, 2004.

[60] A. Badolato, K. Hennessy, M. Atatüre, J. Dreiser, E. Hu, P. M. Petroff, and A. Imamoglu. Deterministic coupling of single quantum dots to single nanocavity modes. *Science*, 308(5725):1158–1161, 2005.

[61] D. Englund, D. Fattal, E. Waks, G. Solomon, B. Zhang, T. Nakaoka, Y. Arakawa, Y. Yamamoto, and J. Vuckovic. Controlling the spontaneous emission rate of single quantum dots in a two-dimensional photonic crystal. *Phys Rev. Lett.*, 95(1):013904, 2005.

[62] A. Zrenner, L. V. Butov, M. Hagn, G. Abstreiter, G. Böhm, and G. Weimann. Quantum dots formed by interface fluctuations in AlAs/GaAs coupled quantum well structures. *Phys. Rev. Lett.*, 72(21):3382–3385, 1994.

[63] K. Brunner, G. Abstreiter, G. Böhm, G. Tränkle, and G. Weimann. Sharp-line photoluminescence and two-photon absorption of zero-dimensional biexcitons in a GaAs/AlGaAs structure. *Phys. Rev. Lett.*, 73(8):1138–1141, 1994.

[64] L. Samuelson, C. Thelander, M.T. Bjork, M. Borgstrom, K. Deppert, K.A. Dick, A.E. Hansen, T. Martensson, N. Panev, A.I. Persson, W. Seifert, N. Skold, M.W. Larsson, and L.R. Wallenberg. Semiconductor nanowires for 0d and 1d physics and applications. *Physica E*, 25(2–3):313–318, 2004.

[65] M. T. Borgström, V. Zwiller, E. Müller, and A. Imamoglu. Optically bright quantum dots in single nanowires. *Nano Lett.*, 5(7):1439–1443, 2005.

[66] A. P. Alivisatos. Semiconductor clusters, nanocrystals, and quantum dots. *Science*, 271(5251):933–937, 1996.

[67] P. Michler. *Quantum Dot Single Photon Sources*, chapter 6, pages 185–225. Springer, 2009.

[68] O. Benson, C. Santori, M. Pelton, and Y. Yamamoto. Regulated and entangled photons from a single quantum dot. *Phys. Rev. Lett.*, 84(11):2513–2516, 2000.

[69] E. Stock, W. Unrau, A. Lochmann, J. A. Töfflinger, M. Öztürk, A. I. Toropov, A. K. Bakarov, V. A. Haisler, and D. Bimberg. High-speed single-photon source based on self-organized quantum dots. *Semicond. Sci. Technol.*, 26:014003, 2011.

[70] A. M. Zaitsev. *Optical Properties of Diamond.* Springer, 2001.

[71] J. Wrachtrup and F. Jelezko. Processing quantum information in diamond. *J. Phys.: Cond. Matter*, 18(18):S807–S824, 2006.

[72] G. Davies and M. F. Hamer. Optical studies of the 1.945 eV vibronic band in diamond. *Proc. R. Soc. Lond. A*, 348(1653):285–298, 1976.

[73] Y. Mita. Change of absorption spectra in type-Ib diamond with heavy neutron irradiation. *Phys. Rev. B*, 53(17):11360–11364, 1996.

[74] T. Gaebel, M. Domhan, C. Wittmann, I. Popa, F. Jelezko, J. Rabeau, A. Greentree, S. Prawer, E. Trajkov, P.R. Hemmer, and J. Wrachtrup. Photochromism in single nitrogen-vacancy defect in diamond. *Appl. Phys. B*, 82:243–246, 2006.

[75] A. Lenef, S. W. Brown, D. A. Redman, S. C. Rand, J. Shigley, and E. Fritsch. Electronic structure of the N-V center in diamond: Experiments. *Phys. Rev. B*, 53(20):13427–13440, 1996.

[76] A. Lenef and S. C. Rand. Electronic structure of the n-v center in diamond: Theory. *Phys. Rev. B*, 53(20):13441–13455, 1996.

[77] N. B. Manson, J. P. Harrison, and M. J. Sellars. Nitrogen-vacancy center in diamond: Model of the electronic structure and associated dynamics. *Phys. Rev. B*, 74(10):104303, 2006.

[78] A. Gali, M. Fyta, and E. Kaxiras. Ab initio supercell calculations on nitrogen-vacancy center in diamond: Electronic structure and hyperfine tensors. *Phys. Rev. B*, 77(15):155206, 2008.

[79] F. M. Hossain, M. W. Doherty, H. F. Wilson, and L. C. L. Hollenberg. Ab initio electronic and optical properties of the NV- center in diamond. *Phys. Rev. Lett.*, 101(22):226403, 2008.

[80] P. Tamarat, N. B. Manson, J. P. Harrison, R. L. McMurtrie, A. Nizovtsev, C. Santori, R. G. Beausoleil, P. Neumann, T. Gaebel, F. Jelezko, P. Hemmer, and J. Wrachtrup. Spin-flip and spin-conserving optical transitions of the nitrogen-vacancy centre in diamond. *New J. Phys.*, 10:045004, 2008.

[81] P. Neumann, R. Kolesov, V. Jacques, J. Beck, J. Tisler, A. Batalov, L. Rogers, N. B. Manson, G. Balasubramanian, F. Jelezko, and J. Wrachtrup. Excited-state spectroscopy of single NV defects in diamond using optically detected magnetic resonance. *New J. Phys.*, 11:013017, 2009.

[82] F. Jelezko and J. Wrachtrup. Read-out of single spins by optical spectroscopy. *J. Phys.: Cond. Matter*, 16(30):R1089–R1104, 2004.

[83] F. Jelezko, I. Popa, A. Gruber, C. Tietz, J. Wrachtrup, A. Nizovtsev, and S. Kilin. Single spin states in a defect center resolved by optical spectroscopy. *Applied Physics Letters*, 81:2160, 2002.

[84] F. Jelezko, T. Gaebel, I. Popa, A. Gruber, and J. Wrachtrup. Observation of coherent oscillations in a single electron spin. *Phys. Rev. Lett*, 92(7):076401, 2004.

[85] T. Gaebel, M.l Domhan, I. Popa, C. Wittmann, P. Neumann, F. Jelezko, J. R. Rabeau, N. Stavrias, A. D. Greentree, S. Prawer, J. Meijer, J. Twamley, P. R. Hemmer, and J. Wrachtrup. Room-temperature coherent coupling of single spins in diamond. *Nature Phys.*, 2(6):408–413, 2006.

[86] L. Childress, M. V. Gurudev Dutt, J. M. Taylor, A. S. Zibrov, F. Jelezko, J. Wrachtrup, P. R. Hemmer, and M. D. Lukin. Coherent dynamics of coupled electron and nuclear spin qubits in diamond. *Science*, 314(5797):281–285, 2006.

[87] P. Neumann, N. Mizuochi, F. Rempp, P. Hemmer, H. Watanabe, S. Yamasaki, V. Jacques, T. Gaebel, F. Jelezko, and J. Wrachtrup. Multipartite entanglement among single spins in diamond. *Science*, 320(5881):1326–1329, 2008.

[88] A. Bermudez, F. Jelezko, M. B. Plenio, and A. Retzker. Electron-mediated nuclear-spin interactions between distant nitrogen-vacancy centers. *Phys. Rev. Lett.*, 107(15):150503, 2011.

[89] T. Gaebel, I. Popa, A. Gruber, M. Domhan, F. Jelezko, and J. Wrachtrup. Stable single-photon source in the near infrared. *New J. Phys.*, 6:98, 2004.

[90] C. Wang, C. Kurtsiefer, H. Weinfurter, and B. Burchard. Single photon emission from SiV centres in diamond produced by ion implantation. *J. Phys. B*, 39(1):37, 2006.

[91] I. Aharonovich, S. Castelletto, B. C. Johnson, J. C. McCallum, D. A. Simpson, A. D. Greentree, and S. Prawer. Chromium single-photon emitters in diamond fabricated by ion implantation. *Phys. Rev. B*, 81(12):121201, 2010.

[92] S. Schietinger, M. Barth, T. Aichele, and O. Benson. Plasmon-enhanced single photon emission from a nanoassembled metal-diamond hybrid structure at room temperature. *Nano Lett.*, 9:1694–1698, 2009.

[93] M. Barth. *Hybrid Nanophotonic Elements and Sensing Devices Based on Photonic Crystal Structures*. PhD thesis, Humboldt-Universität zu Berlin, 2010.

[94] S. Schietinger. *Investigation, Manipulation, and Coupling of Single Nano and Quantum Emitters*. PhD thesis, Humboldt-Universität zu Berlin, 2011.

[95] A. T. Collins, M. F. Thomaz, and M. I. B. Jorge. Luminescence decay time of the 1.945 eV centre in type Ib diamond. *J. Phys. C*, 16(11):2177–2181, 1983.

[96] R. H. Hadfield. Single-photon detectors for optical quantum information applications. *Nature Phot.*, 3:696–705, 2009.

[97] G. H. Rieke. *Detection of Light*. Cambridge University Press, 2003.

[98] J. G. Rarity, K. D. Ridley, and P. R. Tapster. Absolute measurement of detector quantum efficiency using parametric downconversion. *Appl. Opt.*, 26(21):4616–4619, 1987.

[99] M. Ware and A. Migdall. Single-photon detector characterization using correlated photons: The march from feasibility to metrology. *J. Mod. Opt.*, 51(9-10):1549–1557, 2004.

[100] R. W. Romani, A. J. Miller, B. Cabrera, S. W. Nam, and J. M. Martinis. Phase-resolved crab studies with a cryogenic transition-edge sensor spectrophotometer. *Astrophys. J.*, 563(1):221–228, 2001.

[101] A. J. Miller, S. W. Nam, J. M. Martinis, and A.V. Sergienko. Demonstration of a low-noise near-infrared photon counter with multiphoton discrimination. *Applied Physics Letters*, 83(4):791–793, 2003.

[102] A. E. Lita, A. J. Miller, and S. W. Nam. Counting near-infrared single-photons with 95% efficiency. *Opt. Express*, 16(5):3032–3040, 2008.

[103] D. Fukuda, G. Fujii, T. Numata, A. Yoshizawa, H. Tsuchida, H. Fujino, H. Ishii, T. Itatani, S. Inoue, and T. Zama. Photon number resolving detection with high speed and high quantum efficiency. *Metrologia*, 46(4):S288–S292, 2009.

[104] R. H. Hadfield, M. J. Stevens, S. S. Gruber, A. J. Miller, R. E. Schwall, R. P. Mirin, and S. W. Nam. Single photon source characterization with a superconducting single photon detector. *Opt. Express*, 13(26):10846–10853, 2005.

[105] M. J. Stevens, R. H. Hadfield, R. E. Schwall, S. W. Nam, R. P. Mirin, and J. A. Gupta. Fast lifetime measurements of infrared emitters using a low-jitter superconducting single-photon detector. *Appl. Phys. Lett.*, 89(3):031109, 2006.

[106] C. Zinoni, B. Alloing, L. H. Li, F. Marsili, A. Fiore, L. Lunghi, A. Gerardino, Yu. B. Vakhtomin, K. V. Smirnov, and G. N. Gol'tsman. Single-photon experiments at telecommunication wavelengths using nanowire superconducting detectors. *Appl. Phys. Lett.*, 91(3):031106, 2007.

[107] R. H. Hadfield, J. L. Habif, J. Schlafer, R. E. Schwall, and S. W. Nam. Quantum key distribution at 1550 nm with twin superconducting single-photon detectors. *Appl. Phys. Lett.*, 89(24):241129, 2006.

[108] H. Takesue, S. W. Nam, Q. Zhang, R. H. Hadfield, T. Honjo, K. Tamaki, and Y. Yamamoto. Quantum key distribution over a 40 dB channel loss using superconducting single-photon detectors. *Nature Phot.*, 1:343, 2007.

[109] R. W. Heeres, S. N. Dorenbos, B. Koene, G. S. Solomon, L. P. Kouwenhoven, and V. Zwiller. On-chip single plasmon detection. *Nano Lett.*, 10(2):661–664, 2010.

[110] A. M. Kadin and M. W. Johnson. Nonequilibrium photon-induced hotspot: A new mechanism for photodetection in ultrathin metallic films. *Applied Physics Letters*, 69(25):3938–3940, 1996.

[111] F. Marsili, D. Bitauld, A.Gaggero, S. Jahanmirinejad, R. Leoni, F. Mattioli, and A. Fiore. Physics and application of photon number resolving detectors based on superconducting parallel nanowires. *New J. Phys.*, 11(4):045022, 2009.

[112] K. S. Il'in, M. Lindgren, M. Currie, A. D. Semenov, G. N. Gol'tsman, Roman Sobolewski, S. I. Cherednichenko, and E. M. Gershenzon. Picosecond hot-electron energy relaxation in NbN superconducting photodetectors. *Applied Physics Letters*, 76(19):2752–2754, 2000.

[113] A. Rothwarf and B. N. Taylor. Measurement of recombination lifetimes in superconductors. *Phys. Rev. Lett*, 19(1):27–30, 1967.

[114] M. Lindgren, M. Currie, W.-S. Zeng, R. Sobolewski, S. Cherednichenko, B. Voronov, and G. N. Gol'tsman. Picosecond response of a superconducting hot-electron NbN photodetector. *Appl. Supercond.*, 6(7-9):423–428, 1998.

[115] A. D. Semenov, G. N. Gol'tsman, and A. A. Korneev. Quantum detection by current carrying superconducting film. *Physica C*, 35:349–356, 2001.

[116] G. N. Gol'tsman, A. Korneev, I. Rubtsova, I. Milostnaya, G. Chulkova, O. Minaeva, K. Smirnov, B. Voronov, W. Sysz 2, A. Pearlman, A. Verevkin, and R. Sobolewski. Ultrafast superconducting single-photon detectors for near-infrared-wavelength quantum communications. *Phys. Stat. Sol. c*, 2:1480–1488, 2005.

[117] W. Slysz, M. Wegrzecki, J. Bar, P. Grabiec, M. Gorska, V. Zwiller, C. Latta, P. Bohi, I. Milostnaya, O. Minaeva, A. Antipov, O. Okunev, A. Korneev, K. Smirnov, B. Voronov, N. Kaurova, G. Gol'tsman, A. Pearlman, A. Cross, I. Komissarov, A. Verevkin, and R. Sobolewski. Fiber-coupled single-photon detectors based on NbN superconducting nanostructures for practical quantum

cryptography and photon-correlation studies. *Appl. Phys. Lett.*, 88(26):261113, 2006.

[118] S. N. Dorenbos. *Fabrication and charaterization of superconducting detectors for single photon counting.* Master thesis, TU Delft, 2007.

[119] A. J. Kerman, E. A. Dauler, W. E. Keicher, J. K. W. Yang, K. K. Berggren, G. N. Gol'tsman, and B. Voronov. Kinetic-inductance-limited reset time of superconducting nanowire photon counters. *Appl. Phys. Lett.*, 88(11):111116, 2006.

[120] A. Divochiy, F. Marsili, D. Bitauld, A. Gaggero, R. Leoni, F. Mattioli, A. Korneev, V. Seleznev, N. Kaurova, O. Minaeva, G. N. Gol'tsman, K. G. Lagoudakis, M. Benkhaoul, F. Levy, and A. Fiore. Superconducting nanowire photon-number-resolving detector at telecommunication wavelengths. *Nature Phot.*, 2:302 –306, 2008.

[121] F. Marsili, A. Fiore D. Bitauld, A. Gaggero, R. Leoni, F. Mattioli, A. Divochiy, A. Korneev, V. Seleznev, N. Kaurova, O. Minaeva, and G. N. Goltsman. Superconducting parallel nanowire detector with photon number resolving functionality. *J. Mod. Opt.*, 56(2–3):334–344, 2009.

[122] A. Engel, A. Semenov, H.-W. Hübers, K. Ilin, and M. Siegel. Dark counts of a superconducting single-photon detector. *Nuclear Instr. & Meth. A*, 520:32–35, 2004.

[123] A. Engel, A. Semenov, H.-W. Hübers, K. Il'in, and M. Siegel. Fluctuations and dark count rates in superconducting NbN single-photon detectors. *Phys. Stat. Sol. c*, 2:1668, 2005.

[124] J M Kosterlitz and D J Thouless. Ordering, metastability and phase transitions in two-dimensional systems. *J. Phys. C*, 6(7):1181–1203, 1973.

[125] J. Kitaygorsky, J. Zhang, A. Verevkin, A. Sergeev, A. Korneev, V. Matvienko, P. Kouminov, K. Smirnov, B. Voronov, G. Gol'tsman, and R. Sobolewski. Origin of dark counts in nanostructured NbN single-photon detectors. *IEEE Appl. Supercond.*, 15(2):545–548, 2005.

[126] S. Cherednichenko, P. Yagoubov, K. Il'in, G. Gol'tsman, and E. Gershenzon. Large bandwidth of NbN phonon-cooled hot-electron bolometer mixers on sapphire substrates. *Proc. 8th Int. Symp.on Space Terahertz Technology*, pages 245–257, 1997.

[127] A. Röseler. *Infrared Spectroscopic Ellipsometry.* Akademie-Verlag Berlin, 1990.

[128] K. M. Rosfjord, J. K. W. Yang, E. A. Dauler, A. J. Kerman, V. Anant, B. M. Voronov, G. N. Gol'tsman, and K. K. Berggren. Nanowire single-photon detector with an integrated optical cavity and anti-reflection coating. *Opt. Express*, 14(2):527–534, 2006.

[129] R. H. Hadfield, P. A. Dalgarno, J. A. O'Connor, E. Ramsay, R. J. Warburton, E. J. Gansen, B. Baek, M. J. Stevens, R. P. Mirin, and S. W. Nam. Submicrometer photoresponse mapping of nanowire superconducting single-photon detectors. *Appl. Phys. Lett.*, 91(24):241108, 2007.

[130] A. Semenov, A. Engel, H.-W. Hübers, K. Il'in, and M. Siegel. Spectral cut-off in the efficiency of the resistive state formation caused by absorption of a single-photon in current-carrying superconducting nano-strips. *Eur Phys J B*, 47:495–501, 2005.

[131] A. Semenov, P. Haas, K. Il'in, H.-W. Hübers, M. Siegel, A. Engel, and A. Smirnov. Energy resolution and sensitivity of a superconducting quantum detector. *Physica C*, 460:1491–1492, 2007.

[132] A. D. Semenov, P. Haas, B. Günther, H.-W. Hübers, K. Il'in, and M. Siegel. Energy resolution of a superconducting nanowire single-photon detector. *J. Low Temp. Phys.*, 151:564–569, 2008.

[133] A. Verevkin, J. Zhang, R. Sobolewski, A. Lipatov, O. Okunev, G. Chulkova, A. Korneev, K. Smirnov, G. N. Gol'tsman, and A. Semenov. Detection efficiency of large-active-area NbN single-photon superconducting detectors in the ultraviolet to near-infrared range. *Applied Physics Letters*, 80(25):4687–4689, 2002.

[134] R. Hanbury-Brown and R. Q. Twiss. A new type of interferometer for use in radio astronomy. *Phil. Mag.*, 45(366):663–682, 1954.

[135] R. Hanbury-Brown and R. Q. Twiss. Correlation between photons in two coherent beams of light. *Nature*, 177:27–29, 1956.

[136] T. Aichele. *Detection and Generation of Non-Classical Light States from Single Quantum Emitters*. PhD thesis, Humboldt-Universität zu Berlin, 2005.

[137] P. Schwille. Fluorescence correlation spectroscopy and its potential for intracellular applications. *Cell. Biochem. Biophys.*, 34:383–408, 2001.

[138] S. M. Barnett and S. Croke. Quantum state discrimination. *Adv. Opt. Photon.*, 1:238–258, 2009.

[139] C. W. Helstrom. Quantum detection and estimation theory. *J. Stat. Phys.*, 1:231–252, 1969.

[140] U. Herzog and J. A. Bergou. Distinguishing mixed quantum states: Minimum-error discrimination versus optimum unambiguous discrimination. *Phys. Rev. A*, 70(2):022302, 2004.

[141] U. Herzog and O. Benson. Generalized measurements for optimally discriminating two mixed states and their linear-optical implementation. *J. Mod. Opt.*, 57:188–197, 2010.

[142] U. Herzog. Discrimination of two mixed quantum states with maximum confidence and minimum probability of inconclusive results. *Phys. Rev. A*, 79:032323, 2009.

[143] S. Croke, E. Andersson, S. M. Barnett, C. R. Gilson, and J. Jeffers. Maximum confidence quantum measurements. *Phys. Rev. Lett.*, 96:070401, 2006.

[144] T. Rudolph, R. W. Spekkens, and P. S. Turner. Unambiguous discrimination of mixed states. *Phys. Rev. A*, 68:010301(R), 2003.

[145] B. Huttner, A. Muller, J. D. Gautier, H. Zbinden, and N. Gisin. Unambiguous quantum measurement of nonorthogonal states. *Physical Review A*, 54(5):3783–3789, Nov 1996.

[146] R. B. M. Clarke, A. Chefles, S. M. Barnett, and E. Riis. Experimental demonstration of optimal unambiguous state discrimination. *Phys. Rev. A*, 63(4):040305, Mar 2001.

[147] J. A. Bergou, U. Herzog, and M. Hillery. Quantum filtering and discrimination between sets of Boolean functions. *Phys. Rev. Lett.*, 90(25):257901, Jun 2003.

[148] M. Mohseni, A. M. Steinberg, and J. A. Bergou. Optical realization of optimal unambiguous discrimination for pure and mixed quantum states. *Phys. Rev. Lett.*, 93(20):200403, Nov 2004.

[149] U. Herzog and J. A. Bergou. Optimum unambiguous discrimination of two mixed quantum states. *Phys. Rev. A*, 71(5):050301(R), 2005.

[150] P. Raynal and N. Lütkenhaus. Optimal unambiguous state discrimination of two density matrices: Lower bound and class of exact solutions. *Phys. Rev. A*, 72:022342, 2005.

[151] J. A. Bergou, E. Feldman, and M. Hillery. Optimal unambiguous discrimination of two subspaces as a case in mixed-state discrimination. *Phy. Rev. A*, 73:032107, 2006.

[152] U. Herzog. Optimum unambiguous discrimination of two mixed states and application to a class of similar states. *Phys. Rev. A*, 75:052309, 2007.

[153] M. Kleinmann, H. Kampermann, and D. Bruß. Unambiguous discrimination of mixed quantum states: Optimal solution and case study. *Phys. Rev. A*, 81:020304, 2010.

[154] S. M. Barnett and E. Riis. Experimental demonstration of polarization discrimination at the Helstrom bound. *J. Mod. Opt.*, 44:1061–1064, 1997.

[155] R. B. M. Clarke, V. M. Kendon, A. Chefles, S. M. Barnett, E. Riis, and M. Sasaki. Experimental realization of optimal detection strategies for overcomplete states. *Phys. Rev. A*, 64:012303, 2001.

[156] J. Mizuno, M. Fujiwara, M. Akiba, T. Kawanishi, S. M. Barnett, and M. Sasaki. Optimum detection for extracting maximum information from symmetric qubit sets. *Phys. Rev. A*, 65:012315, 2001.

[157] P. J. Mosley, S. Croke, I. A. Walmsley, and S. M. Barnett. Experimental realization of maximum confidence quantum state discrimination for the extraction of quantum information. *Phys. Rev. Lett.*, 97:193601, 2006.

[158] B. L. Higgins, B. M. Booth, A. C. Doherty, S. D. Bartlett, H. M. Wiseman, and G. J. Pryde. Mixed state discrimination using optimal control. *Phys. Rev. Lett.*, 103:220503, 2009.

[159] Y. Lu, N. Coish, R. Kaltenbaek, D. R. Hamel, S. Croke, and K. J. Resch. Minimum-error discrimination of entangled quantum states. *Phys. Rev. A*, 82(4):042340, 2010.

[160] M. Koashi and N. Imoto. Quantum cryptography based on two mixed states. *Phys. Rev. Lett.*, 77(10):2137–2140, Sep 1996.

[161] G. A. Steudle, S. Knauer, U. Herzog, E. Stock, V. A. Haisler, D. Bimberg, and O. Benson. Experimental optimal maximum-confidence discrimination and optimal unambiguous discrimination of two mixed single-photon states. *Phys. Rev. A*, 83(5):050304(R), 2011.

[162] A. Lochmann, E. Stock, J. A. Töfflinger, W. Unrau, A. Toropov, A. Bakarov, V. A. Haisler, and D. Bimberg. Electrically pumped, micro-cavity based single photon source driven at 1 GHz. *Electron. Lett.*, 45:566–567, 2009.

[163] P. Kok, W. J. Munro, K. Nemoto, T. C. Ralph, J. P. Dowling, and G. J. Milburn. Linear optical quantum computing with photonic qubits. *Rev. Mod. Phys.*, 79(1):135–174, 2007.

[164] R. Horodecki, P. Horodecki, M. Horodecki, and K. Horodecki. Quantum entanglement. *Rev. Mod. Phys.*, 81:865–942, 2009.

[165] T. H. Taminiau, F. D. Stefani, and N. F. van Hulst. Single emitters coupled to plasmonic nano-antennas: angular emission and collection efficiency. *New J. Phys.*, 10:105005, 2008.

[166] Y.S. Park, A.K. Cook, and H. Wang. Cavity QED with diamond nanocrystals and silica microspheres. *Nano Lett.*, 6(9):2075–2079, 2006.

List of Own Publications

The following articles have been published by the author in peer-reviewed journals. The one marked by an asterisk arose from work which was not part of this thesis.

Steudle *et al.* 2012 G. A. Steudle, S. Schietinger, D. Höckel, S. N. Dorenbos, V. Zwiller, and O. Benson. The quantum nature of light measured with a single detector. Submitted (2012), available at http://arxiv.org/abs/1107.1353 (arXiv:1107.1353v1)

Steudle *et al.* 2011 G. A. Steudle, S. Knauer, U. Herzog, E. Stock, V. A. Haisler, D. Bimberg, and O. Benson. Experimental optimal maximum-confidence discrimination and optimal unambiguous discrimination of two mixed single-photon states. *Phys. Rev. A*, 83(5):050304(R), 2011.

****Neacsu *et al.* 2005** C. C. Neacsu, G. A. Steudle, and M. B. Raschke. Plasmonic light scattering from nanoscopic metal tips. *Appl. Phys. B*, 80(3):295–300, 2005.

Conference presentations

The following presentations have been given by the author at scientific conferences.

G. A. Steudle, S. Schietinger, D. Höckel, S. N. Dorenbos, V. Zwiller, and O. Benson. Analysing non-classical photon statistics of quantum emitters with a single superconducting detector (talk). *SPIE Conference on Optics and Optoelectronics*, Prague, 2011.

G. A. Steudle, S. Knauer, U. Herzog, E. Stock, D. Bimberg, and O. Benson. Experimental optimum unambiguous discrimination of two mixed single-photon states (talk). *DPG Spring Meeting*, Dresden, 2011.

G. A. Steudle, S. Knauer, U. Herzog, and O. Benson. Experimental implementation of optimum unambiguous and maximum-confidence discrimination of two mixed state (poster). *CLEO*, San José (USA), 2010.

G. A. Steudle, S. Knauer, U. Herzog, and O. Benson. Experimental results for unambiguous state discrimination (talk). *DPG Spring Meeting*, Hannover, 2010.

G. A. Steudle, S. N. Dorenbos, I. Müller, V. Zwiller, and O. Benson. Superconducting single-photon detectors (poster). *iNOW*, Stockholm/Berlin, 2009.

List of Own Publications

G. A. Steudle, S. N. Dorenbos, I. Müller, V. Zwiller, and O. Benson. Photon counting with fiber-coupled superconducting single-photon detectors (poster). *International Workshop on Fundamentals of Light-Matter Interaction*, Recife (Brazil), 2008.

G. A. Steudle, M. Barth, and O. Benson. Modification of spontaneous emission of nanoscopic particles near interfaces (talk). *DPG Spring Meeting*, Frankfurt, 2006.

Acknowledgement

Selbständigkeitserklärung

Ich erkläre, dass ich die vorliegende Arbeit selbständig und nur unter Verwendung der angegebenen Literatur und Hilfsmittel angefertigt habe.

Berlin, den 16. Februar 2012   Gesine Anne Steudle